Milli-kelvin Thermodynamic and Transport Measurements of Low Dimensional Systems in High Magnetic Fields

Submitted by Martin Joseph Smith, to the University of Exeter as a thesis for the degree of Doctor of Philosophy in Physics, September 2009.

I certify that all material in this thesis which is not my own work has been identified and that no material has previously been submitted and approved for the award of a degree by this or any other University.

.....Martin J Smith

Abstract

This thesis presents an investigation into aspects of the integer quantum Hall effect, specifically the near-dissipationless state of the longitudinal resistivity ρ_{xx} between Landau levels, and the associated broadening of the levels. Eddy currents induced by a time varying magnetic field B are considered in chapter 4. The temperature dependences of the eddy currents were measured over the range 100 mK to 1600 mK. The peak current at filling factor $\nu = 2$ was shown to saturate at $\gtrsim 800$ mK, more robust than previously observed, but was reduced by elevating the temperature to 1600 mK. The saturated regime is associated with a breakdown of the quantum Hall effect, and in this case, the most likely candidate for the saturation is an electron heating effect.

Sweep-rate dependences were characterised for a range of filling factors and temperatures, and even for the lowest sweep rates, never entered a linear regime. Induced currents $\nu = 1, 2$ and 4 all saturated at the same critical value at 100 mK, but $\nu = 4$ was shown to reduce with slower sweep rates, consistent with the prediction that the ρ_{xx} minima is not as small as for lower Landau levels. Induced current decays were measured to be similar to previous work, a fast initial decay attributed to breakdown of the QHE followed by a much longer slow decay. The eddy decay of $\nu = 1$ at low temperature, in the slow decay regime, is among the most persistent reported. It was shown that the assumptions of previous work had not evaluated the mutual inductance of the eddy current in the presence of the magnet sufficiently. By fitting a suitable function to the IV characteristic of $\nu = 1$ the shape of the induced current was modeled. The model agreed with the data, producing a similar shape and a very long time constant for the slow decay.

In chapter 5 the hysteresis in the magnetoresistance of a quantum point contact was investigated, through a simultaneous transport and magnetometry measurement. Induced currents corresponding to filling factors up to $\nu = 8$ were measured. Three corresponding features were measured in the magnetoresistance of a QPC, one more than previously seen. The temperature dependence was measured simultaneously, and for Landau level filling factor $\nu = 1$, the general shape of the curves was the same. The sweep rate IV characteristics of the the two experiments were similar. Sweeping the magnetic field B to a fixed field position and waiting, demonstrated that both phenomena decay with time, a fast decay of seconds and a slow decay taking more than $10,000$ seconds. An attempt was made to affect the induced eddy current by switching the QPC gate on/off. Experiments on a fast timescale, 10 ms, resolved structure in the induced currents that has previously been attributed to the noisy breakdown of the quantum Hall effect. By performing a simultaneous measurement, individual breakdown events were seen and correlated.

After investigating the zero-resistance state in chapter 4 and chapter 5 with induced currents, exactly how the zero-resistance state varied between Landau levels was the topic of chapter 6. A method was presented for the fabrication of a novel device, to measure the magnetisation and the heat capacity of a 2DES at the same time. AuGe thin film resistors were grown in only 10 bilayers, reducing the heat capacity per unit area by approximately an order of magnitude on previous workers. The AuGe thermometers were shown to be 'tunable', i.e. the temperature dependence was dictated by the annealing conditions after growth, so thermometers with different gold concentrations due to growth conditions, could be tuned to have similar temperature dependences. Low temperature thermometers with small heat capacities were repeatably produced, and thermometer D5 is presented in this thesis with a sensitivity of $S = 0.58$.

At an elevated refrigerator temperature of nearly 300 mK, heat pulses of ~ 26 nJ were resolved on a device which had a 100% front processing success rate, but was not etched from the back. It was shown that a device to measure the broadening of the low temperature, high magnetic field 2DES density of states is possible.

Acknowledgements

There have been many people who have helped me enormously over the course of my PhD. First I would like to thank my supervisors Dr Alan Usher and Dr Charles Williams for all the help and inspiration along the way.

An experimental low temperature physics project could not happen without all the support staff. Thank you to Dave Manning and Adam Woodgate for the the liquid helium and liquid nitrogen, especially the flavour that comes at short notice. The mechanical workshop guys, Steve Tuckett, Matt Wears, Pete Cann, Paul Wilkins, John Meakin and Kevyn White.

I would also like to thank Geoff Hill at Sheffield University for the enormous help he has been over the course of the project. In developing the dual cantilever-calorimeter we shared a lot of frustrations together, and saw more than our fair share of scratched tracks.

Thank you to Tony Matthews, Tristan Kershaw and especially James Gething for the handing down of refrigerators and knowledge. Thank you to all my friends who have been great fun over the last few years, there are too many of you to list. Thank you to my parents for supporting me in whatever I wanted to do.

I also need to mention Batman: the world's greatest detective. You ask all the right questions, always have a plan, the night is never too late for you, the pressure is never too much and a deadline is never too close. You are an inspiration to me.

Finally I would like to thank the eddy currents, they may not have put a lot of energy into this project, but without their tiny contribution it would not have been possible.

Contents

List of Figures

List of Tables

Chapter 1

Introduction

Two dimensional electron systems (2DESs) allow the study of electron fluids in an environment with extremely low disorder. There have been intensive studies of these systems since the discovery of the quantum Hall effect (QHE) by Klaus von Klitzing in 1980 [1], which was predicted several years earlier by Ando et al. [2]. This effect, sometimes referred to as the Integer quantum Hall effect (IQHE) and the later discovery of the fractional quantum Hall effect (FQHE) by Tsui et al. [3] and Stormer [4], were awarded Nobel prizes in physics, in 1985 and 1998 respectively.

Although current technology can produces 2DESs with very high mobilities, they are still not ideal systems. The electrons do experience residual disorder, but this can make them all the more interesting to study. By probing these low dimensional systems a wealth of information can be obtained, in particular the form of the density of states (DOS), a quantity of particular physical interest. For 2D electrons in a magnetic field, the DOS is characterised by peaks in the vicinity of Landau levels (LL) and by almost zero values between them, resulting in an oscillatory character to a wide range of phenomena including electrical, magnetic and thermal properties of the system. The $1/B$ oscillatory phenomenon that is best studied in the GaAs/(Al,Ga)As 2DES is the QHE. In all physical properties that are measured via transport effects, pinning of the Fermi level takes place in regions of localised states, which do not conduct current. However, for equilibrium properties such as

specific heat or magnetisation, the difference between localised and extended states is of no importance, and these equilibrium properties reveal the total density of states.

The specific mechanism for the breakdown of the quantum Hall effect in the dissipationless state in which the Fermi energy lies between Landau levels is not well understood. The value of this near-zero-resistance state is dictated by, and is yet another probe of, the shape of the DOS. In a time varying magnetic field of constant dB/dt eddy currents are induced, which have a magnetic moment and can therefore be detected with a contactless magnetometry measurement. The breakdown of the QHE via eddy currents is investigated in chapter 4, and they are seen to saturate with magnetic field sweep rate and with temperature. Induced currents in the zero resistance state are characterised by a fast decay attributed to the breakdown of the QHE and a long decay dictated by the value of the resistance minimum between LL's.

The perturbation of the electrostatic potential of a quantum point contact (QPC), due to induced currents, is investigated in chapter 5. Eddy currents are not measured in a typical transport measurement, but are shown to affect the QPC, evident by a hysteretic magnetoresistance.

The Helmholtz free energy, a thermodynamic potential, can be probed by use of magnetisation, and through this, information about the broadening of the DOS can be obtained. There have been many attempts to probe the form of the DOS through magnetisation studies, using cantilever magnetometry [5], and different types of torsion balance magnetometers [6, 7, 8]. Another thermodynamic measurement that arises from, and therefore relates back to the form of the DOS is the heat capacity of the 2DES, and both heat pulse [9, 10] and AC calorimetry [11] have been used to measure this quantity. Heat capacity and magnetisation measurements should in principle produce the same answer to the fundamental question about the shape of the broadening of the DOS. However, there is a lack of consensus regarding the form of the DOS on the magnetic field dependence of the broadening. Various methods have been used to measure both, and a wide variety of models proposed

both theoretically and experimentally. Workers have proposed Gaussian [11, 12, 13, 14] and Lorentzian [15] broadened Landau levels with both a broadening parameter independent of B [12, 16, 14, 15] and dependent as $B^{1/2}$ [17, 13]. Many authors have had to use a non-zero background DOS between LLs to explain the discrepancy between results and theory.

The lack of consensus about the form of the DOS in the literature motivates further investigation with both experiments. Improvements in fabrication technology mean that cantilever magnetometry may become much more sensitive than the torsion balance technique. The same argument extends to the heat capacity experiment. A new understanding may arise from probing the same fundamental physics with two different measurement techniques, on the same sample, during the same cool-down. Chapter 6 discusses the viability of combining both experiments onto a single device, and presents preliminary measurements.

Chapter 2

Background

2.1 Two-dimensional electron systems

2.1.1 Construction of a Two Dimensional System

A two-dimensional electron system (2DES) can be realised at the interface between two semiconductors of different bandgaps. The system under experimental investigation is a GaAs/(Al,Ga)As heterostructure as depicted in figure 2.1. When the two semiconductors are brought together there is a band bending caused by the transfer of electrons from the n-type (Al,Ga)As side (with silicon as a dopant) to the GaAs (which is taken to be weakly p-type). This transport of electrons leaves a positive donor space charge layer, which is responsible for the upward curvature in the conduction band on the (Al,Ga)As side. Because of the excess electrons on the GaAs side there is a negative space charge that leads to the downward bending in the conduction band.

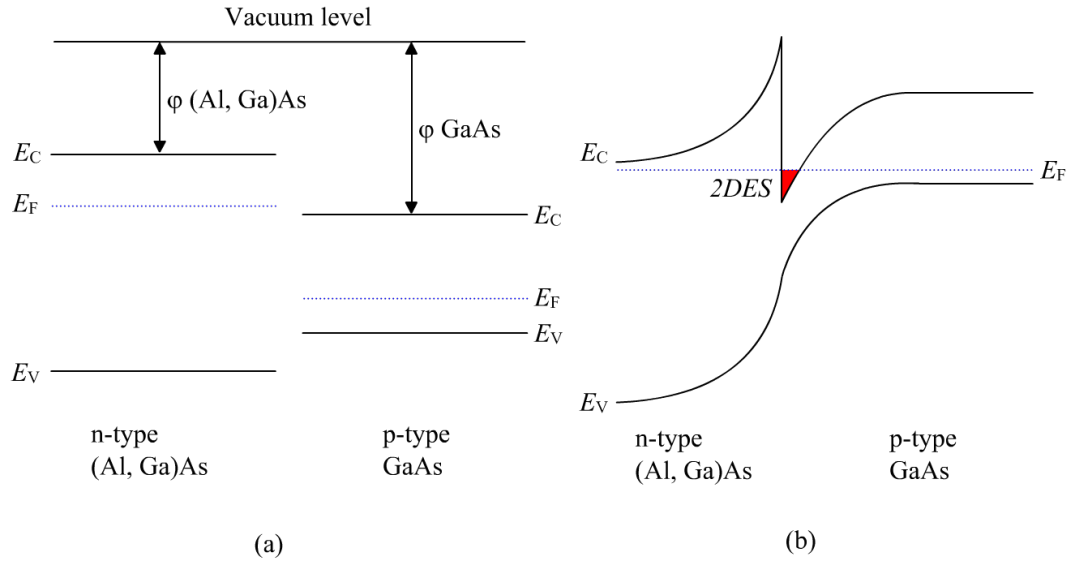

Figure 2.1: A simplified heterojunction: two separate n- and p-type semiconductors with different bandgaps (a), are brought together to form a heterojunction (b), confining a 2DES at the electrostatic boundary.

Modulation doped heterostructures grown by molecular beam epitaxy (MBE) have revolutionised the field; simplistically, instead of just growing the doped (Al,Ga)As layer on top of a GaAs layer, an extra undoped (Al,Ga)As layer is introduced. The electrons from the donor atoms are still free to diffuse over to the GaAs layer through this additional one, and are confined to a triangular quantum well, having left ionised donors on the (Al,Ga)As side. The mobility of the electrons in the 2DES is largely limited by remote ionised impurity scattering. The electrons are still subject to an attractive force but cannot return over the potential barrier; they are bound against the (Al,Ga)As wall. Another form of remote doping, δ-doping, is utilised for the sample AK47 which is discussed in later chapters. Unlike the distribution of dopant atoms in the modulation growth process, in δ-doping the dopant atoms are placed in a single layer in the growth process (growth details of samples included in this thesis can be found in section 3.6). This confining potential at the interface forces the motion of the electrons in the growth direction (defined as the z-direction), to be quantised into a series of sub-bands of energy E_n. The sub-band separation is dependent on the electric field. The system is approximated to be finite triangular, and an appropriate trial ground-state wavefunction to describe such a 2DES is the

Fang-Howard wavefunction [18], which is depicted in figure 2.2.

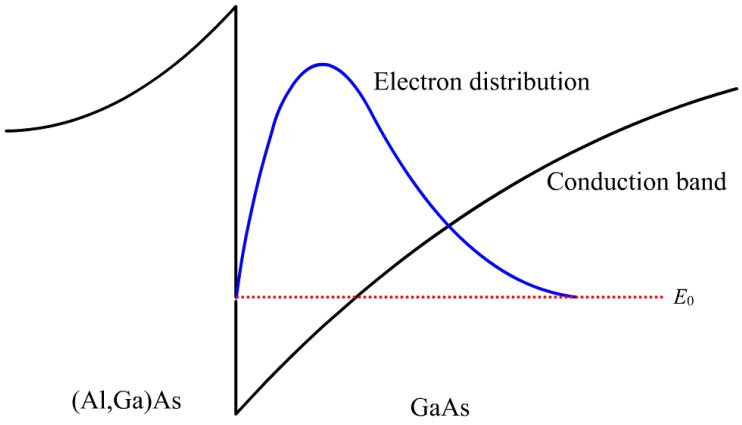

Figure 2.2: Illustration of the ground state wavefunction of a heterojunction.

This wavefunction and its eigenvalues have only one adjustable parameter, which is dependent on the electric field within the well. The wavefunction is given by,

$$\chi_0(z) = \sqrt{\frac{b^3}{2} z \exp\left(-\frac{bz}{2}\right)}, \tag{2.1}$$

where b is a variational parameter given by

$$b = \left(\frac{12 m^* e^2}{\varepsilon \hbar^2}\right)^{1/3} \left(N_{\text{depl}} + \frac{11}{32} N_{\text{s}}\right)^{1/3}, \tag{2.2}$$

and m^* is the effective mass, ε the dielectric constant of the channel layer and N_{depl} is the density of fixed charge in the depletion layer, and E_{g} the bang gap in (Al,Ga)As. Evaluation of the expectation value of z for the Fang-Howard wavefunction reveals that $\langle z \rangle = 3/b$ (where $\langle z \rangle$ is the average distance of the 2D wavefunction from the interface). This describes the wavefunction as being bound in the $z-$direction, however the electrons experience a constant potential in the $x-$ and $y-$directions, so are free to conduct. Figure 2.2 sketches this wavefunction, and shows it to be an appropriate choice for the ground state wavefunction as it disappears at z=0, and decays exponentially into the finite barrier.

Surface of Liquid Helium

Another way to realise a 2DES is to put electrons on the surface of liquid helium. Helium is the only substance that does not solidify upon cooling, even at zero kelvin. At atmospheric pressure, helium liquefies at 4.2 K. Electrons approaching the helium surface from above are attracted to the surface due to the electric polarisation of the helium atoms, however a potential barrier to enter the liquid exists. Helium has 1s orbitals that are completely filled, and the next available orbital 2s, has an energy that is too high to become occupied. Therefore if an electron is forced into the liquid, the electron does not go into an atomic orbital of helium, but pushes aside the liquid helium instead, effectively forming a bubble around itself. This costs the formation energy of the bubble and the kinetic energy related to the confinement. Therefore, the liquid helium acts as a potential barrier. Electrons are bound near the surface just as in the case of semiconductors, and a two-dimensional system is realised.

By placing a metal plate below the surface of the liquid helium and applying a positive voltage the electron density can be controlled. The electron density has an upper limit of $\sim 10^{12}\,\mathrm{m}^{-2}$. The surface can be thought of as having dimples below each bound electron, and whilst the number density is low, the dimples are independent of each other. As the density is increased the dimples overlap and this tends to enhance the density fluctuations of the electrons, i.e. in a higher density region, the dimple is larger and will therefore causes other electrons to come closer. This positive feedback drives an exponential increase in the size of the dimple, and then the electrons are able to escape to the metal plate below when the dimple is deep enough. There then must be an upper limit to the electron density in liquid helium, which is qualitatively different to the semiconductor system where there is in practice a lower bound to the electron density. Another difference is that in helium, the mass of the electron is the same as the vacuum mass. Therefore, the Fermi energy as defined by

$$E_{\mathrm{F}} = \frac{p_{\mathrm{F}}^2}{2m_e}, \tag{2.3}$$

which is $\sim 2\,\mathrm{mK}$ at most. The electrons therefore act as non-degenerate classical particles at ordinary experimental temperatures ($T > 10\,\mathrm{mK}$). The small effective mass of a 2DES in GaAs makes the Fermi energy much higher, of the order several hundred kelvin, and is therefore Fermi degenerate at liquid helium temperatures.

It was demonstrated by Etz et al. [19] that in the special case of electrons on a supported helium surface, the helium system could be made degenerate. By using a thin film of helium as a substrate for the surface-state electrons, the film was additionally stabilised by van der Waals forces, achieving electron densities up to $\sim 10^{11}\,\mathrm{cm}^{-2}$. Because surface-state electrons are perturbed by surface roughness of the substrate under the thin helium film, compared to the cleaner enviroment of bulk helium, low frequency conductivity measurements are noiser. Mistura et al. [20] worked towards overcoming this limitation with a microwave cavity technique, which they showed to be sensitive over very small horizontal distances, $\sim 10\,\text{Å}$, reducing the influence of surface defects.

2.1.2 Two Dimensional Density of States

The following two sections are modified from bookwork in McMurry and Someren [21], and discussions with Alan Usher. In a 3D system the density of states (DOS) varies as $E^{1/2}$, confining the electrons to two dimensions has a dramatic effect. The free-particle Schrödinger equation (SE) in two-dimensions is,

$$-\frac{\hbar^2}{2m^*}\left(\frac{\partial^2}{\partial x^2}+\frac{\partial^2}{\partial y^2}\right)\psi_k(r) = E_k\psi_k(r). \tag{2.4}$$

Consider a two-dimensional sheet confining the electrons, with dimensions L_x and L_y (where $L_x = L_y = L$). The electron wavefunction is assumed to satisfy periodic boundary conditions, so a good choice for the wavefunction would be,

$$\psi(x,y) = \exp(ik_x x)\exp(ik_y y), \tag{2.5}$$

where k_x has to satisfy periodic boundary conditions,

$$k_x = 0; \quad \pm\frac{2\pi}{L}; \quad \pm\frac{4\pi}{L}; \tag{2.6}$$

Similarly for k_y. The allowed values of k are uniformly distributed in k-space with a separation $2\pi/L$. The density of states in k space, $g(k)dk$ is given by dividing the area of k-space in the range $(k, k+dk)$ by the area of k-space taken up by one state,

$$g(k)dk = 2\pi k \left(\frac{L}{2\pi}\right)^2 dk. \tag{2.7}$$

The DOS in k-space can be related to the DOS in energy space by the relation,

$$E_n = \frac{\hbar^2 k^2}{2m} \tag{2.8}$$

The following substitutions can be made,

$$k = \left(\frac{2mE}{\hbar^2}\right)^{1/2}, \tag{2.9}$$

$$dk = \left(\frac{m}{\hbar^2}\right)\left(\frac{2mE}{\hbar^2}\right)^{-1/2} dE. \tag{2.10}$$

Substituting these expressions into equation 2.7, also including a factor of 2 for spin degeneracy, the DOS as a form of energy is given by,

$$D(E)dE = \frac{mL^2}{\pi\hbar^2}dE \tag{2.11}$$

This result is independent of energy. The effect of confining electrons to a two dimensional well produces a DOS with a step like function. As well width approaches infinity the two-dimensional case approaches that of the three dimensional.

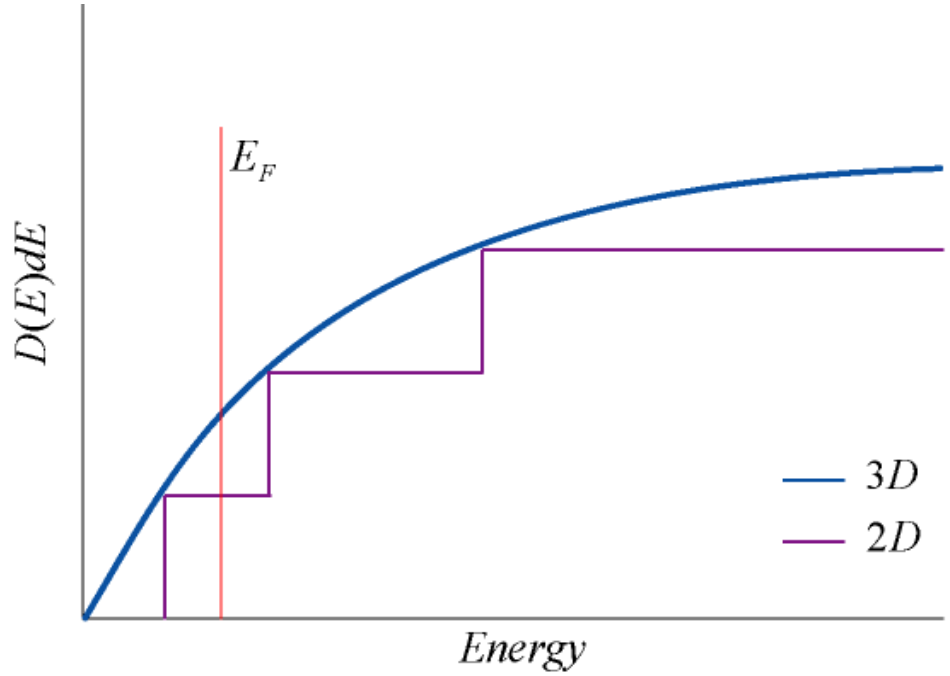

Figure 2.3: The density of states for a 3D and 2D system. The position of the Fermi energy is indicated for the condition that only the first sub-band is occupied at a finite temperature.

The position of the Fermi energy can now be obtained from the DOS by noting that,

$$N = \int_0^\infty D(E)f(E)dE, \tag{2.12}$$

where $f(E)$ is the Fermi distribution of states. Taking the degeneracy per unit area and the number of electrons per unit area, the number density is,

$$n_e = \frac{m^* E_\mathrm{F}}{\pi\hbar^2} \tag{2.13}$$

2.1.3 Two Dimensional Electrons in a Magnetic Field

Applying a magnetic field perpendicular to the plane of the 2DES results in complete quantisation of the electrons. This again has a dramatic effect on the shape of the DOS, to fully understand the problem a quantum mechanical approach is required.

The general Hamiltonian for the electrons is of the form,

$$H = \frac{1}{2m^*}[-i\hbar\nabla - q\mathbf{A}(x,y,z)]^2 + qV(x,y,z), \tag{2.14}$$

where A is the vector potential of the magnetic field and V is the scalar potential of the electric field. A uniform magnetic field B, applied in the $z-$direction with respect to the 2DES, which is confined to the $x-y$ plane, can be represented by a vector potential knowing,

$$\mathbf{B} = \nabla \times \mathbf{A}, \tag{2.15}$$

where the vector potential is chosen as:

$$A_x = 0 \qquad A_y = Bx \qquad A_z = 0. \tag{2.16}$$

This is known as the Landau gauge. Because the electric field is taken to be constant; the scalar potential $V = 0$. Substituting the vector potential from equation 2.16 into 2.14, gives the Schrödinger equation to be solved:

$$-\frac{\hbar^2}{2m}\left[\frac{\partial^2}{\partial z^2} + \frac{\partial^2}{\partial x^2} + \left(\frac{\partial}{\partial y} + \frac{ieB}{\hbar}\right)^2\right]\psi(x,y,z) = E\psi(x,y,z). \tag{2.17}$$

A 2D understanding is all that is required, therefore the Hamiltonian can be simplified. The $y-$component of the momentum operator commutes with the Hamiltonian,

$$\left[-i\hbar\frac{\partial}{\partial y}, \hat{H}\right] = 0. \tag{2.18}$$

Therefore the energy eigenfunctions will be eigenfunctions of P_y,

$$\psi(x,y) = \psi(x)e^{(ik_y y)} \tag{2.19}$$

Substituting (2.19) into (2.17) gives

$$-\frac{\hbar^2}{2m^*}\frac{\partial}{\partial x^2}\psi(x) + \frac{\hbar^2}{2m^*}\left(k_y^2 + \frac{2Bxek_y}{\hbar} + \frac{e^2B^2}{\hbar^2}x^2\right)^2\psi(x) = E\psi(x). \tag{2.20}$$

By inspection of the middle bracket, the expression can be factorised down to,

$$\left(k_y + \frac{eBx}{\hbar}\right)^2, \tag{2.21}$$

and by defining

$$x_0 = -\frac{\hbar k_y}{eB} \quad \text{and} \quad \omega_c = \frac{eB}{m^*}, \tag{2.22}$$

gives

$$\left[-\frac{\hbar}{2m^*}\frac{d^2}{dx^2} + \frac{1}{2}m^*\omega_c(x - x_0)\right]\psi(x) = E\psi(x). \tag{2.23}$$

This final result is of the same form as the 1D quantum mechanical simple harmonic oscillator equation, with the motion centred at the point x_0 with natural frequency ω_c. The eigenvalues E_n are therefore given by,

$$E_n = \left(n + \frac{1}{2}\right)\hbar\omega_c. \tag{2.24}$$

The motion of the electrons in the (x, y) plane is now completely quantised into these oscillator like energy levels known as Landau levels (LLs). This result, the DOS for the 2DES in a magnetic field is shown in figure 2.4, and is similar to the zero field 0D density of states. In ideality, the DOS is characterised by a series of δ-functions separated by $\hbar\omega_c$, which are shown to be degenerate, in figure 2.4.

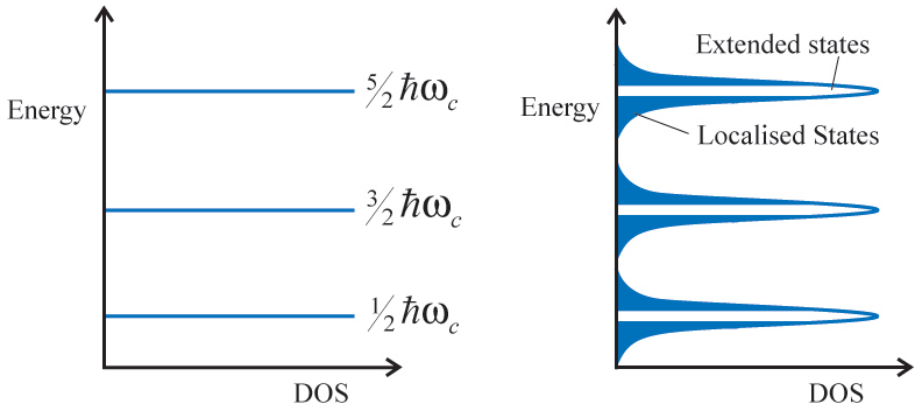

Figure 2.4: The theoretical density of states for a 2DES in a magnetic field (left), and broadened levels due to disorder and temperature, consisting of both localised and extended states (right).

The eigenfunctions for equation 2.23, the one dimensional simple harmonic oscillator

are of the form [21],

$$\psi_n(\xi) = C_n H_n(\xi) \exp(-\xi^2/2), \tag{2.25}$$

where C_n is a normalising constant and H_n is the Hermite polynomial in ξ of order n. The wavefunction 2.19 can now be rewritten as,

$$\psi_{\mathrm{n}\xi_0}(\xi, y) = C_{\mathrm{n}} \exp[ik_y y] \exp\left[\frac{1}{2}(\xi - \xi_0)^2\right] H_{\mathrm{n}}(\xi - \xi_0), \tag{2.26}$$

by introducing the quantity,

$$\xi = x\sqrt{\left(\frac{m^*\omega_c}{\hbar}\right)}. \tag{2.27}$$

This means the eigenfunctions depend on ξ_0 and k_y, as well as n. However ξ_0 and k_y are related through equation 2.22, so the state represented by (2.25) can be characterised by two quantum numbers n and x_0. The Landau level energy given in equation 2.24 depends only on n, so the LLs are degenerate, and states with the same n but different x_0 have the same energy. The degree of degeneracy of a Landau level is the number of possible values of x_0, and this depends on the number of different values of k_y. For a sample of width L_y the allowed values of k_y are separated by $2\pi/L_y$. The allowed values of x_0 are therefore separated by,

$$\Delta x_0 = \frac{\hbar}{eB}\Delta k = \frac{\hbar}{eB}\frac{2\pi}{L_y} = \frac{h}{eBL_y}, \tag{2.28}$$

which means the number of values of x_0 in a sample of length L_x is the nearest integer less than,

$$n_{max} = \frac{L_x}{\Delta x_0} = L_x L_y \frac{eB}{h} = \frac{\Phi}{h/e}, \tag{2.29}$$

where Φ is the total magnetic flux through the sample. The degeneracy factor per unit area is therefore,

$$n = \frac{n_{\max}}{L_x L_y} = \frac{eB}{h}. \tag{2.30}$$

It can be seen that the degeneracy is linearly dependent in B. The Landau level filling factor, ν, is defined as the number of filled LLs at a given magnetic field. This

is essentially the number of electrons divided by the degeneracy of a Landau level.

$$\nu = \frac{n_e h}{eB} \tag{2.31}$$

2.2 Oscillating Magnetic Moment - the de-Haas—van Alphen effect

At $T = 0\,\mathrm{K}$ in an ideal 2DES with no disorder, the DOS is a series of $\delta-$functions separated by $\hbar\omega_c$. A plot of these Landau-level energies against B is depicted in figure 2.5. As the magnetic field B increases, the degeneracy also increases, allowing more electrons to fit into lower states, causing the Fermi level of the system to oscillate in a sawtooth like pattern.

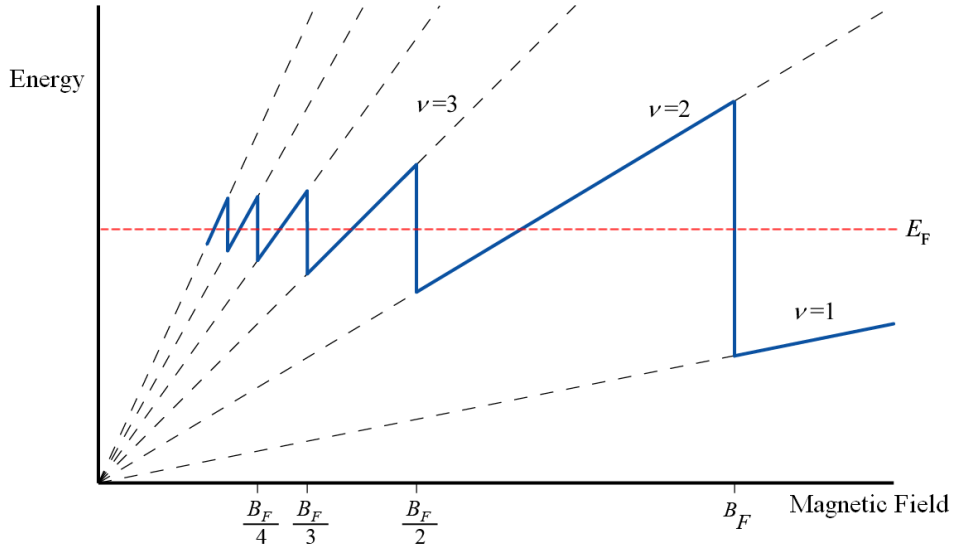

Figure 2.5: Oscillation in the Fermi energy due to Landau level quantisation.

At high magnetic fields there is a high degeneracy and all of the electrons can can occupy the lowest energy level, therefore the Fermi energy is also pinned to this level. As B is decreased, there is a critical 'fundamental' field where this state is completely filled, beyond which the electrons are promoted to a higher level, this first critical value is B_F . At this point the Fermi energy jumps abruptly as electrons

jump into the higher state. Decreasing the magnetic field further, the degeneracy of each LL decreases, and electrons again seek higher energy states to occupy (at points periodic in inverse magnetic field), again, E_{F} jumps at these points. The magnetoresistance (Shubnikov—de-Haas) oscillations which can be inferred from this only give information relating to the extended states and do not address the full problem of describing the broadening of the Landau levels. In order to measure the entire density of states a thermodynamic measurement is required, such as magnetisation or heat capacity. If the Fermi energy lies within a partially filled Landau level, the internal energy at this point is given by

$$U = g \sum_{i=0}^{\lambda-1} \left(i + \frac{1}{2} \right) \hbar\omega_{\mathrm{c}} + \left(\lambda + \frac{1}{2} \right) \hbar\omega_{\mathrm{c}} (n_{\mathrm{e}} - \lambda g), \tag{2.32}$$

where the degeneracy $g = eB/h$, n_{e} is the number density of electrons, i is the LL index and λ is the uppermost LL.

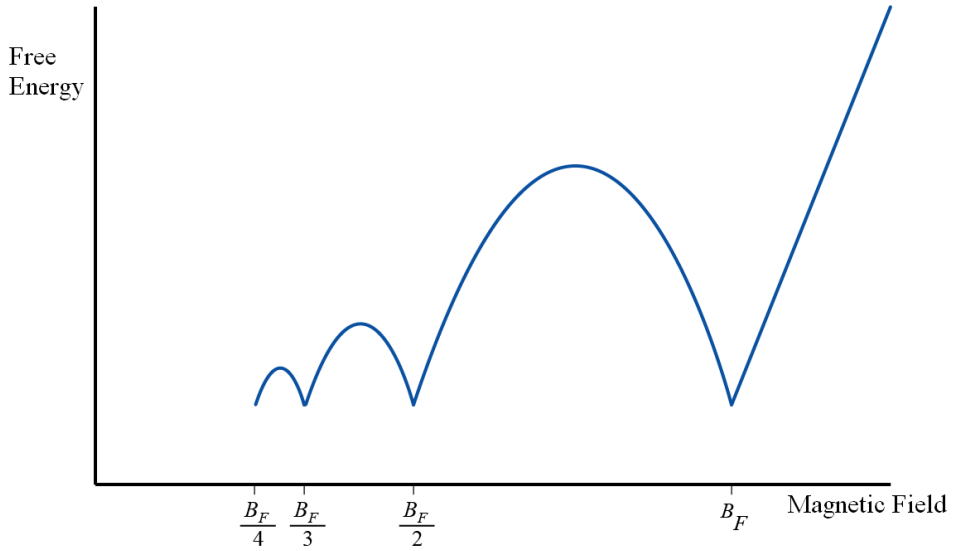

Figure 2.6: Oscillations in the Free energy due to a varying magnetic field B.

Figure 2.6 illustrates the shape of the free energy oscillations. Above B_{F}, the point at which the first Landau level is completely filled, the free energy is linear in B, and passes through zero. Decreasing magnetic field from a value $B > B_{\mathrm{F}}$, will decrease ω_{c} and the degeneracy linearly, until B_{F} is reached. Below this critical point the oscillations resemble a series of upside down parabolas, predicted by equation 2.32. At

the sharp cusp at B_{F}, the electrons have filled a LL completely. At each subsequent filling factor the free energy experiences another cusp as electrons occupy higher LLs. The free energy is not an easy quantity to measure by conventional methods, but there is an indirect way, by considering the definition of the Helmholtz free energy:

$$F = U - TS, \tag{2.33}$$

where the form of the internal energy of the system,

$$dU = dQ + dW, \tag{2.34}$$

and,

$$dQ = TdS. \tag{2.35}$$

The work done in a magnetic system can be written as,

$$W = MdB, \tag{2.36}$$

and by differentiating F and substituting in the first law of thermodynamics, equation 2.34, it is shown that,

$$dF = TdS - MdB - TdS - SdT. \tag{2.37}$$

In the limit that $T \rightarrow 0$ only one term remains, which can be re-arranged to give the magnetisation M,

$$M = -\left(\frac{\partial F}{\partial B}\right)\Big|_{n_{\mathrm{e}},T} \tag{2.38}$$

This is an interesting result; the magnetisation of a system can be measured by probing the free energy, and therefore is a thermodynamic quantity also. The magnetisation of a 2DES can be readily measured; by placing it at an angle in an applied magnetic field, and measuring the resulting torque. Differentiating the curve shown in figure 2.6 it is seen that the oscillations are of equal amplitude and periodic in $1/B$ as shown in figure 2.7, the steep jump is on the high field side.

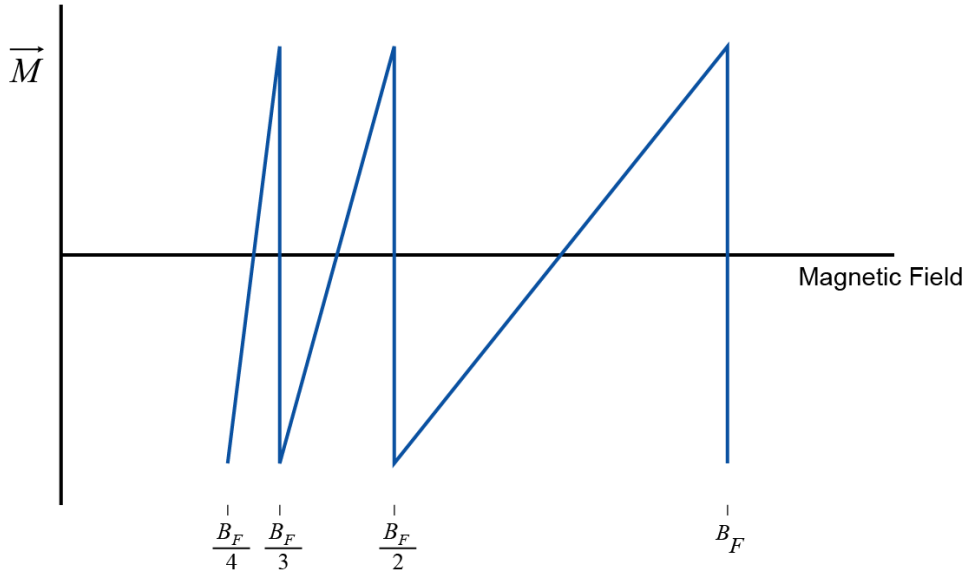

Figure 2.7: Oscillations in the magnetisation of a 2DES in a magnetic field, the de-Haas—van-Alphen effect.

2.3 Oscillating Heat Capacity

The heat capacity is an important quantity in terms of the physics of a system, since the internal energy, U, is impossible to measure directly. A useful experiment is a determination of $\partial U/\partial T$ as a function of temperature. This is another means by which to measure a fundamental thermodynamic quantity of a 2DES, and it can be shown that the electronic contribution to the specific heat capacity C_{el} is dependent on the two-dimensional DOS as in (2.41). As discussed earlier, applying a magnetic field to a 2DES will cause quantisation of Landau levels. A sweeping magnetic field not only causes oscillations in the magnetisation, but also of the specific heat. There have been several theoretical treatments, some workers calculated a specific heat based on a DOS taken to be a sum of Gaussian peaks [22, 23] and others which take into account a self consistent level broadening effect [24] which is in agreement with the $B-$dependent oscillations that Wang et al. [11] infer on the basis of their specific heat data. Zawadzki and Lassnig [24] assumed the same form for the DOS as later used by Potts et al. [25] for Gaussian broadened Landau levels, but they neglected the dependence of broadening on magnetic field. The electron concentration in a

unit area of the layer is calculated by introducing the Fermi distribution f, to the DOS to give,

$$N = A\sum_{n}\frac{2}{\pi}\frac{1}{\gamma}\int_{0}^{\infty}\frac{1}{1+e^{z-\eta}}e^{-2\gamma_n^2}dz, \tag{2.39}$$

where the reduced quantities are denoted,

$$A = \left(\frac{1}{\pi}\right)\left(\frac{eB}{\hbar}\right),\ \gamma_n = \frac{(z-\theta_n)}{\gamma},\ z = \frac{E}{k_{\mathrm{B}}T},\ \eta = \frac{E_{\mathrm{F}}}{k_{\mathrm{B}}T},\ \theta_n = \frac{\lambda_n}{k_{\mathrm{B}}T}\ \gamma = \frac{\Gamma}{k_{\mathrm{B}}T}, \tag{2.40}$$

where Γ is a broadening parameter. The specific heat is given in general as [26],

$$C_{\mathrm{el}} = \frac{df}{dT}(E - E_{\mathrm{F}})\mathrm{D(E)} \tag{2.41}$$

in which,

$$\frac{df}{dT} = -\frac{\partial f}{\partial E}\left(\frac{E-E_{\mathrm{F}}}{T} + \frac{\partial E_{\mathrm{F}}}{\partial T}\right). \tag{2.42}$$

The dependence $\partial E_{\mathrm{F}}/\partial T$ at constant concentration is determined by differentiating equation 2.39 with respect to T and using (2.42), leads to

$$\frac{\partial E_{\mathrm{F}}}{\partial k_{\mathrm{B}}T} = -\frac{L_1}{L_0} \tag{2.43}$$

and

$$C_{el} = kA\left(L_2 - \frac{L_1^2}{L_0}\right) \tag{2.44}$$

where

$$L_{\mathrm{r}} = \sum_{\mathrm{n}}\sqrt{\frac{2}{\pi}}.\frac{1}{\gamma}\int_{0}^{\infty}\frac{e^x}{(1+e^x)}x^r e^{-2\gamma_n^2}dz \tag{2.45}$$

in which $x = z - \eta$. Zawadzki and Lassnig calculated the heat capacity for a 2DES, assuming a broadening $\Gamma = 0.5\,\mathrm{meV}$ and an electron density $N = 8\times10^{11}\,\mathrm{cm}^{-2}$, figure 2.8 depicts the Fermi energy as a function of magnetic field at $T = 6\,\mathrm{K}$, and also the specific heat of the 2DES for the same temperature.

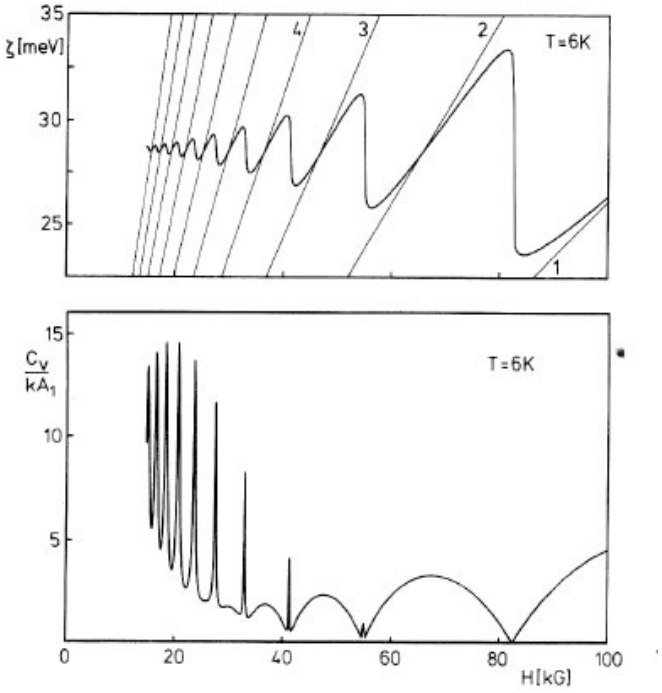

Figure 2.8: Oscillations in the Fermi energy give rise to an oscillating heat capacity, calculated by Zawadzki and Lassnig [24]. There are two contributions, an intra-LL contribution, and an additional inter-LL contribution in the form of spikes.

The specific heat is seen to consist of two contributions. At high magnetic fields where $\hbar\omega_c >> k_B T$ only the intra-level excitations contribute to the heat capacity. When the Fermi energy is between two Landau levels, the lower ones completely full and the upper ones completely empty, C_{el} vanishes. At weaker magnetic fields there is an inter-level contribution in the form of sharp spikes. These contributions are observable in the low field range if the temperature is not too low, and arise when the Fermi energy lies between two Landau levels. Zawadzki and Lassnig suggested that the rise of this contribution with decreasing magnetic field follows the general behaviour of C_V for two-level systems. Figure (2.8) illustrates a continuous transition of the specific heat from the intra-level to the inter-level behaviour with changing magnetic field.

2.4 The form of the density of states

In the 1980s Eisenstein et al. [13] used a torsion magnetometer design to investigate the de-Haas—van-Alphen (dHvA) oscillations, and found a substantial DOS between levels. Comparison with heat capacity measurements of the time by Gornik et al. [12], showed agreement on the issue of residual DOS between Landau levels. However, evidence was not found for the relatively narrow structures atop the constant background cited by Gornik et al. [12]. The authors claimed, due to the differences and complexity of the model used, a direct comparison could not be made. Since then there has been much investigation into the properties of 2DES utilising magnetisation. Potts et al. [25] investigated dHvA oscillations in the previously unobtainable temperature range 0.125 K–4.2 K, with a large magnetic field range up to 15 T. They concluded that at high B the DOS can be described by a series of Lorentzian broadened Landau levels with a broadening that is independent of B, and level index n. However at low B the Lorentzian becomes indistinguishable from a Gaussian with broadening that is proportional to $B^{1/2}$. They considered two different models for the DOS, $g(E, B)$, each of which assumes a periodic array of Landau levels with the broadening of each level being independent of the Landau level index, n. The first model assumes the broadening to be Gaussian with the DOS given by,

$$g(E,B) = \frac{2eB}{h}\frac{1}{\Gamma\sqrt{2\pi}}\sum_{n=-\infty}^{\infty}\exp\left(-\frac{(E-E_n)^2}{2\Gamma^2}\right) \tag{2.46}$$

where E_n is the energy of the Landau level of index n given by equation 2.24 previously. The LL broadening, Γ, is assumed to be a function of magnetic field, B, with

$$\Gamma(B) = \Gamma_0 B^P, \tag{2.47}$$

where $P = 0$ or $P = 1/2$. The second model to be considered assumes a Lorentzian-broadened DOS defined by,

$$g(E,B) = \frac{2eB}{h}\frac{1}{\Gamma\sqrt{2\pi}}\sum_{n=-\infty}^{\infty}\exp\left(-\frac{\Gamma}{(E-E_n)^2+\Gamma^2}\right). \tag{2.48}$$

Several authors have reported the existence of a constant background to the density of states [12, 17]. The background can be characterised by a parameter ξ representing the magnitude of the background density of states as a fraction of the zero-field DOS. This can be incorporated into the model,

$$g'(E,B) = \xi\frac{m^*}{\pi h^2} + (1-\xi).g(E,B) \quad (0 \leq \xi < 1). \tag{2.49}$$

By assuming the Gaussian and Lorentzian models to be periodic and symmetric about $E = 0$ it is possible to express both models as Fourier series. This is not done here, but in both cases the background parameter has the effect of reducing the amplitude of the oscillations by a factor $(1 - \xi)$. Potts et al. incorporate these DOS into a model for the magnetisation that is an extension of that proposed by Shoenberg [27], that is, to include LL broadening and the effect of background DOS. Figure 2.9 shows a plot of the DOS of a 2DES in GaAs as a function of electron energy E, at a constant magnetic field B, for both Lorentzian broadened LLs with $\Gamma = 2.16\,\text{meV}$ (solid line) and Gaussian broadened levels with $\Gamma = 1.09\sqrt{B}\,\text{meV}$ (dashed line) for $B = 8T$.

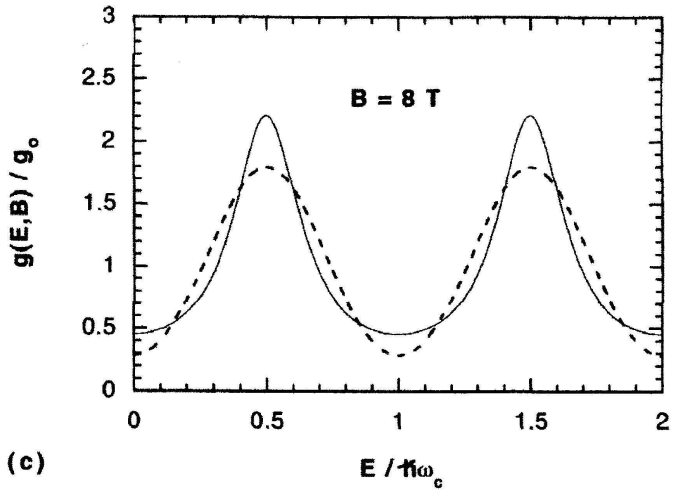

Figure 2.9: DOS $g(E, B)$ calculated for a 2DES in GaAs for Lorentzian broadened LLs (solid curve) and Gaussian broadened LLs (dashed curve), after Potts et al. [25].

Potts et al. [25] found no evidence to support the theory that the broadening oscillates with field due to changes in electron screening as suggested by some workers [11]. They concluded that at high B, the Lorentzian with no B dependence proved the best fit. They attributed the quality of fit to the greater sensitivity of their equipment and the low temperature capability of the modern day, as well as an improved background removal and calibration procedure. Taking the work further, Zhu et al. [28] were able to investigate the temperature range 50 mK to 1 K. Apart from the shape of the Landau levels, the existence of an absolute gap between two adjacent LLs was again questioned. It was found that a constant background still had to be introduced to account for the discrepancy between theory and result. Multilayer samples are commonly used to enhance the weak signal, as a result the line shape may be influenced by interlayer inhomogeneities. Improvement to the technique has meant single layer investigations possible such as Wiegers et al. [29], who used a heat capacity method.

Zhu et al. modified the potentials used by Potts et al. Assuming the 2DES is an ideal non-interacting Fermi system in which spin splitting is ignored, the thermodynamic

potential per unit area Ω at the temperature T is given by,

$$\Omega(B,T) = kT \int_0^\infty dE.D(B,E).\ln\left(1 - \frac{1}{1+\exp\left(\frac{E-E_\mathrm{F}}{kT}\right)}\right) \tag{2.50}$$

Assuming n_e is fixed, the energy Ω is determined by the position of the Fermi energy, which oscillates with the applied magnetic field. The magnetisation of the 2DES is given by,

$$M(B,T) = \left(\frac{-\partial\Omega(B,T)}{\partial B}\right)\Bigg|_{E_\mathrm{F},\mathrm{T}}. \tag{2.51}$$

This calculated magnetisation is then fitted to the experimental data using either model DOS, with n_e, Γ, and ξ being treated as fitting parameters. An effective electron mass of $0.0667m_\mathrm{e}$ is also assumed. A scaling factor S is applied to M and allowed to vary within $\pm 10\%$ of the calibration obtained from the calibration coil. A discussion on the effects of these parameters is given in Zhu et al.. The authors reported widths of $(0.1 - 0.4\,\mathrm{meV})$ which were much smaller than in the study of Potts et al., this is attributed to better quality heterojunctions. Zhu et al. found that a Lorentzian or Gaussian fits equally well with no B dependence. This agrees with Potts et al. who favoured a Lorentzian fit. However Zhu et al. had to invoke a significant background density of states between LLs which is larger when the Gaussian shape is assumed (up to 49%), which although sounds large, is consistent with some earlier experiments which attributed it to impurities and sample inhomogeneity [12, 13]. This contrasts Potts et al., suggesting the constant background is associated with the higher sample quality, or that the relatively broader Lorentzian fits used in the study include a large number of states between LLs without the need to introduce a background. This feature makes the Lorentzian a favourable choice. They noted that no amount of adjusting the other parameters can yield a satisfactory fit to the data – only a non zero ξ.

In contrast to the large number of magnetotransport and magnetoptical experiments reported for 2DESs in the QHE regime, few heat capacity measurements have been reported so far. Calorimetry measurements of samples as small as 500 mg in the range $\sim 1 - 35\,\mathrm{K}$ were developed by Bachmann et al. [9] before the discovery of

the QHE. Gornik et al. [12] developed the technique further and reported the first observation of magnetic field dependent electronic specific heat in a GaAs-GaAs multilayer. As well as the expected intra-level contribution, additional spikes were observed for 4.2 K and 5 K as a result of inter-level contributions. This was confirmed through their temperature dependence, they are only present at higher temperatures in agreement with theory [22, 24]. These results were compared against predicted results for different models, Gaussian, Lorentzian and a Gaussian with constant background for which they favoured the latter. Wang et al. [11] shortly after presented results which dispute those of Gornik et al. [12], the data could not be fitted assuming B-independent level broadening. The search for an adequate fit lead them to conclude that the level widths oscillated with a variation in B. Wang et al. proposed that the level width is larger when E_{F} lies between Landau levels than when it coincides with one. The difference in widths greatened at higher B (smaller ν). They suggest the results supported a model in which screening of the scattering potential and the energy-level broadening influence each other self-consistently but do not offer a more detailed explanation. At 2 K no oscillatory features in the data were observed despite magnification and subtraction of partial fits to background signals. Below 2 K small $1/B$ oscillations were visible, but only after subtraction of fits to background and magnification, with a maximum contribution of C_{el} amounting to only 0.1%. This amount does not compare well with Gornik et al. measuring a signal of $\sim 1 - 10\%$. Fitting a constant broadening to the data resulted in a line shape qualitatively different from their data. Another disparity between results with Gornik et al. was the maxima in heat capacity were distinctively sharper than the minima, although comment is made no explanation is offered. Wang et al. however state that they do not determine an absolute value for C_{el}: just measure a variation between minima and maxima, in which they assume a zero background DOS which has been shown to be an inadequate assumption by current magnetisation work. Another discrepancy between these two workers is with regard to the interlevel spikes. Above 4 K in a very similar sample Gornik et al. observed interlevel spikes at low B (2 T) of size $\sim 0.03 - 5\%$ of C_{tot} as predicted [22, 24]. However, in an average of 30 sweeps from 0 to 5 T at 4.6 K, Wang et al. observed no spikes. Within their experi-

mental resolution the absence of inter-level contributions is claimed to be consistent with their model of a B-dependant broadening. The most recent heat capacity measurements [10, 30] have used a combination of the different techniques, at low B, where the relaxation time $\tau_{\text{ext}} \sim 0.1\,\text{s}$, heat capacity was measured using an AC technique similar to Wang et al. Near $\nu = 1$ where heat capacity had increased by several orders of magnitude, they turned to the pulse technique. Although these workers detected a T dependence of the heat capacity near $\nu = 1$, which they did not expect to find in the GaAs/(Al,Ga)As structure, they attribute it to a Schottky nuclear heat capacity. Little was inferred about the form of the DOS.

2.5 The Hall effect

The classical Hall effect, which was first observed by Edwin Hall in 1879 [31], describes what effect crossed electric and magnetic fields have on the trajectory of charged particles. Nowadays, the use of the effect is common place in the measurement of magnetic fields, characterising semiconductors, motion sensing devices.

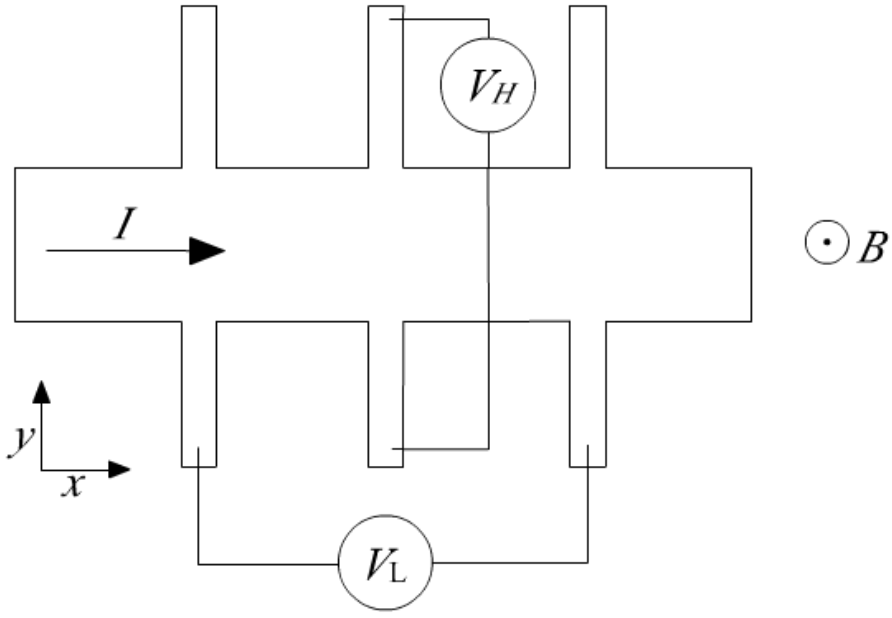

Figure 2.10: Hall bar geometry of a 2DES. A magnetic field B is applied perpendicular to the plane and the direction of current flow. The voltmeters indicate the longitudinal and Hall voltages.

The geometry of a Hall bar experiment is depicted in figure 2.10. A small current I is passed along the Hall bar, and voltmeters connected to ohmic contacts measure voltage drops parallel and perpendicular to the current flow. These are often referred to as the longitudinal (V_{L}) and Hall (V_{H}) voltage. If a magnetic field, B, is applied perpendicular to the plane of the 2DES, the Hall voltage is found to be directly proportional to the magnitude of the field,

$$V_{\mathrm{H}} = \frac{IB}{en_s}, \tag{2.52}$$

where e is the charge of the electron, and n_s is the number density of the 2DES. This effect can be explained by classical electrodynamics. An electron with charge e, propagating through the conducting material with velocity v_x in the $x-$direction, is deflected by a Lorentz force in the $y-$direction. The magnitude of this force is given by,

$$F = -e(V_{\mathrm{H}} + v_x B). \tag{2.53}$$

This force creates a build up of charge on one side of the material, until the force is balanced. From inspecting the bracket of equation 2.53, V_{H}, must therefore be proportional to B. The resistances are defined as,

$$R_{\mathrm{L}} = \frac{V_{\mathrm{L}}}{I} = \rho_{xx}\left(\frac{L}{W}\right), \tag{2.54}$$

and

$$R_{\mathrm{H}} = \frac{V_{\mathrm{H}}}{I} = \rho_{xy}. \tag{2.55}$$

In 2D, the resistance and the resistivity have the same dimension. The conductivities can be obtained from the measured resistivity's through the tensor relations,

$$\sigma_{xx} = \frac{\rho_{xx}}{\rho_{xx}^2 + \rho_{xy}^2}, \tag{2.56}$$

and

$$\sigma_{xy} = -\frac{\rho_{xy}}{\rho_{xx}^2 + \rho_{xy}^2}. \tag{2.57}$$

In a Hall effect measurement, the Hall resistivity is the same value as the Hall

resistance, and in a Corbino geometry experiment, where a known voltage is applied between two concentric rings Dolgopolov et al. [32], the longitudinal conductivity is measured directly by measuring the radial current.

2.6 The integer quantum hall effect

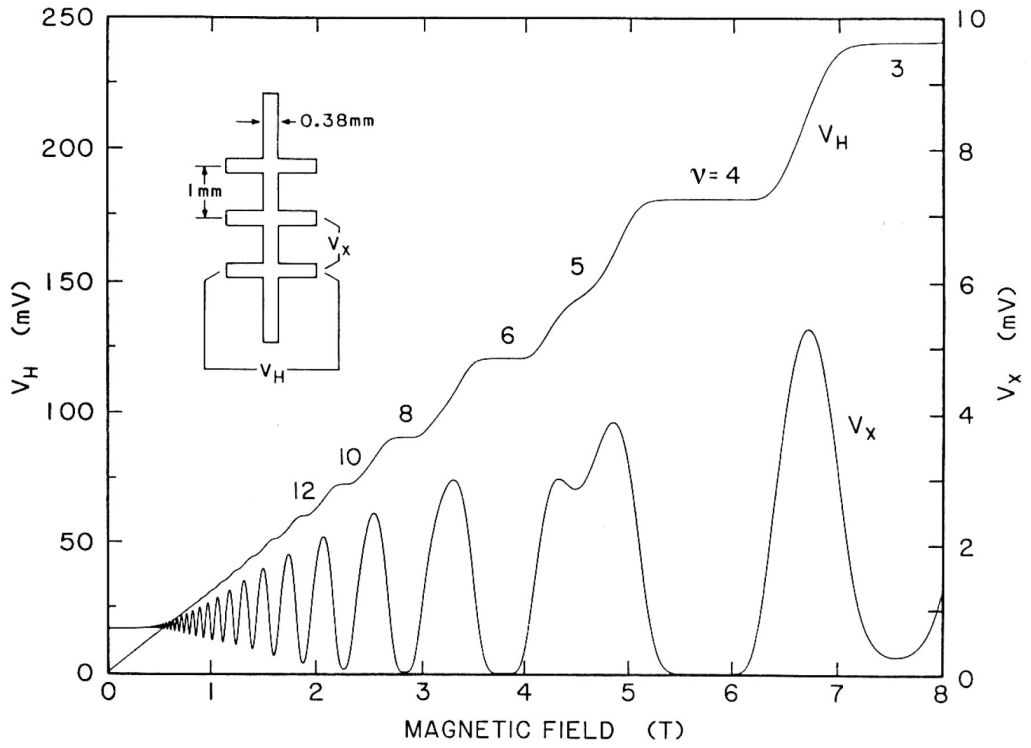

Figure 2.11: Experimental data of the quantum Hall effect, characterised by deep resistance minimum in the longitudinal voltage drop, and quantised plateaux in the Hall voltage, from Cage [33].

The integer quantum Hall effect (IQHE or sometimes referred to as the QHE) was not discovered until over a hundred years later by von Klitzing et al. [1]. The discovery was so significant it was awarded the Nobel prize in physics in 1985, and was a fantastic demonstration of a macroscopic quantum phenomena. The IQHE requires low temperatures and high magnetic fields to be observed in a GaAs/(Al,Ga)As 2DES, but recently was measured in a single atomic layer of carbon, graphene, at room temperature by Novoselov et al. [34].

Returning to the GaAs/(Al,Ga)As system, at low temperature and high magnetic fields, 'the quantum Hall regime', the Hall conductivity exhibits a series of plateaus which are quantised:

$$\sigma_{xy} = \frac{-ie^2}{h} \tag{2.58}$$

where i is a positive integer (equal to the Landau level filling factor), e is the charge of an electron and h is Planck's constant. The quantisation was shown to be accurate to better than one part in ten million, and is independent of sample geometry, the material the system is made from and the quality of the sample. The plateaus (regions where the Hall voltage is constant) are accompanied by minima in the longitudinal resistivity, $\rho_{xx} \rightarrow 0$. This results in an almost dissipationless flow of current, and by using equation 2.56, the Hall resistivity is shown to be,

$$\rho_{xy} = \frac{h}{ie^2}. \tag{2.59}$$

The near dissipationless state of the 'zero-resistance' minima is discussed more, and investigated in chapter 4. The Hall resistance plateaus arise from disorder, which results in localised states between Landau levels. In the limit of zero disorder with a uniform electron density, at discrete values of filling factor, there would be no states and the Fermi level would jump from one level to another, reducing the plateaus to discrete points. The extent to which this affects the plateaus is discussed by Luryi and Kazarinov [35].

2.7 Edge States

As already discussed, when a perpendicular magnetic field is applied to a 2DES, the electrons undergo cyclotron orbits. Near the edge of the sample these form skipping orbits which move in opposite directions on the two Hall bar edges, but without an applied potential do not carry any current. The skipping orbit picture is discussed further when debating quantum point contact conduction mechanisms in chapter 5, and can be seen in figure 5.12. Halperin [36] extended on the analysis of Laughlin

[37] on conduction in the QHE, and showed that the states at the edge of the sample are current carrying quasi-one-dimensional states, which remain extended in the presence of a disordered potential. In the bulk, edge states lie below the Fermi level, but rise in energy as the edge of the sample is approached.

The number of edge channels at E_{F} is equal to the number of bulk Landau levels below E_{F}, the example in figure 2.12 depicts the $n = 3$ Landau level being partially full. The Fermi energy crosses Landau levels at the edge to form extended states, and localised states encircling potential maxima and minima in the bulk. Beenakker [38] was the first to give a qualitative edge channel picture, dividing the electron gas into alternating compressible and incompressible strips, the idea has been developed further by other workers such as Chklovskii et al. [39]. As the bulk is approached from the edge, the chemical potential moves step-wise through regions of contant ν, and regions which do not lie in an energy gap. The former regions are considered incompressible and extend the length of the sample. The later, compressible bands, may be identified as edge channels, and essentially originate from the discontinuities of the chemical potential dependence on filling factor $\mu(\nu)$. There is still a lacking of consensus as to the dimensions and positions of these strips, but knowledge of them is required to explain various transport experiments, such as the population of edge states in a quantum point contact measurement, as discussed in chapter 5. Distribution of the current carrying states, and their breakdown is discussed further in chapter 4.

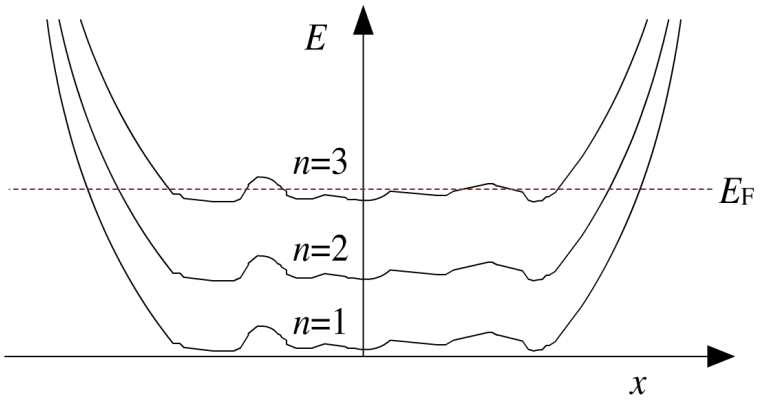

Figure 2.12: Edge channels form in a disordered potential. The energy of the edge state increases as the edge of the sample is approached. As the Fermi energy is increased, more Landau levels contribute to the conduction. In this example, the $n = 3$ level is partially full and there are states occupied in the bulk. Image after Beenakker and van Houten [40].

Chapter 3

Experimental Details

3.1 Introduction

In order to observe phenomena associated with the quantum Hall effect discussed in chapter 2, low temperatures and high magnetic fields are required. This chapter gives details of the two cryogenic systems used. A brief summary of the torque magnetometry technique is described, as are the common calorimetry measurement methods. As chapter 6 is largely a design discussion chapter, specific details will be left until later.

3.2 The Dilution Refrigerators

3.2.1 Oxford Instruments Refrigerator System

The Oxford Instruments (OI) refrigerator (Kelvinox AST200) is housed in a OI Dewar. The Dewar has a 77 K cold shield which has a capacity of 120 L, and a helium bath also of 120 L. The magnet has a bore of 52 mm, with an inductance of 96.6 H. The maximum guaranteed field at 4.2 K is 17 T (corresponding to 105.9 A), and with the lambda plate in operation at 2.2 K it is 19 T. The homogeneity over a

10 mm diameter spherical volume is 1 part in 10^3. In persistent mode the decay of the magnet current is 1 part in 10^4 per hour. The magnet is bolted to the bottom of the cryostat, unlike the Cryogenics Consultants magnet, which is suspended from the top of the cryostat. This system is therefore the less susceptible to mechanical noise arising from the magnet. The magnet power supply is an OI IPS 120-20.

The OI fridge does not use conventional mechanical pumps to circulate 3He, but uses adsorption pumps instead. Granulated charcoal is kept cold at ~ 2 K by pumping 4He from the main bath, and provides a large surface area above the still which the 3He can adsorb to. The adsorption pumps give a high pumping speed, are small so can be placed near the still without large pumping lines, and have no moving parts (except for a pneumatic valve). The disadvantage of the pumps is that they are single-shot, they cannot pump once the entire surface has adsorbed gas. By having two pumps the fridge can be run in a continuous mode: they are both connected to the still via a pneumatic cryovalve, whilst one is pumping the other is heated to 40 K so that the He-mixture desorbs, and is then re-liquefied in the 1 K pot. The liquid then enters the collector, which acts to turn the on/off pumping into a constant flow of 3He into the condenser line. The disadvantage is that the mechanical measurement of magnetometry is so sensitive that it is perturbed by the operation of the pneumatic valve opening/closing, so for detailed runs the fridge has to be run in a single shot mode. The maximum operation time of a single shot mode before the still is completely emptied and the temperature of the mixing chamber starts to drift upwards is ~ 12 to 24 hours.

The temperature is controlled by an OI Kelvinox AST temperature controller with a 2.2 kΩ ruthenium oxide thermometer [41] at the top of the mixing chamber, and several Allen Bradley resistors for diagnostic purposes.

3.2.2 Cryogenic Consultants Limited dilution refrigerator

This fridge is housed in a Cryogenic Consultants Limited (CCL) cryostat. The CCL cryostat contained a superconducting solenoid with a bore of 40 mm and an

inductance of 32 H. The high field solenoid can produce fields of 15.5 T at 4.2 K, and 16.8 T at 2.2 K through the operation of a lambda plate. At 15.5 T the current through the solenoid, from the CCL magnet power supply, corresponds to 107.6 A.

The CCL refrigerator is an entirely plastic mixing chamber below the cooling loop. The plastic construction minimises eddy current heating which would be present in the mixing chamber walls. The 3He is circulated by a Leybold TRIVAC S40B 3He sealed rotary pump, and an Edwards roots blower booster pump. The refrigerator cooling power at 100 mK is $\sim 300\,\mu$W, and the base temperature is ~ 50 mK.

The temperature can be controlled by a Neocera LTC-21 temperature controller using a Ge thermometer in the plastic mixing chamber. An additional RuO_2 resistor with a lower magnetoresistance than that of the Ge, was fitted when using the cold finger, calibrated against the RuO_2 thermometer in the OI refrigerator.

3.3 Vibration Damping

Matthews et al. [6] demonstrated that the noise limitation in the magnetometry arrangement was mechanical, so a two stage inertial damping arrangement was used. Each cryostat was attached to a large concrete mass, attached to an even larger mass through a thick layer of rubber. The larger mass is itself floating on air suspension springs. The air springs remove vibrations down to < 1 Hz, while the rubber is more effective at removing high frequencies. The total mass of the CCL cryostat, refrigerator and concrete is 8.5×10^3 kg, and of the OI arrangement is 2.8×10^4 kg. In the OI setup, due to the weight of the experiment, the large mass is supported by its own foundations separate from the building. The four air springs in each experiment are maintained by a typical pressure of 80 psi by a compressed air line that is smoothed by a main regulator, and a separate regulator for each spring.

3.4 Magnetometry

The technique of torque magnetometry, along with the detection electronics is described in more detail in [6]. The magnetometer consists of a rotor, and two stator capacitance plates (plates machined from phosphor bronze). The rotor is made from Stycast [42] with a gold film of $\sim 150\,\mathrm{nm}$ evaporated onto the back to act as a capacitance plate. The fibre is GE varnished [43] to a pad in the centre of the rotor, and connected electrically to the underside of the rotor via thin gold wire [44] contacted with silver-loaded paint [45]. The magnetometer is depicted in figure 3.1.

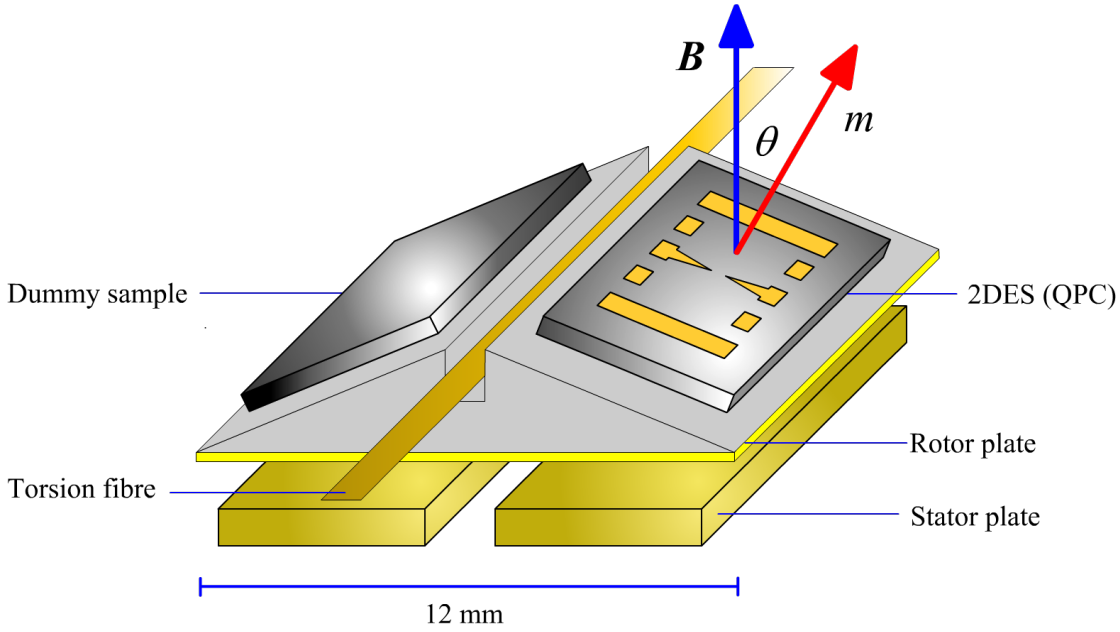

Figure 3.1: Torsion balance magnetometer. A magnetic field B causes a magnetic moment m in the sample (quantum point contact AK47 pictured without wires), which results in a torque that can be measured by a differential capacitive change. The sample is not to scale.

The magnetic moment of a two dimensional sample, caused by the application of a magnetic field B, is constrained to be perpendicular to its surface. The magnetic moment, m, at angle θ to the applied field, results in a torque,

$$\tau = m \wedge B = mB \sin\theta \tag{3.1}$$

A measurement of torque can be related to a magnetic moment of the sample, and

hence the magnetisation. Early generations of the magnetometer had a coil of 10 turns around a central pillar; by applying a current through the coil, a known magnetic moment gave a measure of the responsivity of the magnetometer. It was shown by Smith [46] that by making certain assumptions, an electrostatic force measurement agreed to within $\sim 1\%$ of the calibration coil technique. The magnetometer is significantly easier to assemble without a calibration coil, and also electrostatic coupling to the 2DES was reduced. By assuming that the plates are parallel, and that the deflection caused by an applied voltage V (applied between the rotor plate and one stator plate) is small compared to the separation, the force F on a capacitor plate is given by,

$$F = \frac{1}{2}\frac{C^2V^2}{\varepsilon_r\varepsilon_0 A}, \tag{3.2}$$

where C is assumed to be constant, and A is the area of the static plate. The torque τ can then be calculated, assuming the plates to be parallel by,

$$\tau = F.dl, \tag{3.3}$$

where dl is the distance from the centre of the rotor plate to the centre of the stator plate. This torque can then be plotted against a measured output from the capacitance bridge to give a responsivity calibration factor for the experiment. For more detail see Matthews et al. [6].

3.5 Calorimetry

The interest in measuring the heat capacity of a 2DES in a magnetic field has been discussed in chapter 2. The development of a calorimeter on the end of a cantilever is the topic of chapter 6, so experimental specifics will not be discussed here. There is more than one way to measure the heat capacity of a sample; adiabatic, relaxation and AC calorimetry all have been used to measure the heat capacity of the 2DES. The design of the cantilever-calorimeter is predicted to be best suited to a combination of an adiabatic and relaxation calorimetry method, depending upon

the measured relaxation times.

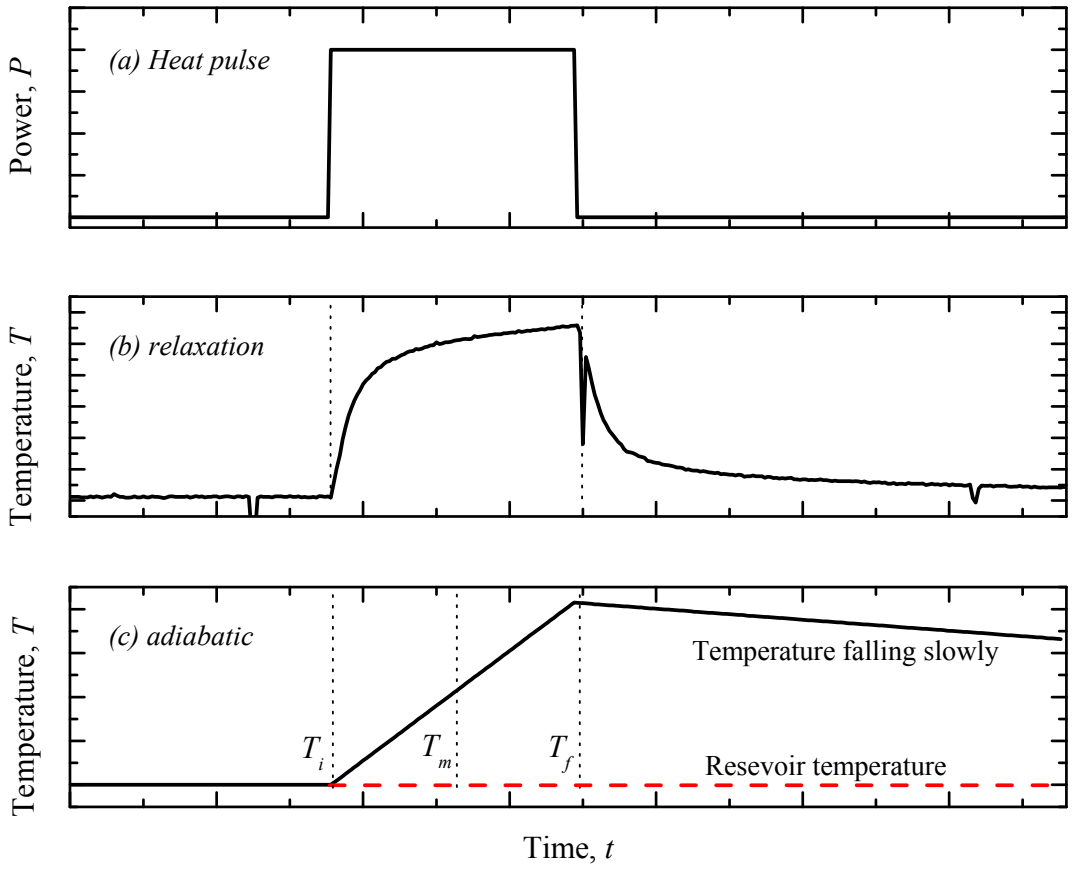

Figure 3.2: Heat-pulse calorimetry: A heat pulse (a) results in a thermometer response: (b) Measured response of a AuGe thin film resistor connected to a weak thermal link and (c) Predicted response in quasi-adiabatic conditions.

3.5.1 Adiabatic Calorimetry

The heat capacity of a sample can be measured from an input pulse of heat energy ΔQ, figure 3.2, causing a small temperature rise ΔT in a specimen of mass M

$$C_V = \left(\frac{\Delta Q}{\Delta T}\right)_V \tag{3.4}$$

Bachmann et al. [9] were among the first to use such a pulse technique to determine heat capacities of small masses, and it remains one of the best methods for obtaining specific heat data. The sample is contained in, or thermally connected to an

'addenda' consisting of the specimen support (bulk semiconductor), a thermometer, a resistive heater and any wires. The addenda/sample is thermally isolated from the surroundings (adiabatic conditions). Thermal equilibrium with the surroundings is established before and after the heat pulse ΔQ. The temperature is measured as a function of time. Such conditions could be realised for example, by suspending the calorimeter and sample in a vacuum by superconducting wires, which double as a weak thermal link to a constant temperature heat reservoir.

Figure 3.2 (c) shows the predicted response to a heat pulse, the temperature increase is $T_f - T_i$, from which C_V is obtained at the temperature T_m. Strictly adiabatic conditions occur only when there is no heat transfer between the calorimeter and the surroundings. After the heat pulse, the calorimeter will be at a temperature slightly above that of the reservoir, there will be a downward temperature drift, and experimental conditions are therefore actually 'quasi-adiabatic'. The calorimeter is heated by a series of heat pulses and the drift rates monitored before and after each heat pulse. Ideally ΔT is kept small. The reservoir temperature is kept constant at all times, although it is common to adjust the addenda with a heater before each data point is taken, to minimise drift corrections. In this technique the sample is in thermal equilibrium before and after each heat pulse There are some difficulties with this method: for small specimens such as a 2DES, the heat capacity of the addenda will be the largest portion, necessitating large addenda corrections which limit the accuracy of the heat capacity. There are limitations in that finite values of ΔT must be used, it may not be possible to resolve the fine detail of a phase transition if ΔT has a coarse resolution and the transition occurs over a small temperature range. Experimental calorimetry benefits greatly from advances made in electronic instrumentation, and the use of micro-lithography technology to form very small addenda. The measurement of the heat capacity will depend critically on the accuracy of the energy, time and temperature measurements. The whole arrangement relies on good thermal equilibrium within the calorimeter and a resistance thermometer that can accurately indicate the temperature of a specimen and has a small magnetic field dependence.

3.5.2 Relaxation Calorimetry

In this method the sample is connected by a weak thermal link to a thermal bath at a temperature T_0, as used by Forgan and Nedjat [47], and Bachmann et al. [9]. The temperature of the sample is raised by a small ΔT by a heat pulse, and then allowed to relax exponentially back down to the bath temperature, as shown in (b) of figure 3.2. The temperature of the sample is given by

$$T_s = T_0 + \Delta T \exp(-t/\tau_{\text{ext}}), \tag{3.5}$$

at a time t, and τ_{ext} is the relaxation time constant. The heat capacity is determined from a measurement of τ_{ext} and the thermal conductance of the weak link K,

$$C_P = \tau_{\text{ext}} K. \tag{3.6}$$

The experiment can be designed such that τ_{ext} is in the range desired, by adjusting the thermal link K, as this method relies on the assumption that the internal relaxation time, τ_{int} of the sample is faster than the relaxation time of the sample to bath, τ_{ext}.

3.5.3 AC Calorimetry

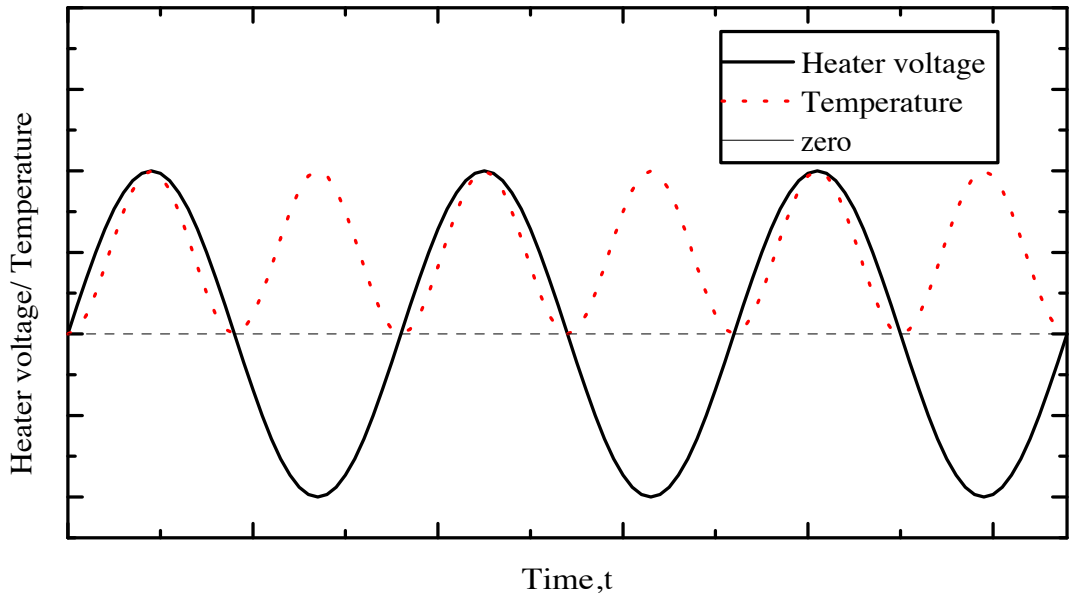

Figure 3.3: Ac calorimetry method. The measured heating is at twice the frequency of the applied heater voltage.

In 1968 Sullivan and Seidel [48] introduced a technique where the sample is heated by an ac current of frequency $\omega/2$ through a resistive heater. The peak to peak response, $T_{\rm ac}$, is measured by detecting the thermometer voltage across a resistance thermometer at a frequency ω, with a lock-in amplifier, as in figure 3.3, after Barron and White [49]. The total heat capacity, that of the 2DES and the addenda, C_P, can be calculated from,

$$T_{\rm ac} = \frac{\dot{Q}_0}{2\omega C_P}\left[1 + \frac{1}{\omega^2\tau_{\rm ext}^2} + \omega^2{\tau_{\rm int}}^2 + \frac{2K_{\rm bath}}{3K_{\rm sample}}\right]^{-1/2}, \tag{3.7}$$

where $\dot{Q}_0$ is the amplitude of the sinusoidal heat flux, $\tau_{\rm ext}$ is the sample to bath relaxation time, $\tau_{\rm int}$ in this case is the response time of the sample, heater and thermometer to the heat input, $K_{\rm bath}$ is the thermal conductance of the sample to the bath, and $K_{\rm sample}$ the thermal conductance of the sample. By careful choice of experimental conditions where $\tau_{\rm ext} << 1/\omega$, $\tau_{\rm int} >> 1/\omega$ and $K_{\rm sample} >> {\rm K_{bath}}$, it

has been shown by Stewart [50], that equation 3.7 can be simplified to

$$C_P \backsimeq \frac{\dot{Q}_0}{2\omega T_{\mathrm{ac}}}. \tag{3.8}$$

As with the other methods, the heat capacity has to be corrected for the addenda contribution. An advantage of this method is that complete thermal isolation is not a requirement. Due to the automation of the measurement, it can take place whilst varying a property of the system, such as magnetic field B at a constant rate.

3.6 The Samples

AK47

The sample AK47 is a single layer GaAs/(Al,Ga)As quantum well structure, delta doped with Si, with a measured mobility of $1.03 \times 10^6\,\mathrm{cm^2\,V^{-1}\,s^{-1}}$, grown at the Institute for Microstructural Sciences (within the group of Sachrajda), Canada and processed by Dr Alicia Kam. In Chapter 4 the number density is measured to be $2.01 \times 10^{11}\,\mathrm{cm^{-2}}$ through a Hall effect resistance measurement, below 1 K. The Layer profile can be seen in table 3.1.

Repeat	Thickness /Å	Material	Dopant
1	100	GaAs	
1	600	Al(0.33)GaAs	
1	5.6	GaAs	
1		delta	Si - $4 \times 10^{-12}\,\mathrm{cm^{-2}}$
1	5.6	GaAs	
1	400	Al(0.33)GaAs	
1	8000	GaAs (2DES at top)	
67	24	GaAs	
	24	Al(0.33)GaAs	
1	300	GaAs	
1	2500	Al(0.4)GaAs	
1	30	AlAs	
1	2000	GaAs	
Semi Insulating GaAs substrate			

Table 3.1: Layer profile of δ- doped heterojunction, sample AK47.

T621

Modulation doped heterojunction T621 was grown at the Cavendish Laboratory, Cambridge. A typical number density for such a structure would be $\sim 1.25 \times 10^{11}\,\mathrm{cm}^{-2}$ below 1 K. The Layer profile is shown in table 3.2.

Repeat	Thickness /Å	Material	Dopant
1	167	GaAs	
1	2000	Al(0.33)GaAs	Si - $1 \times 10^{17}\,\mathrm{cm}^{-3}$
1	800	Al(0.33)GaAs	
1	8000	GaAs (2DES at top)	
1	300	AlAs	
1	3000	GaAs	
1	50	GaAs	
1	50	Al(0.33)GaAs	
1	5000	GaAs	
(100) Semi-insulating GaAs substrate			

Table 3.2: Layer profile of modulation doped heterojunction, sample T621.

A3970

The sample A3970 is grown with an etch stop approximately 10 μm away from the top surface, in order to be made into a cantilever at a later stage. The growth layers are shown in table 3.3. The resulting number density and mobility were measured at liquid helium temperatures at Cambridge to be $n_s = 2.1 \times 10^{11}\,\mathrm{cm}^{-2}$ and $\mu = 3.258 \times 10^{6}\,\mathrm{cm}^{2}\,\mathrm{V}^{-1}\,\mathrm{s}^{-1}$ in the dark, and $n_s = 3.6 \times 10^{11}\,\mathrm{cm}^{-2}$ with $\mu = 2.960 \times 10^{6}\,\mathrm{cm}^{2}\,\mathrm{V}^{-1}\,\mathrm{s}^{-1}$ under illumination.

Repeat	Thickness /Å	Material	Dopant/ note
1	100	GaAs	cap
1	400	Al(0.33)GaAs	Si - $9 \times 10^{17}\,\mathrm{cm}^{-3}$
1	400	Al(0.33)GaAs	
1	9100	GaAs (2DES at top)	
6	15000	GaAs	9 μm in total
1	300	AlAs	Etch stop
1	500	GaAs	
Semi-insulating GaAs substrate			

Table 3.3: Layer profile of modulation doped heterojunction, sample A3970.

A4182

A4182 is a repeat of A3970, again grown at Cambridge, but with a 15 μm etch stop. The characteristics were $\mu = 3.74 \times 10^6\,\mathrm{cm^2\,V^{-1}\,s^{-1}}$ with $n_s = 2.04 \times 10^{11}\,\mathrm{cm^{-2}}$ in the dark, and $\mu = 5.52 \times 10^6\,\mathrm{cm^2\,V^{-1}\,s^{-1}}$ with $n_s = 3.47 \times 10^{11}\,\mathrm{cm^{-2}}$ when illuminated.

Chapter 4

Measurements of induced currents in the QHE

4.1 Introduction

This chapter presents a study of induced eddy currents in the integer quantum Hall effect (IQHE), in a GaAs/(Al,Ga)As single layer heterojunction. The size of the induced current was measured using the contactless measurement of torque magnetometry at integer filling factors $\nu = 8, 6, 4, 3, 2$ and 1 in the temperature range 39 mK to 1.6 K. Induced current amplitudes for different sweep rates, known as sweep rate IV characteristics, were mapped for several filling factors over the range of temperatures 100 to 800 mK, and a non-linear sweep rate dependence was observed and is interpreted as breakdown of the IQHE near the edge of the 2DES. At fixed field positions decays of the induced currents were seen and are comparable with the longest lived persistent currents observed previously by Kershaw et al. [51]. The temperature dependence of the eddy currents is measured at 100 mK intervals up to 800 mK, and $\nu = 2$ is observed to insensitive to a change in temperature. Decay curves are generated from the sweep rate IV curves, and give a new explanation for the shape of the decay curves. A quantum point contact at the centre of the sample was activated in an attempt to affect the induced current, and to measure

the distribution of the eddy near the edge, but this is the subject of the following chapter.

4.2 Early measurements of induced currents

The IQHE was discovered by von Klitzing et al. [1] in 1980, and is characterised by quantised Hall plateaux in ρ_{xy} and 'zero's in the longitudinal resistivity ρ_{xx}. When the Fermi energy is between Landau levels, the current through an ideal device at 0 K flows without dissipation. This is not realised experimentally due to various scattering processes which will be discussed in this chapter. Early measurements of ρ_{xx} were limited by the resolution of the voltmeter used, Tsui and Gossard [52] reported an upper limit of $\rho_{xx} < 0.1\Omega$ shortly after the discovery of the IQHE. In 1982 an improvement was made by Tsui et al. using a Corbino geometry in a GaAs/(Al,Ga)As heterojunction system, which gave a new limit of $\rho_{xx} \lesssim 5 \times 10^{-7}\Omega/\square$.

In 1985 Eisenstein et al. [7] were the first to measure induced eddy currents around integer filling factors with a torsion balance magnetometer. Eddy currents are induced by an EMF proportional to the sweep rate of the magnet, so by measuring the induced current the authors were able to estimate the resistance of the sample. They assumed that the current flow was not in the bulk, but confined to a narrow region about the edge of $\sim 10\,\mu$m, which gave $\rho_{xx} \sim 10^{-6}\Omega/\square$ at ~ 0.5 K, for a 172 layer superlattice. The low mobility superlattice had both a linear, and a non-linear regime, in the induced current/ voltage characteristic. They made a comparison with a high mobility single-interface sample, which was entirely non-linear, and this was theorised to be a manifestation of breakdown of the QHE.

4.3 High current breakdown of the quantum Hall effect

4.3.1 Electron-heating model

Breakdown of the quantum Hall effect due to high currents has been studied extensively, and has been used to determine the current distribution in samples. Ebert et al. [54] first observed breakdown of the zero resistance state of ρ_{xx} in a transport measurement. They observed non-ohmic behaviour in the IV characteristic (see later, section 4.6), and a critical current density that varied with magnetic field around $\nu = 2$ as shown in figure 4.1. By assuming that the current flow was uniform throughout the sample, they showed that the nearly loss-less 'supercurrent' was abruptly destroyed above a critical value of $j_x \approx 0.56\,\mathrm{A\,m^{-1}}$. Additionally, at elevated temperatures the authors observed a 'pre-breakdown' effect; E_x increased in a step-like manner with increasing current density. The explanation offered was that the breakdown occurred due to an electron heating effect, with breakdown occurring at the point when the rate of energy being supplied to the lattice exceeded that rate of removal from the lattice.

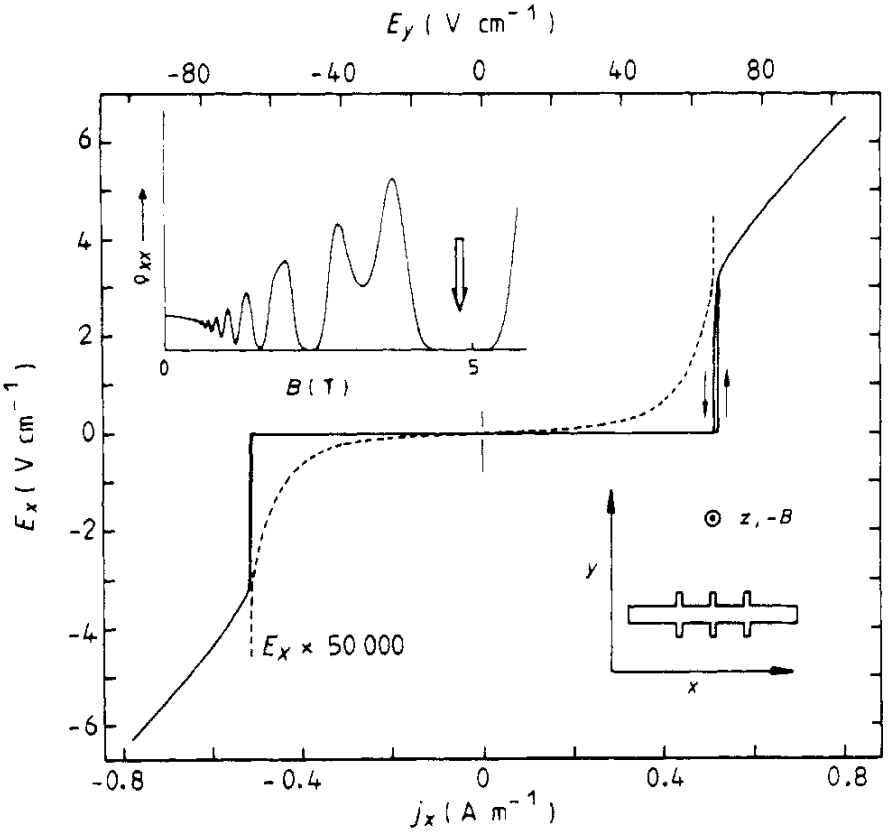

Figure 4.1: Current-voltage characteristic of a GaAs/(Al,Ga)As heterostructure at $T = 1.4\,\mathrm{K}$, from Ebert et al. [54]. The top inset indicates the magnetic field position at which the breakdown was measured, and the bottom inset shows the device geometry. The solid line in the central figure is magnified by a factor of 50 000 to give the broken curve.

Cage et al. [55] followed this work shortly after, and observed a similar breakdown to Ebert et al., but their experiment suggested that the breakdown was spatially inhomogeneous and they concluded that the so called 'pre-breakdown' observed by Ebert et al. was a sequence of breakdown events, each occurring at a different position in the sample.

Komiyama et al. [56] expanded upon this work by performing experiments in extended ranges of the electric Hall field up to 100 V/cm and a range of lattice temperatures from 2 to 50 K. The authors derived an energy balance equation that allowed electron temperature as a function of lattice temperature and electric field to be calculated. They demonstrated that as the electric field approached a critical value there was a sharp rise in electron temperature. They predicted an S-shaped

characteristic for the longitudinal conductivity σ_{xx} against Hall electric field, predicting three possible electron temperatures for a given lattice temperature. The middle temperature was shown to be unstable, hence never realised experimentally, and the 2DES thus comprised regions of either a high or low electron temperature. The predictions fitted the experimental data and estimated a critical Hall field of 50 V/cm.

4.3.2 Intra-Landau-level scattering

This model was proposed by Streda and von Klitzing [57] and predicts that the quantum Hall effect breaks down when the drift velocity of the 2DES is close to the value of the speed of sound in the material, beyond which emission of acoustic phonons becomes possible. This is an analogy to Cerenkov radiation, in which charged particles moving through a medium at speeds greater than the speed of light in that material, emit photons. The model predicts scattering of electrons from one sample edge to the other via an interaction with the phonon system, but requires the presence of empty states in the upper-most Landau level just below the Fermi energy. For measurements made at exact filling factor in samples of low disorder, at low temperature, this scattering process is unlikely. For samples under investigation in this chapter, where the sample edges are far from a thin Hall geometry, this process is less likely to explain the effects seen than other models.

4.3.3 Inter-Landau-level scattering

Heinonen et al. [58] suggested a phonon assisted inter-Landau-level transition, where an electron is excited into a higher Landau level that is previously unoccupied. The prediction made was that onset of breakdown happens at a critical Hall field, E_c, across the sample after which there is a dramatic onset of dissipation. The form of the longitudinal voltage drop as a function of current density was found to be in agreement with experiments, but the critical currents calculated were approximately

a factor of 20 larger than observations, with a critical current density of $\sim 5.5\,\mathrm{A\,m^{-1}}$ for $\nu = 1$ occurring at a field of 5.5 T.

Eaves and Sheard [59] later proposed the quasi-elastic inter-Landau-level scattering model (QUILLS) to explain features in the experimental observations by Bliek et al. [60]. The experiment used Hall bars with narrow constrictions in the middle, of widths $1.0\,\mu$m and $66\,\mu$m, giving a conducting channel that was sufficiently small to be considered homogeneous. Critical current densities as high as $32\,\mathrm{A\,m^{-1}}$ were measured, much larger than previous wide sample experiments and theory, which thus far only assumed a uniform current. Eaves and Sheard showed that considering the solution of the one-electron Schrödinger equation in crossed electric and magnetic fields gave a useful insight in the observations, and using this, calculated the critical field for which breakdown occurs. When there is significant overlap of the wavefunctions, as depicted in figure 4.2, between the highest filled Landau level and the next upper-most,

$$E_c = \frac{\hbar\omega_c}{el_B\left[(2n+1)^{1/2} + (2n+3)^{1/2}\right]},$$

and

$$J_c = \frac{E_c}{(h/\nu e^2)}.$$

where $n = 0$ for $\nu = 1, 2$ and $n = 1$ for $\nu = 3, 4$ etc. The authors calculated for $\nu = 2, 4$ $(n = 0, 1)$ a critical current of $29\,\mathrm{A\,m^{-1}}$ and $14\,\mathrm{A\,m^{-1}}$. This agreed to within 10% with the threshold current densities reported by Bliek et al. [60].

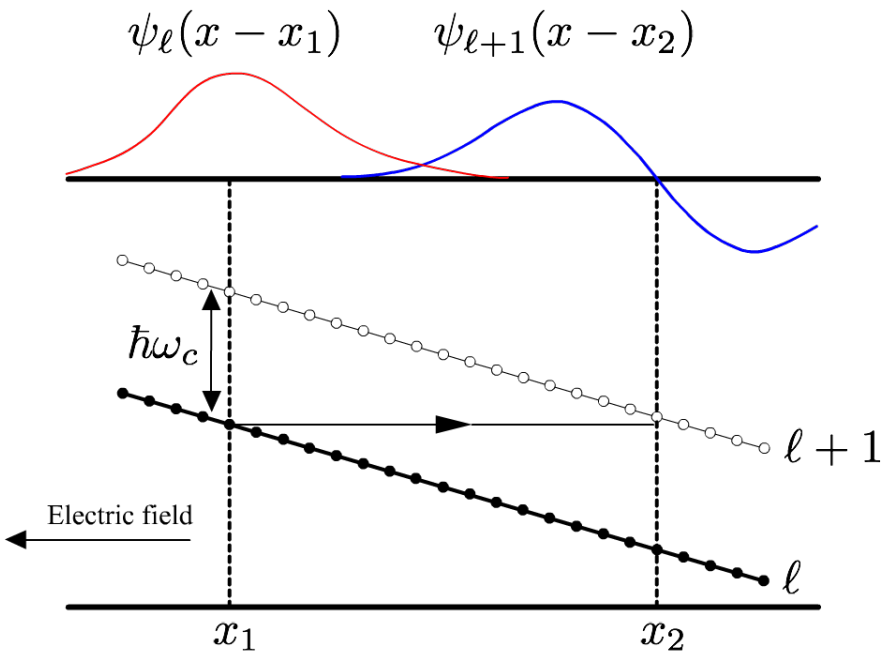

Figure 4.2: Quasi-elastic inter-Landau-level scattering representation, after Eaves and Sheard [59] Landau levels are sloped ($slope = eE$) due to an electric field. States in the lower LL (ℓ) acquire the same energy as the upper LL ($\ell+1$) and can tunnel to these new states if perturbed.

4.4 Experiment

The sample, AK47, is a single layer GaAs/(Al,Ga)As quantum well structure with a measured mobility of $1.03 \times 10^6\,\mathrm{cm^2\,V^{-1}\,s^{-1}}$, grown at the Institute for Microstructural Sciences (within the group of Sachrajda), Canada and processed by Dr Alicia Kam. The sample was mounted onto a stycast [42] rotor at an angle 20° to the applied magnetic field, and investigated through torque magnetometry as described in chapter 3. The 2DES under investigation had a metallic split gate defined on the surface, $\sim 100\,\mathrm{nm}$ away from the electron system. The gate was activated through the application of a negative bias voltage and the system became a quantum point contact, the one large 2DES was transformed into two 2DES regions connected via a tunable constriction. The dual magnetometry and quantum point contact experiments are the subject of chapter 5, and although there are ohmic contacts on the 2DES, they are not required for the contactless study presented in this chapter.

The addition of ohmic contacts does however allow the measurement of the number density of the system through the oscillations in ρ_{xx} on the same cool down, n_s was measured to be $2.01 \times 10^{11}\,\mathrm{cm}^{-2}$. The dimensions of the 2DES on the GaAs substrate are $4.0\,\mathrm{mm} \times 4.5\,\mathrm{mm}$. We observed no difference in the size of the induced magnetic moment for the sample whether it was one 2DES or split in two by the gate, this is in itself an interesting result and will be discussed more in chapter 4. It is important to note that the gate was active for the experiments presented in this chapter, set to a value where the only conduction mechanism was via quantum tunneling. No interaction effects between eddy currents in adjacent areas was seen, so the gate had no other effect other than cutting the 2DES in two. The magnetometer was calibrated at low temperature to give a responsivity of $3.00 \times 10^{-6}\,\mathrm{N\,m\,V}^{-1}$ as discussed in Chapter 3.

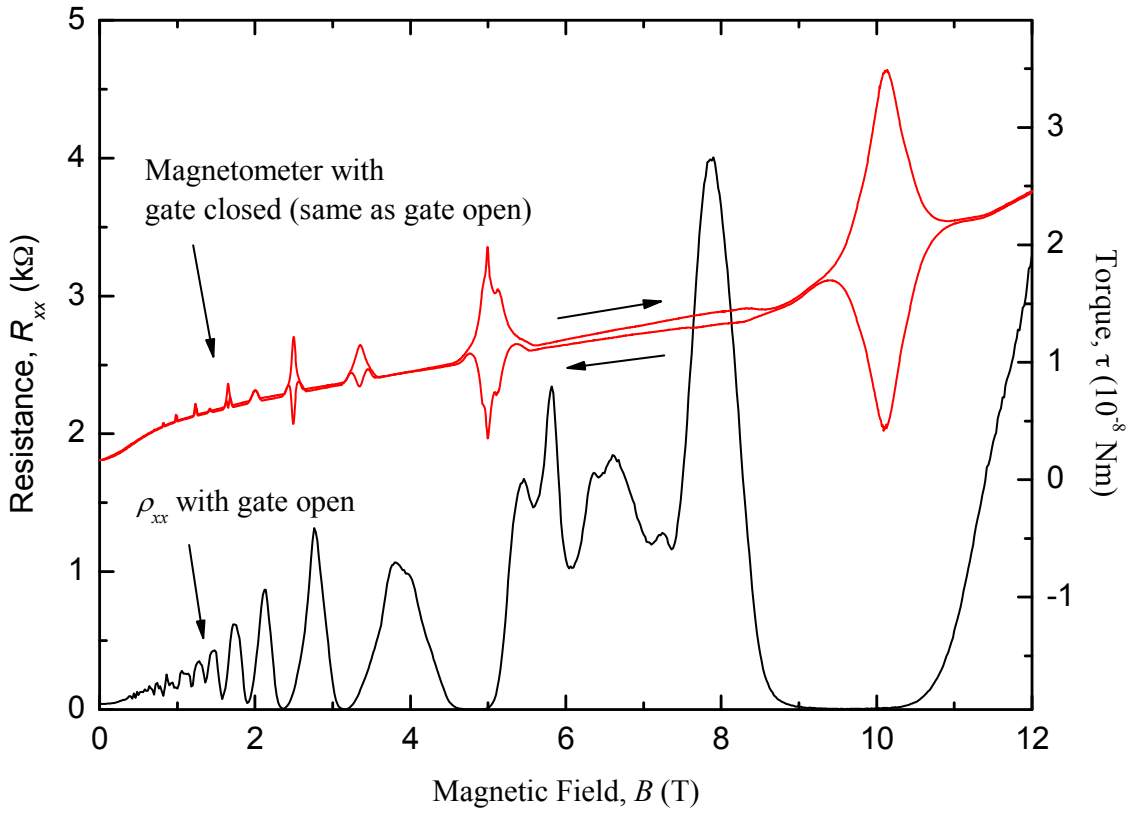

Figure 4.3: Measurement of magnetisation through torque magnetometry and longitudinal resistivity ρ_{xx} through a transport measurement. The resistivity ρ_{xx} is characterised by deep resistance minimum at integer filling factors. Both experiments were conducted at 40 mK but are not simultaneous.

Figure 4.3 illustrates the low temperature, high magnetic field measurement of ρ_{xx} with deep resistance minima periodic in $1/B$. The induced eddy currents, which do not carry a net current from source to drain, were detectable through torque magnetometry and are depicted on the same plot, but had no detectable effect on the transport measurement. In high mobility samples, where the zero resistance state becomes harder to measure with a conventional electrical measurement, the magnetisation due to the induced eddy currents becomes larger and hence easier to measure. Eddy currents are hysteretic in nature; they store energy in response to a changing magnetic field. In this case the induced currents are not centred in the middle of the ρ_{xx} minima as one might expect, this is due to the number density varying slightly over the course of the experiment.

The features of interest are the reversible eddy currents at integer filling factors, but there were some less pronounced non-reversing features apparent in the magnetometry trace. At integer filling factors the hysteretic induced currents were present for $\nu = 1, 2, 3, 4, 6$ and 8. The baseline is not flat, there is a background signal which was likely due to the diamagnetic moments of atoms in the substrate, gold contact pads (not used in this experiment), contact wires and possibly magnetic impurities in the rotor and fibre. The GaAs dummy sample on the the other side of the rotor acted to minimise this background. Another contribution to the background is the magnet; it changes shape somewhat as the current is increased causing the magnetic field centre to move, resulting in a field gradient at the sample. The backgrounds have been investigated in more detail by Gething [61], and are of little further interest in this investigation.

Another feature worth noting is the small non-reversing component in the eddy current trace around integer filling factor as seen in figure 4.4, present in both lock-in channels. The experiment was set up so that the lock-in amplifier was phased up, i.e. the x-phase component (signal component that is in phase with excitation) corresponded to a capacitive change in the bridge, a mechanical deflection. It was observed that the $y-$phase (90^ophase shift from excitation) is zero except for at integer filling factors, and corresponds to a non-mechanical change in the balance of

the bridge circuit. If the features were de-Haas—van-Alphen oscillations they would have a sawtooth appearance and should only manifest as a mechanical deflection, seen in the $x-$phase component of the signal. The features can be seen in more detail in figure 4.5, and it is more obvious that there is a non-reversing component in the $x-$phase that reflects the $y-$phase, plus a reversing eddy current. One explanation is that the 2DES was capacitively coupling to the rotor and/or the stator plates. Additionally in this experiment, there were wires connected to the 2DES which may have also contributed. Although unintentional in this case, capacitive coupling to the conducting 2DES has been used by Takaoka et al. [62] and Petersen and O.P [63] for example, by measuring the differential capacitance formed between a 2DES and a Schottky gate as a function of magnetic field. They measured a minima of the capacitance when the Fermi level E_{F} was between Landau levels, and found their results could not be explained by existing interpretation of magnetoresistance, and suggested that the bottom values are determined by the edge current carrying area.

Morris [64] observed the same phenomena in a torque magnetometry experiment using a similar experimental arrangement to the one in this chapter. Using the Oto model as outlined in [65, 62], that proposes the differential capacitance consists of two components, a contribution from the edge channels, and a component from the bulk of the sample. The model used by Morris predicted a real and imaginary component, including the double peak structure in the imaginary component of the capacitively coupled signal. It would be difficult to model the coupling in this experiment, due to the extra complication of wires. Because the eddy current reverses direction, the additional capacitive coupling component can be easily deducted.

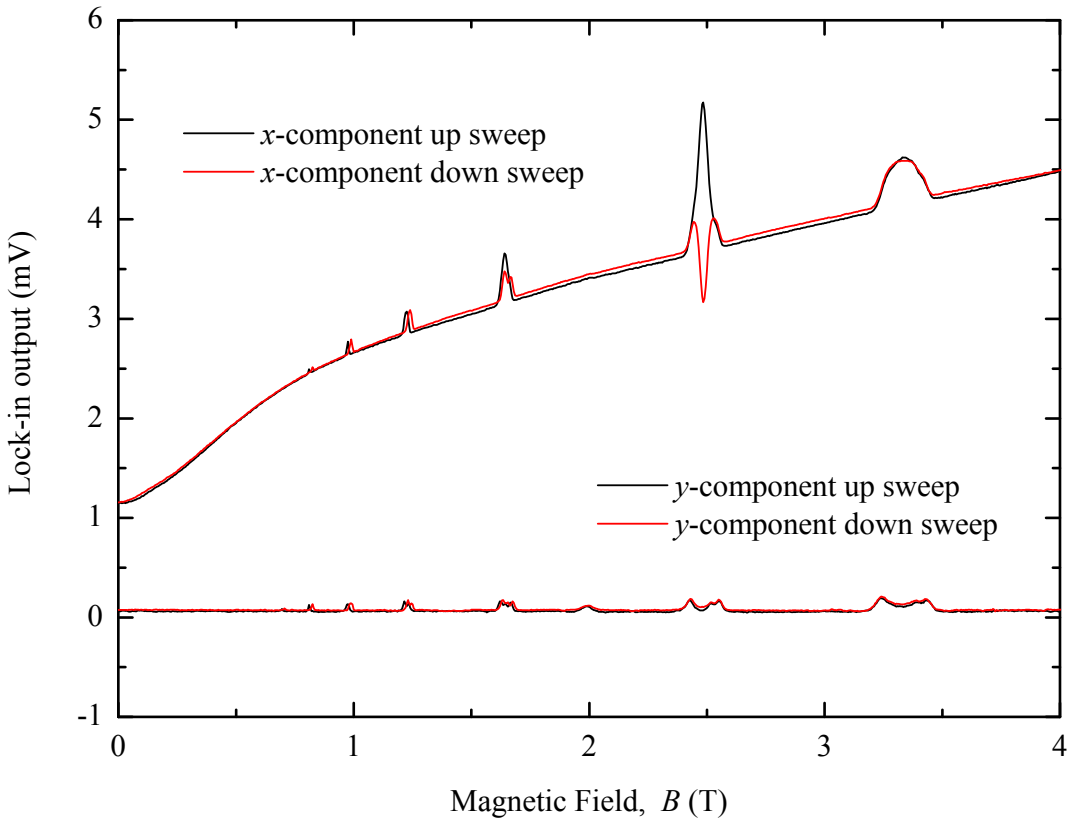

Figure 4.4: $x-$ and $y-$phase components of a lock-in amplifier for a typical magnetometry run at a sweep rate of $1.605\,\mathrm{mT\,s^{-1}}$ at 300 mK.

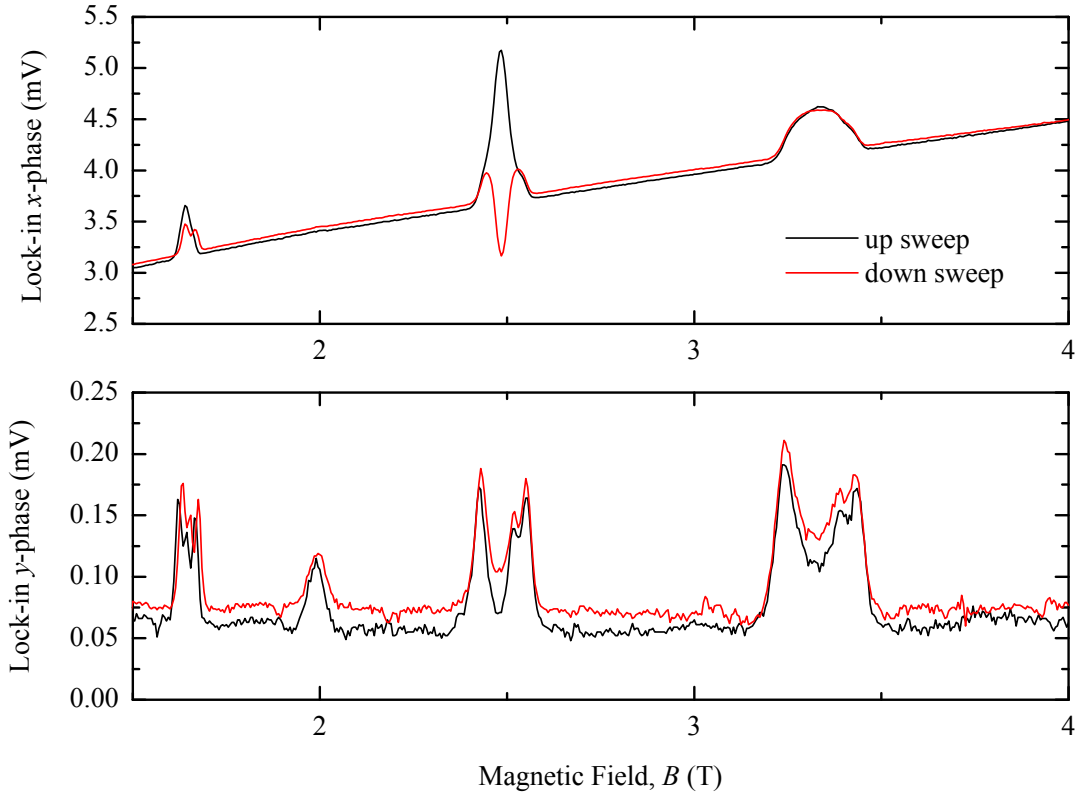

Figure 4.5: $x-$ and $y-$phase components taken from figure 4.4 and magnified. Features in the $y-$phase are small compared to the $x-$phase, and likely to have arisen from capacitive coupling to the 2DES, oscillations are seen with the Fermi energy is between Landau levels. The double peak structure in the $y-$phase is predicted by Morris [64].

4.5 Temperature Dependence

Rigal et al. [66] investigated the breakdown of the dissipationless conductance in the quantum Hall regime over a range of filling factors in a transport experiment. The single quantum well Hall bars were patterned to a width of $250\,\mu$m, with $750\,\mu$m between voltage probes, and mobilities of the samples varied from $3 - 22\,\mathrm{m^2V^{-1}s^{-1}}$ with carrier densities of $(6 - 14) \times 10^{11}\,\mathrm{cm^{-2}}$. They constructed a phase diagram, (figure 4.6), and noted that the temperature dependence had a striking resemblance to the critical field in a superconductor. Whilst such an experiment for two chosen current contacts has the advantage that the critical current is well defined, it has the

drawback that the large currents involved can lead to heating in the current contacts. Some of the contacts were observed to show a very abrupt increase in voltage upon breakdown which the authors attributed to an avalanche heating process. Although the investigation drew a comparison to superconductivity, there was no theoretical basis to link superconductivity to the IQHE.

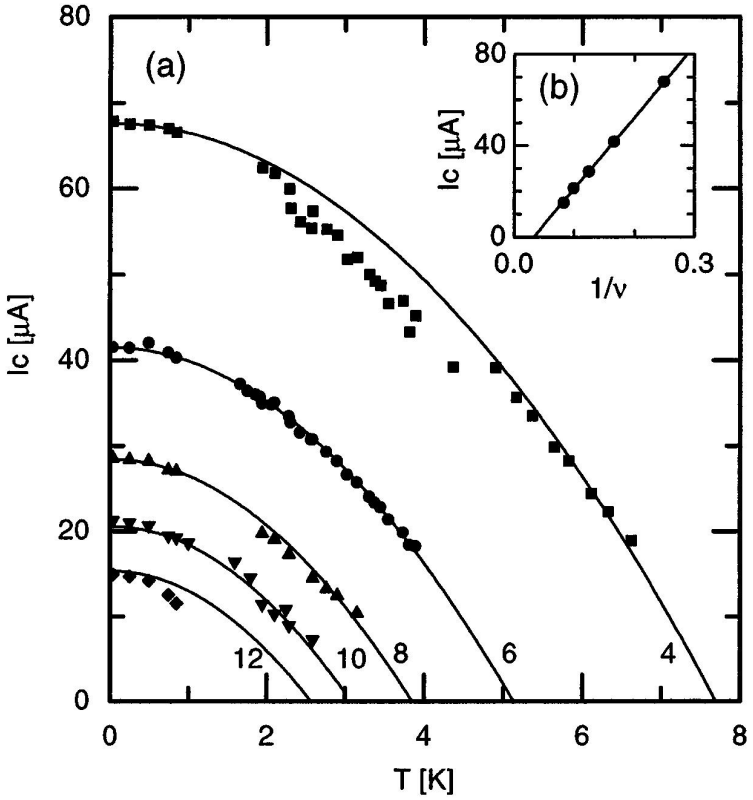

Figure 4.6: Phase diagram of the breakdown current in the QHE with temperature after Rigal et al. [66]

Matthews et al. [67] investigated the temperature dependence of the breakdown of the QHE through the contactless measurement of magnetisation, which will be built upon in this chapter. They found that for strongly disordered samples two distinct breakdown regimes exist. Above a certain temperature T_c, the critical magnetic moment (proportional to the critical current) decreased linearly, and below T_c the magnetic moment of the induced current saturated. They attributed this effect to the QUILLS model.

The temperature dependence of the breakdown of the quantum Hall effect was measured over the temperature range 100 mK to 1600 mK, and in this section a com-

parison is made to existing results and models. The sweep rate was kept constant at $3.2\,\mathrm{mT\,s^{-1}}$ over the magnetic field range $0 - 12\,\mathrm{T}$, and in general the peak to peak eddy current amplitude reduced as temperature was elevated. The sweep rate was chosen to correspond to a current in the breakdown regime, induced current IV characteristics will be discussed in more detail in the next section.

Eddy currents were present for $\nu = 1, 2, 3, 4, 6$, and 8. The measured torque with varying magnetic field is shown in figure 4.7 for $\nu = 1, 2, 3, 4$ and 6. Filling factor $\nu = 8$ disappeared very fast with temperature, as not only was the magnetic moment smaller, but the value of measurement field B was smaller therefore a smaller torque made it a more difficult to resolve from the noise. At low temperature where it is arguable that the eddy currents saturated for the filling factors $\nu = 1, 2$ and 4 at different torques, when the different measurement fields are considered, they correspond to very similar saturation currents in this sample. There is not an obvious physical reason why this should be, and is not the case for other samples such as those of Jones et al. [68].

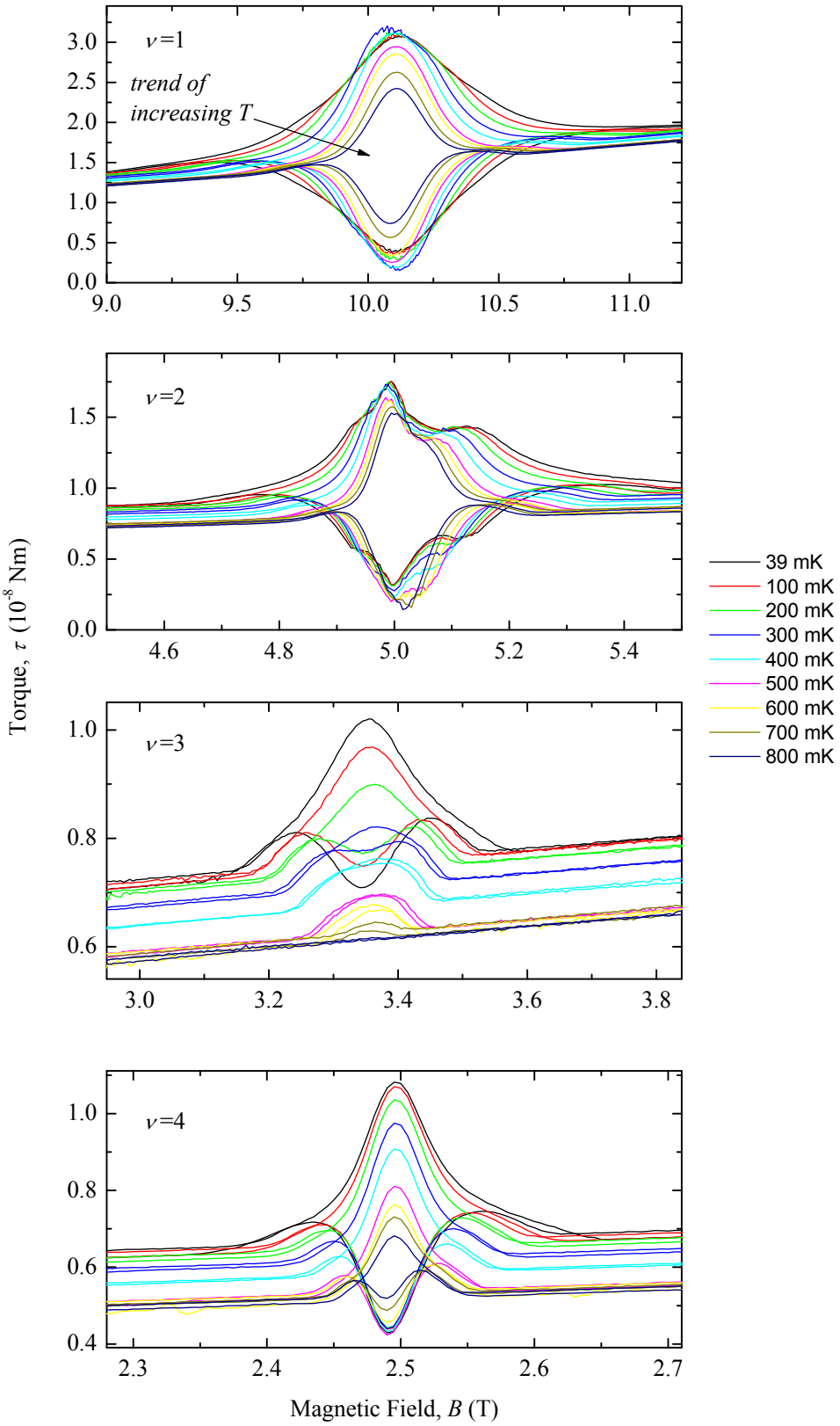

Figure 4.7: Induced eddy currents at $\nu = 1, 2, 3, 4$ changed shape and amplitude with temperature. As temperature increases the integral of the total current decreased, but for $\nu = 2$ the amplitude is approximately constant.

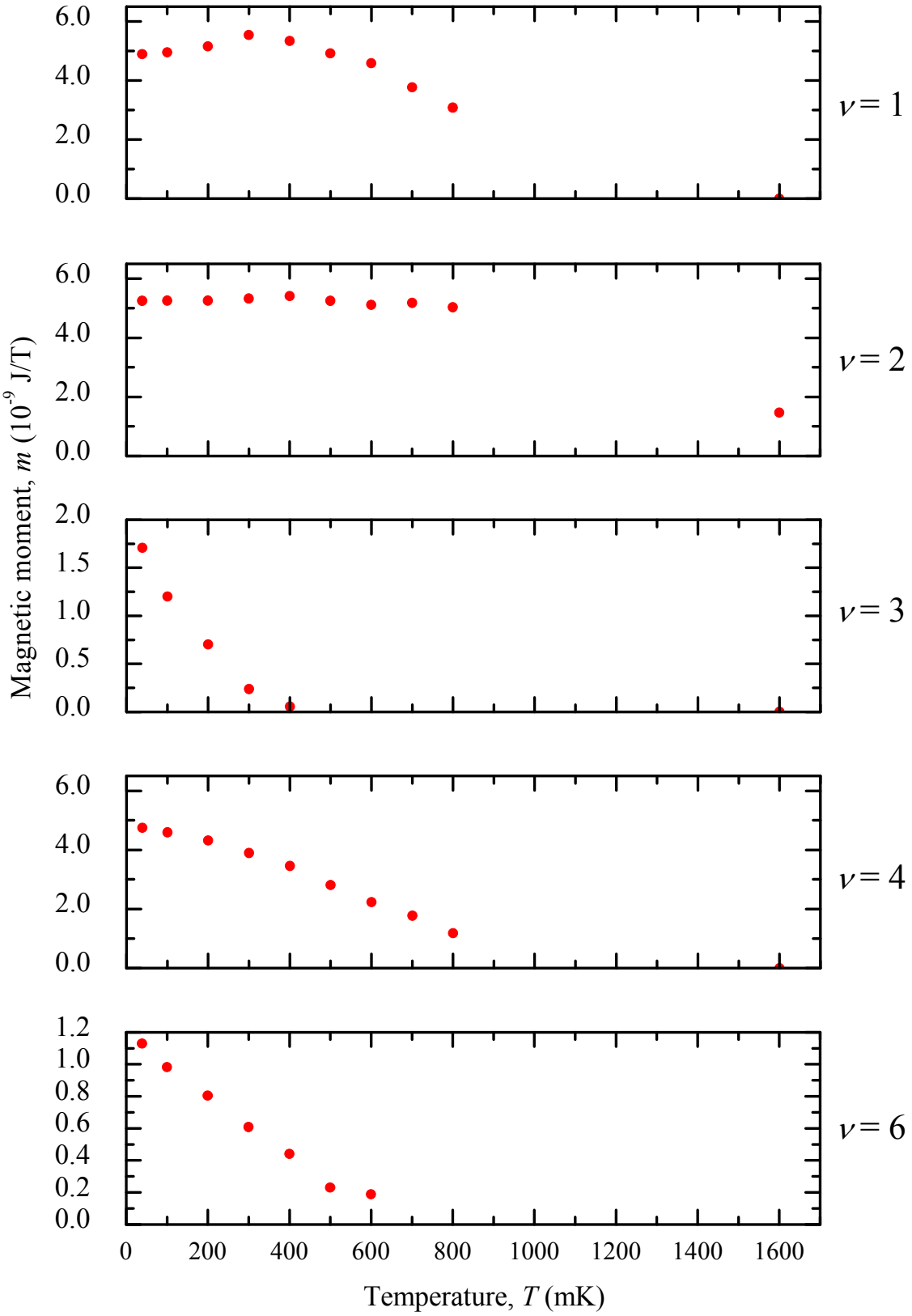

Figure 4.8: Eddy current amplitude vs temperature converted from figure 4.7. Additionally data from a high T sweep at 1.6 K is included, the only remnant eddy current was $\nu = 2$. $\nu = 1, 2$ and perhaps 4, saturate at low T due to a breakdown effect, the strongest candidate is electron heating.

From the shapes in figure 4.7 a plot can be produced of peak amplitude against temperature, shown in figure 4.8. Odd filling factors have a stronger temperature dependence than their even filling factor counterparts for the same Landau level index, i.e. $\nu = 2$ has a less dramatic T dependence than $\nu = 1$, and $\nu = 4$ is also more robust than $\nu = 3$. This is because at even ν the Fermi level is between Landau states of different n, whereas at odd ν, it resides between the spin levels of a given Landau level. The spin splitting in GaAs is much smaller than the cyclotron splitting $\hbar\omega_c$, therefore the quantum Hall effect is better observed for even values of ν. Filling factor $\nu = 2$ was expected to have the deepest resistance minimum, so it is somewhat surprising that the different filling factors have the same saturation current. One explanation is that the saturation regime was self-limiting due to heating of the 2DES from the induced current dissipating. Because the QHE was in breakdown for a given sweep rate, then it did not matter what the starting point in ρ_{xx} is, because the eddy current is driven by a constant voltage, not a constant current, so ρ_{xx} and the temperature will both rise and self limit at the point where is it in thermal equilibrium. Taking $\nu = 1$ as an example, in the low T regime the current may have been limited by heating due to the eddy current, and beyond the shoulder at a temperature of $\sim 300\,\mathrm{mK}$, the 2DES is then limited by the temperature of the GaAs, and decreased with temperature above this point.

Filling factor $\nu = 1$ did not simply saturate at low temperature, but had a smaller peak amplitude at base temperature than at 300 mK. The shapes of the eddy currents in figure 4.7 show that there is still an effect present, the eddy current looks like it was being 'squeezed-in', so occurred over a wider field range at lowest temperatures. At lower temperatures, the zero resistance state was wider and the current is induced at a lower value of B, it effectively heated the sample and increased ρ_{xx} before getting to the centre of the zero resistance state.

For filling factor $\nu = 2$, the peak current against temperature in figure 4.7 was robust (i.e. the peak amplitude did not decrease with temperature until 1.6 K), more so than previously reported in any published magnetometry experiment, although more points between 800 mK and 1600 mK are required to estimate the saturation

temperature. This suggests that the eddy current was raising the temperature of the 2DES for $\nu = 2$ up to at least 800 mK. It is interesting to note that conventional transport experiments do not saturate at high temperatures, and although the eddy currents are not detected they must still be present, so this suggests a complete decoupling of induced eddy currents from conventional currents. In figure (4.8), the data has been converted to a magnetic moment so amplitudes at different filling factors can be compared. The magnetic moment, which is proportional to the critical current, saturated at approximately the same value for $\nu = 1, 2$ and 4. As the sweep rate was fixed, the voltage driving the current was fixed, therefore the power dissipated being dissipated $P = IV$, would correspond to an identical critical current for each filling factor (assuming the minima in the magnetothermal oscillations to be approximately equal for each filling factor). The saturation currents being the same for different filling factors is strong evidence for an electron heating effect.

Matthews et al. [67] developed a model describing the induced currents. Their charge relocation description of the breakdown of the quantum Hall effect explains the sweep rate and temperature dependence's of eddy current amplitudes observed by the previous studies of the same authors and others. Jones et al. [68] observed that the $\nu = 4$ current became progressively smaller as temperature was increased, as expected for a quantum Hall type structure. They also observed the oddity that the $\nu = 2$ current saturated and argued it was further evidence that breakdown is being observed, but did not attribute it to heating: at low temperatures ρ_{xx} is small and therefore the current density exceeds j_c; breakdown occurs, increasing ρ_{xx} and effectively regulating the current so that it is unaffected by any further temperature reduction.

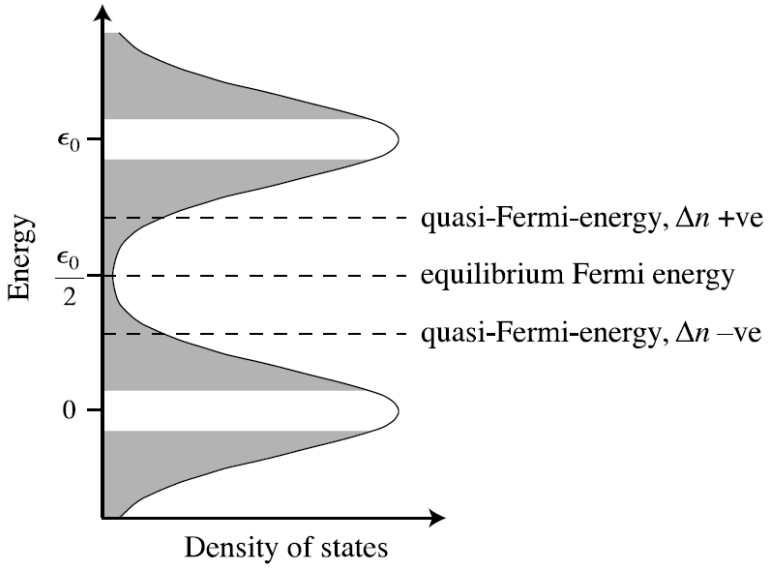

Figure 4.9: Disorder broadened LLs, showing the position of the Fermi energy at integer ν. When a magnetic field is swept, electrons accumulate in, or deplete from, different regions within the 2DES, resulting in regions with quasi-Fermi energies. After Usher and Elliott [69].

The charge redistribution model of Kavokin et al. [70] was invoked to explain the temperature dependences of the induced currents in both high and low mobility experiments of Matthews et al. [67] based on the arguments of Dyakonov [71]. It was assumed that in a two-dimensional system, charges would not accumulate solely at the edges of the sample, but be distributed over the entire area. Regions with an extra electron density Δn raise the local quasi-Fermi energy above its equilibrium position halfway between Landau levels, as depicted in figure 4.9. In this region the probability of thermal activation of electrons from the highest full LL to the lowest empty one is increased. In regions of electron depletion by Δn, the probability of thermal excitation of holes is increased. The authors calculated the saturation value of the magnetic moment, m_s,

$$m_\mathrm{s} = \Lambda \pi \sigma_{xy} e \Delta n_\mathrm{c}(T) R^3, \tag{4.1}$$

where Λ is a dimensionless constant, ~ 1.1, and R is the radius of the sample. The exact distribution does not matter, but Δn_c has a temperature dependence that depends on the form of the DOS in the localised region between the highest

occupied LL and the lowest unoccupied. For a high mobility 2DES, $\rho(\epsilon)$ will be very sharp at this point, but will exponentially become larger as the level moves away from $\epsilon_0/2$ (assuming the LLs to be Gaussian in shape). It was predicted for high mobility samples the temperature dependence would therefore be linear. In lower mobility samples, the DOS is larger around $\epsilon_0/2$, and possibly a background density of states. Because of the large DOS, a larger charge build up is required to shift the quasi-Fermi energy to its critical value of $m_{\rm s}$.

This same explanation can be used to explain the shapes seen in the temperature dependences in this chapter for the different filling factors. For $\nu = 1$ and $\nu = 4$, the temperature dependences out of the saturation regime are approximately linear, in agreement with the model. For filling factors $\nu = 3$ and $\nu = 6$, the temperature dependences start to curve at higher T. The odd integer filling factors, as previously mentioned are spin split, so levels are closer together than for even integer filling factors. The DOS between levels therefore means the onset on the steep region requires a smaller $\Delta n_{\rm c}$, so the temperature dependence has the appearance of a higher mobility exponential form.

4.6 Sweep rate IV curves

By relating the magnetic moment to the current induced in the sample, and the sweep rate to an EMF, a current versus voltage characteristic for the eddy currents can be constructed. The flux through the sample is proportional to the area A orientated at an angle θ to the magnetic field B , $\Phi_B = BA\cos\theta$. From Faraday's law of induction flux, can be related to an EMF,

$$\varepsilon = -\frac{d\Phi_B}{dt} = A\cos\theta\frac{dB}{dt}. \tag{4.2}$$

The magnetic moment m of a loop carrying a current I is given by

$$m = IA, \tag{4.3}$$

assuming the current density is concentrated at the perimeter of the sample. By varying the sweep rate and measuring the magnetic moment an IV characteristic for the induced currents is thus produced. An up and a down sweep was measured, and the current was therefore proportional to half the peak to peak amplitude.

Eddy current sweep rate dependences were measured over a range of temperatures from 100 mK to 800 mK for filling factors $\nu = 1, 2, 4$ and 6 as seen in figure 4.10. The current induced at $\nu = 2$ was the most robust and was still present at 1.6 K. Torques can be converted to a magnetic moment from $\tau = mB\cos\theta$, and then to a current assuming the majority is distributed to the edge of the sample of area $A = 1.8 \times 10^{-5}\,\mathrm{m}^2$. $\nu = 1, 2$ and 4 all saturated at an almost identical critical value corresponding to a current of $\sim 0.29\,\mathrm{mA}$.

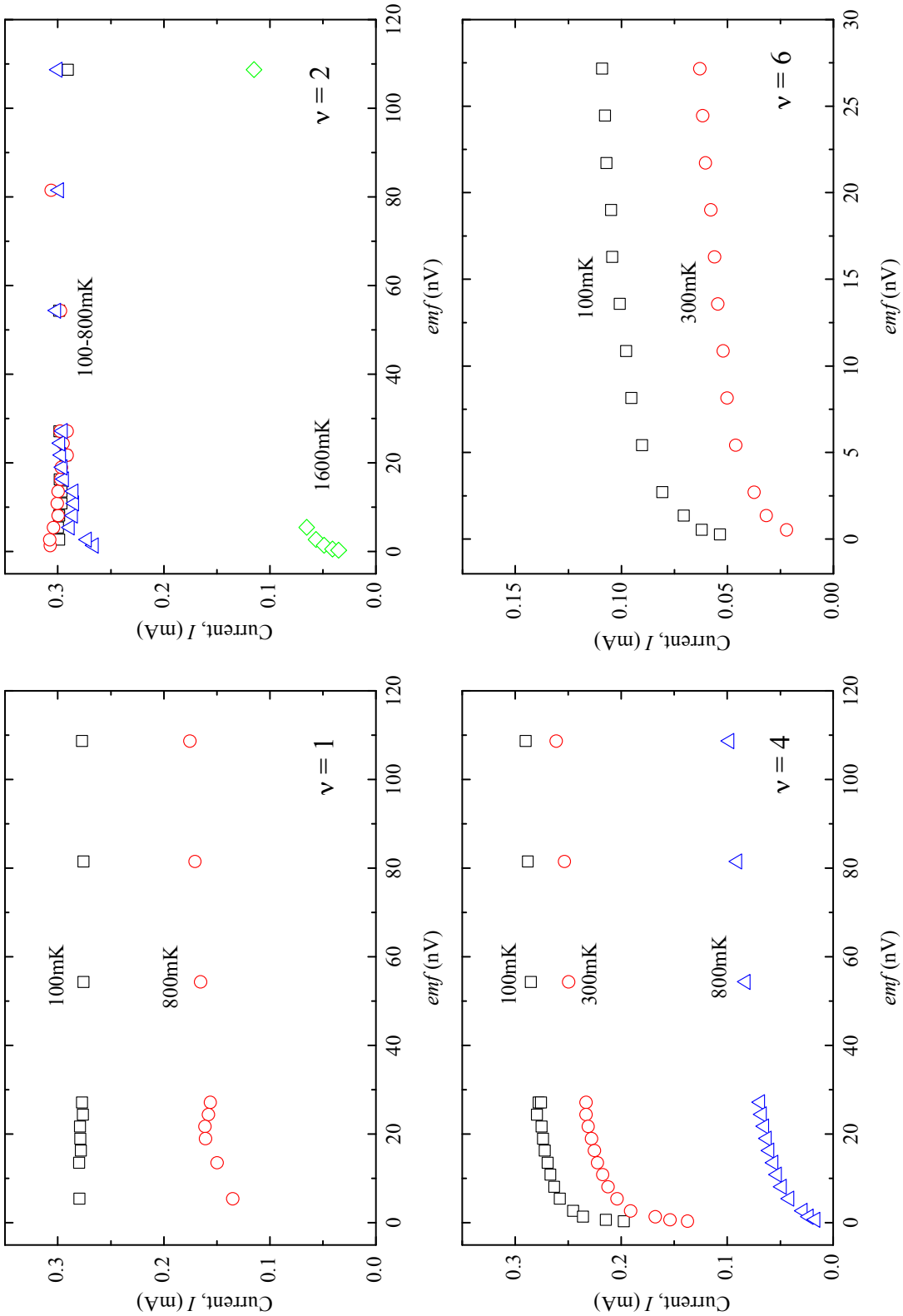

Figure 4.10: Sweep rate IV curves for $\nu = 1, 2, 4$ and 6 at various temperatures are non-linear. Sweep rates have been converted to an EMF and magnetic moments to a current. At higher EMFs the breakdown of the QHE is evident, the current does not exceed a maximum value.

These breakdown measurements are unlike breakdown measurements in conventional transport experiments on Hall bars; in a Hall bar measurement the current would be constant, and in this experiment it was the EMF that was fixed. The power dissipated into the sample causing breakdown was self regulating, as it is equal to V^2/R, as R itself has a temperature dependence. Other experiments observe a thermal runaway in the breakdown of the QHE, which was not expected, and not seen in these experiments.

The lowest EMFs experimentally achievable correspond to sweep rates of $21.3\,\mu\mathrm{T\,s^{-1}}$ for $\nu = 4$ and 6, as at lower sweep rates than this the field would have ceased to sweep smoothly because the power supply changes the field in discrete steps of $2.4\,\mu\mathrm{T}$. For $\nu = 1$ and 2 sweep rates were limited to experiments lasting no longer than 12 hours each way over the given field range (as the current exists over a larger field range for these filling factors), as the fridge was run in single shot mode to keep mechanical noise to a minimum. Even for the lowest EMFs the IV curves never entered a linear regime.

It is possible to estimate the critical current density j_c from the critical currents measured in figure 4.10. As a lower limit let us assume that the current flows throughout the bulk during QHE breakdown, then

$$j_c = \frac{I_c}{R_{eff}}, \tag{4.4}$$

where R_{eff} is the effective radius of a circular sample of the same total area as AK47 (for the purpose of these estimates we assume the critical current to be the same for $\nu = 1, 2$ and 4 as they are very close). This gives a current density of $0.12\,\mathrm{A\,m^{-1}}$, comparable to the early measurements of Ebert et al. [54] where they measured $j_c \approx 0.56\,\mathrm{A\,m^{-1}}$. However this estimate has been shown to be a poor approximation of the real situation by later experiments, as discussed previously.

The other extreme is to assume the current flows entirely within a magnetic length

of the edge,

$$j_c = \frac{I_c}{(\hbar/eB)^{1/2}}. \tag{4.5}$$

The results can be seen in table 4.1. These estimates are rather large, several orders of magnitude larger than any transport measurement has yielded. A better estimate perhaps comes from something in between the two extremes. MacDonald et al. [72] proposed a current distribution model that was later modified by Balaban et al. [73] to deal with the divergence at the edge of the sample.

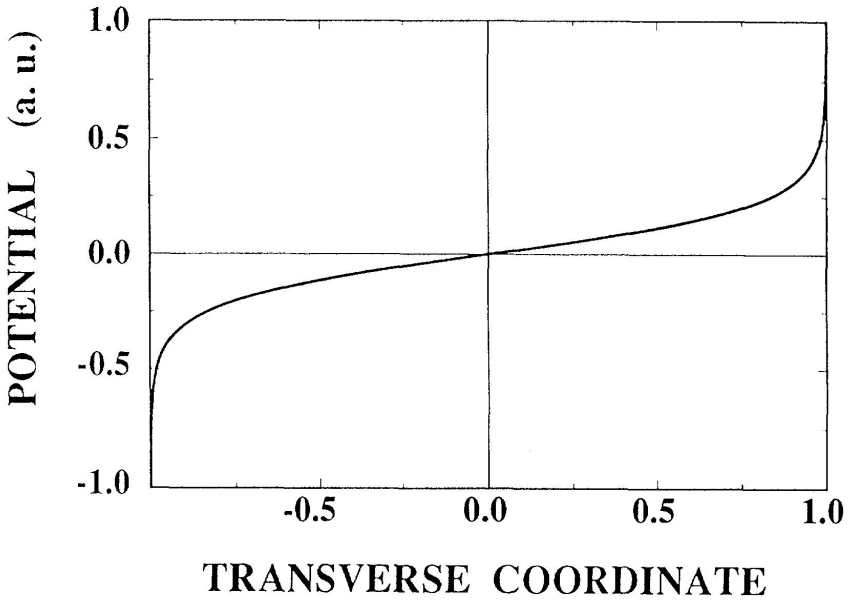

Figure 4.11: Calculated potential profile across a 20 μm Hall bar, as in equation (4.6) after Balaban et al. [73].

The model predicts that the potential across the sample varies as

$$V(x) = V_0 \ln \left(\frac{W}{W_0}\right)^{-1} \ln \left|\frac{x + W/2}{x - W/2}\right|, \tag{4.6}$$

where x is the position, W is the sample width and W_0 is a ν dependent length of the order of 10 nm, and

$$V_0 = \frac{I R_{\mathrm{H}}}{2}. \tag{4.7}$$

From this relation the authors showed the relationship between the critical current

I_c and critical Hall field E_c to be,

$$E_c = \frac{R_{\mathrm{H}}}{2(n+1)^{1/2} l_0} \ln\left(\frac{W}{W_0}\right)^{-1} I_c, \tag{4.8}$$

where R_{H} is the Hall resistance, l_0 is the magnetic length and n is the Landau level index (n=1 for $\nu = 1, 2$ and $n = 2$ for $\nu = 3, 4$). This gives radial Hall fields of $\sim 2.5 \times 10^6$ to $2.1 \times 10^7\,\mathrm{V\,m^{-1}}$, which is about an order of magnitude larger than predictions of the inter-Landau level tunneling model, but closer than assuming an entirely edge weighted distribution. For comparison to the other predictions E_c can be converted to a critical current j_c from

$$j_c = \frac{E_c}{R_{\mathrm{H}}}. \tag{4.9}$$

Results are tabulated again in table 4.1. Jones et al. [74] followed this same model and from sweep rate characteristics established a critical Hall field of $E_c = 3.7 \times 10^5\,\mathrm{V\,m^{-1}}$ for $\nu = 4$ and $E_c = 3.1 \times 10^6\,\mathrm{V\,m^{-1}}$ for $\nu = 2$. The authors reported a measured mobility of $27\,\mathrm{m^2\,V^{-1}s^{-1}}$ compared with the much higher mobility of AK47 of $103\,\mathrm{m^2\,V^{-1}s^{-1}}$. Additionally, the calibration for their magnetometer may have varied upon cool down, whereas in this experiment the magnetometer is calibrated in situ at refrigerator base temperature. Furthermore the authors Balaban et al. [73] do not know how breakdown currents of $\gtrsim 100\,\mu A$ can be accounted for in the framework of their model, which is certainly the case in this experiment, but it gives a rough estimate that is in the same order of magnitude as the most recent work.

Filling factor	J_c uniform	J_c within l_0	J_c non-uniform bulk
$\nu = 1$	$0.12\,\mathrm{A\,m^{-1}}$	$35.7\,\mathrm{kA\,m^{-1}}$	$2.6\,\mathrm{kA\,m^{-1}}$
$\nu = 2$	$0.12\,\mathrm{A\,m^{-1}}$	$25.2\,\mathrm{kA\,m^{-1}}$	$1.8\,\mathrm{kA\,m^{-1}}$
$\nu = 4$	$0.12\,\mathrm{A\,m^{-1}}$	$17.9\,\mathrm{kA\,m^{-1}}$	$1.2\,\mathrm{kA\,m^{-1}}$

Table 4.1: Critical current densities calculated for different assumptions in the current distribution.

4.7 Decay measurements

4.7.1 Brief Introduction

In the extreme limit of zero temperature, the longitudinal resistivity ρ_{xx} becomes zero between Landau levels. If the magnetic field B is increased at a constant sweep rate dB/dt, up to a value corresponding to an integer filling factor then stopped, a current is induced in the dissipationless state and will persist indefinitely. In a real disordered system, where temperature is finite, the decay of these induced eddy currents at fixed field can give an insight into the breakdown of the QHE, and into the relaxation processes by which the system returns to equilibrium. In previous experiments by Jones et al. [74] two distinct regimes were present: a fast initial decay of $\tau \sim$ minutes and a much longer decay of hours for $\nu = 1$ and 2, in samples of mobility $13.5\,\mathrm{m^2\,V^{-1}s^{-1}}$. They assumed that the majority of the energy was stored electrostatically in the Hall field between the centre and the edge of the sample, and were able to estimate resistivities of the order of $10^{-14}\,\Omega/\Box$ for $\nu = 1, 2$ and $10^{-11}\,\Omega/\Box$ for $\nu = 4$. More recently Kershaw et al. [51] again observed a fast initial decay which decayed as a very fast exponential, followed by a long decay ~ 60 times longer than previously observed in the most extreme case. They demonstrated ρ_{xx} varied over the time of the decay, in the slow decay regime varied from $\rho_{xx} \sim 8.4 \times 10^{-13}\Omega/\Box$ to $\rho_{xx} \sim 4.3 \times 10^{-15}\Omega/\Box$, the lowest value observed to date.

In this section decays of induced currents in sample AK47 for $\nu = 1, 2$ and 4 are presented. The dilution refrigerator is operated in single-shot mode to keep mechanical noise, which appears as 'jumps', to a minimum. This limited the experiments to ~ 12 hours, as beyond this the temperature would start to drift upwards as the still is emptied.

4.7.2 Establishing a background

It was not possible to sweep sufficiently slowly that the eddy current vanished, in order to establish a zero for the current, i.e. the value of the magnetic moment decay at $t = \infty$ which corresponds to $I = 0$. By sweeping up and down over the field range of the current, an effective zero was estimated by taking the average of the two peaks. Figure 4.12 shows the hysteretic current for $\nu = 1$ at 100 mK. The magnetic field was swept over the range 9 to 11 T, then back to 9 T, shown as a black line. The field is then swept from 9 T to the centre of the eddy current (this is not shown in the figure, but the decay after being swept into can be seen in figure 4.13), and observed for ~ 10 hours. After this decay, the magnet is ramped down (blue line in figure 4.12), and in this instance the current decayed by less than 10 %.

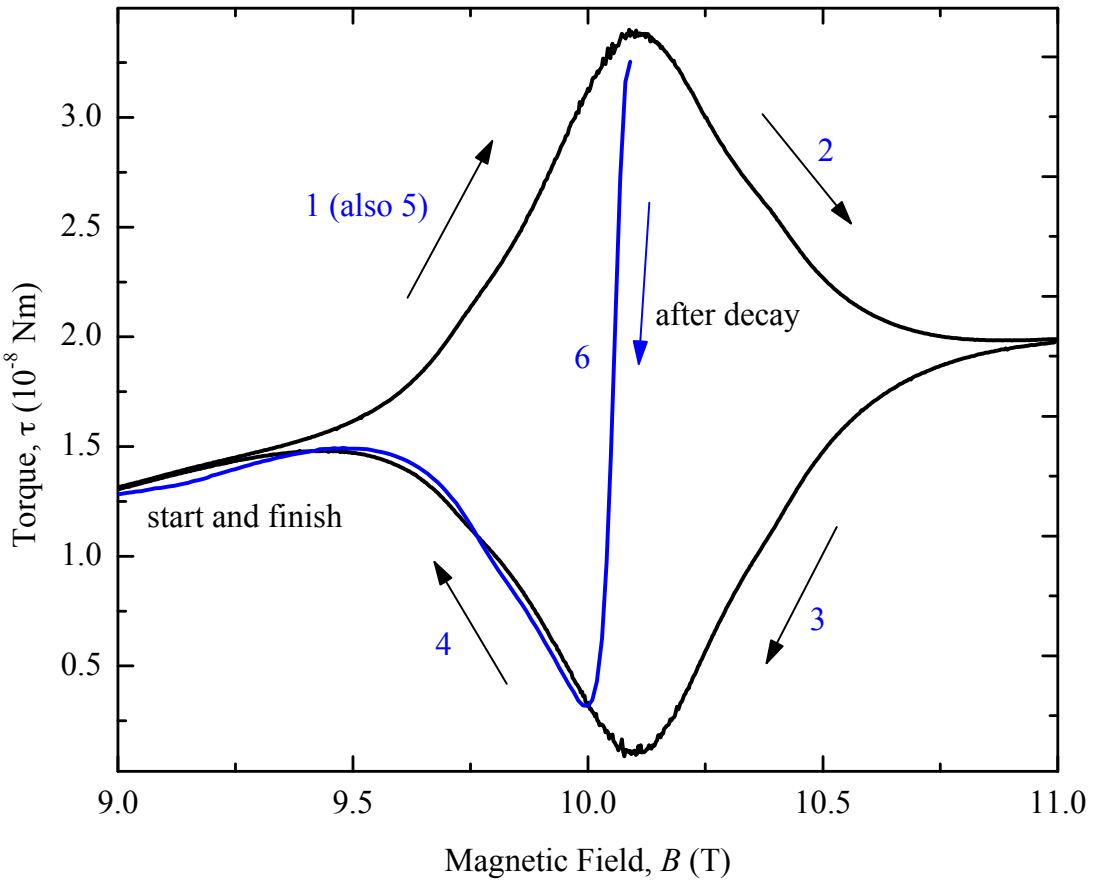

Figure 4.12: Establishing the 'zero' of the decay for $\nu = 1$ by mapping the background with an up and down sweep (black), and sweeping out after $\sim$ 10 hours. The current decayed by less than 10% in this time, with most of the dissipation happening in the first 20 s due to breakdown of the zero resistance state.

4.7.3 Decay of filling factors $\nu = 1, 2,$ and 4

The decay at $\nu = 1$ was measured at fixed field and temperature for 100 mK, 300 mK and 800 mK as in figure 4.13. The decay is characterised by a rapid initial decay which is attributed to breakdown of the QHE, followed by a slower return to equilibrium which for $\nu = 1$ is the less significant contribution. The eddy current in the slow regime is among the most persistent observed in such a system. Elevating the temperature increases the initial fast decay, but does not significantly change the shape of the slow decay. The initial decay of $\nu = 2$ reduced the current more than in $\nu = 1$, followed by a much slower decay, figure 4.14, which can be shown to obey

a power law as observed by Kershaw et al. [51].

Figure 4.15 shows $\nu = 4$, an even more extreme initial decay, that dissipated $\sim 50\%$ of the current in the first 20 seconds. A slower decay was again seen, but was still faster than that of $\nu = 1$ or 2, and decayed to less than 5% within $10,000$ s.

The general trend is for the current to dissipate a greater amount/faster with an increase in temperature. This can be understood by considering that the density of states is broader for a finite temperature and therefore the tails of the Landau levels will overlap more and have a higher ρ_{xx} to dissipate the current through.

Breakdown of the zero resistance state was seen in the IV characteristics of the eddy currents, as it is seen here in the decays. Without trying to explain the detailed mechanisms in the two different decay regimes, perhaps it is possible to predict the shape of the decay from the IV characteristics, but before doing so some consideration to the mechanism for the decay is required, which is the topic of the next section.

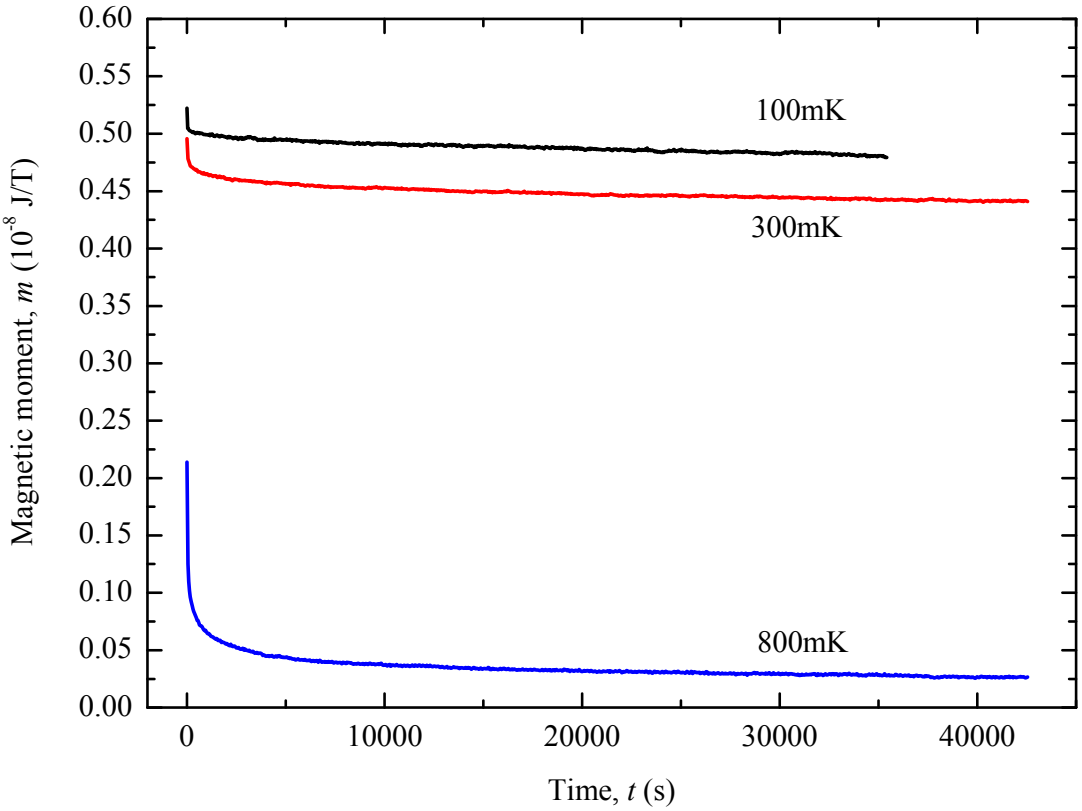

Figure 4.13: Induced eddy current decay for filling factor $\nu = 1$. Of the dissipated current, most is lost in the initial part of the decay, followed by an extremely persistent slow decay.

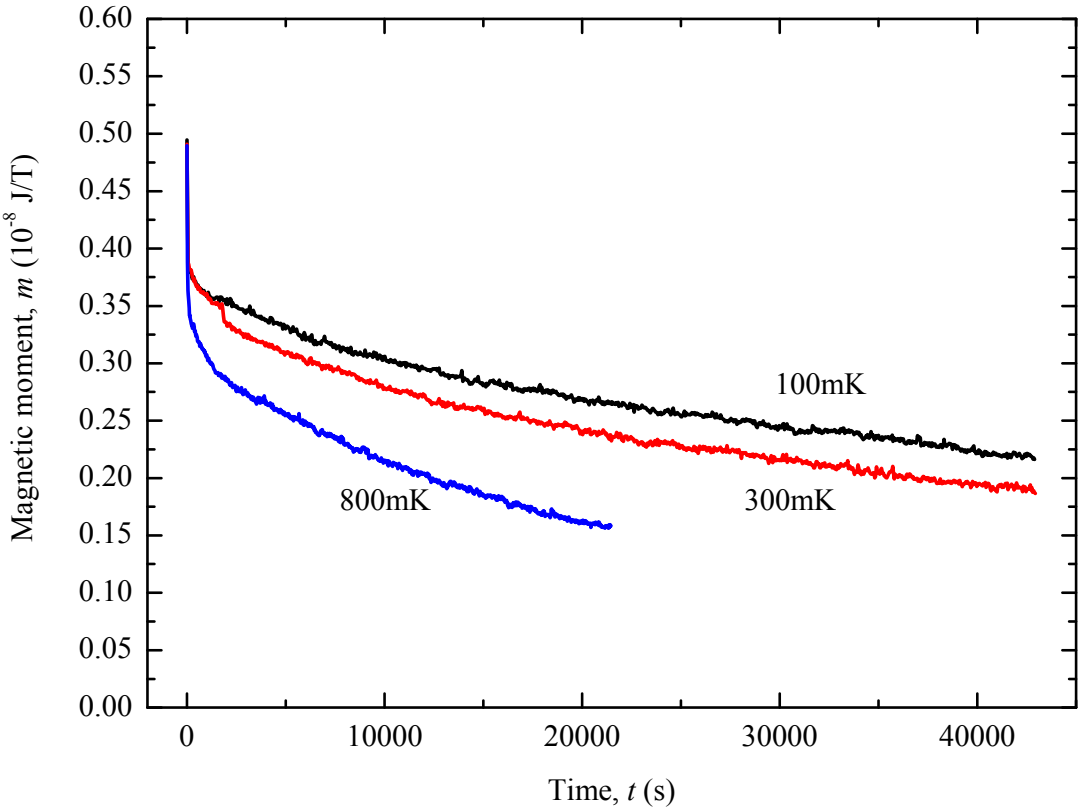

Figure 4.14: Induced eddy current decay for filling factor $\nu = 2$. A significant portion of the current is dissipated in the initial part of the decay, followed by a persistent slow decay of hours. The step in the 300 mK curve is due to ice cracking on the cryostat, causing a mechanical knock.

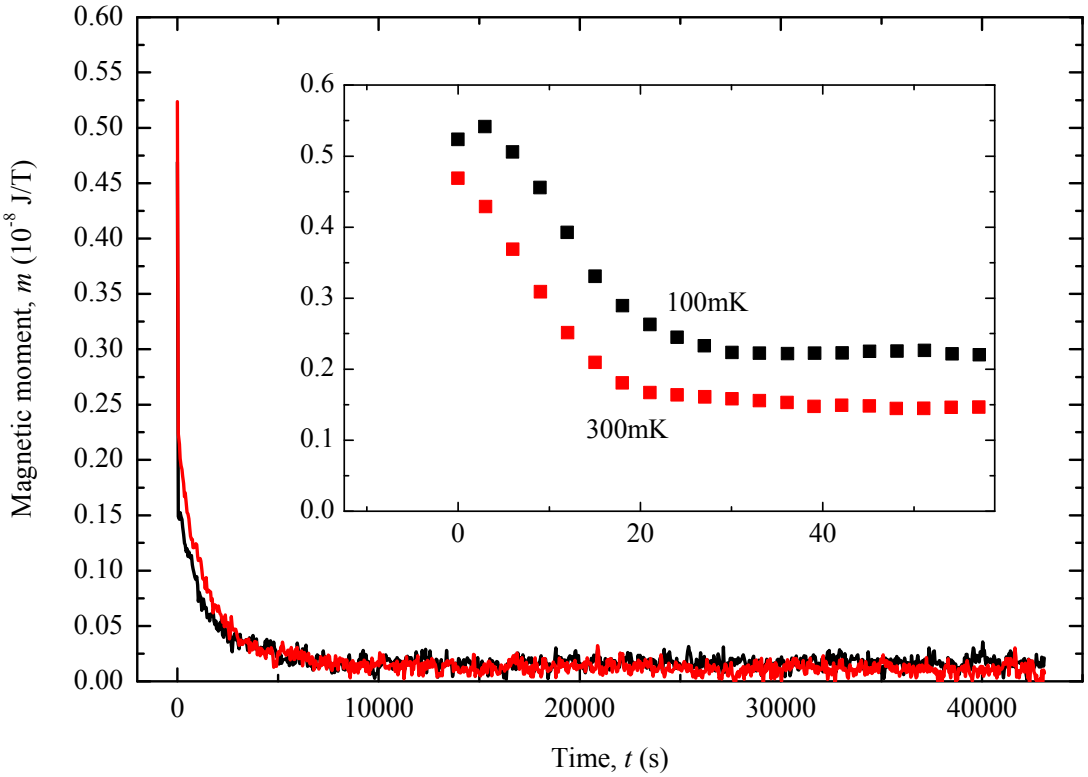

Figure 4.15: Induced eddy current decay for filling factor $\nu = 4$. Most of the current is dissipated in the initial part of the decay, followed by a slower decay of several hours.

4.8 Relating IV characteristics to induced current decays

The previously mapped IV characteristics of the induced eddy currents at various temperatures would be expected to govern how persistent an eddy current decay is. In this section, the shape of a decay is predicted by calculating the time varying resistance from the position on the IV curve in figure 4.10 is investigated.

When B was swept into an integer state at a constant rate corresponding to a constant EMF, the eddy current saturated. Upon reaching this field position and stopping, the applied EMF driving the current was zero, and energy was dissipated through the resistivity of the 2DES. The current was then reduced, and corresponded to a different position on such a curve, and to a different resistivity. Before discussing

the decay of the induced current, some attention will be given to how the energy is stored in this system.

4.8.1 Energy stored in an induced current

Haavasoja et al. [75] measured eddy current decay times of $\sim 300\,\mathrm{s}$ and were the first to consider the energy distribution of the eddy current. They calculated a capacitance for an edge state distribution, and the bulk case, then assumed a decay dictated by these calculated values and the resistance,

$$R = \frac{\alpha}{\sigma_{xx}} \approx \alpha \frac{\rho_{xy}^2}{\rho_{xx}}, \tag{4.10}$$

where α is a geometry factor. From the time constant $\tau = RC$ they calculated a resistivity of $\rho_{xx} \approx 10^{-11}\Omega/\square$ for the edge case and $\rho_{xx} \approx 10^{-10}\Omega/\square$ for the bulk. The fitted resistivity for the corresponding calculated inductance, this time assuming $R = \beta\rho_{xx}$ was an order of magnitude less. In 1995 Jones et al. [74] again compared capacitive and inductive energy storage of an eddy current. For an eddy current at 40mK, the energy associated with the self-inductance of the eddy current was calculated for $\nu = 1$ and 2 to be $10^{-16}\,\mathrm{J}$ and compared with a capacitive energy of $10^{-10}\,\mathrm{J}$ for $\nu = 1$ and $10^{-11}\,\mathrm{J}$ for $\nu = 2$. The authors concluded that the inductive energy storage was small compared to the capacitive, but had like Haavasoja et al., only considered the self inductance of the loop and not the mutual inductance of the loop in the presence of a solenoid carrying a large current. Jones et al. [74] in their model of discharging the eddy current state, comment that they do not in fact need to know an exact value for the capacitance to calculate ρ_{xx}. More recently Elliott et al. [76] commented that the decay time τ of Jones et al. [74] analysed as a discharge of the edge-weighted Hall field, although not quoted in the earlier publication, yielded

$$\tau = C_l\omega/\sigma_{xx}, \tag{4.11}$$

where C_l is the capacitance per unit length of the edge and ω is the effective width of the capacitor (the distance over which the Hall voltage is mostly dropped). However,

all the previous work neglected energy stored by mutual inductance. Jones et al. [74] calculated the self inductance of a current carrying loop, but overlooked the fact that it was at the centre of a large current-carrying solenoid.

Inductive energy

Consider the circuit in figure 4.16, which is a simplified representation of the 2DES located at the centre of a solenoid.

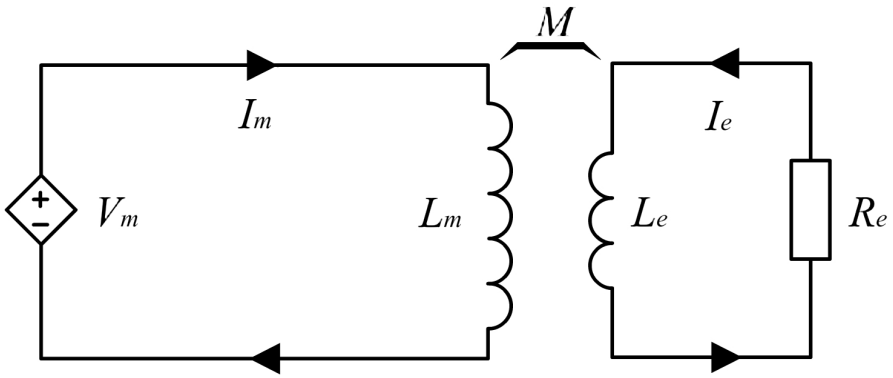

Figure 4.16: Simplified schematic of the magnet with inductance L_m coupling to the eddy current with an inductance L_e.

If a voltage V_{m} drives a time varying current in the inductor, i.e. the large superconducting magnet mentioned in chapter 3, the relation is given by

$$V_{\mathrm{e}} = I_{\mathrm{e}}R_{\mathrm{e}} = L_{\mathrm{e}}\frac{di_{\mathrm{e}}}{dt} - M\frac{dI_{\mathrm{m}}}{dt}, \tag{4.12}$$

and

$$V_{\mathrm{m}} = L_{\mathrm{m}}\frac{di_{\mathrm{m}}}{dt} - M\frac{di_{\mathrm{e}}}{dt}. \tag{4.13}$$

By considering the work done by source V_{m},

$$\varepsilon = \int_0^t V_{\mathrm{m}} I_{\mathrm{m}} dt, \tag{4.14}$$

it can be shown

$$E_{total} = \frac{1}{2}L_m I_m^2 + I_m I_e M + \frac{1}{2}L_e I_e^2, \tag{4.15}$$

where the mutual inductance $M = k\sqrt{L_m L_e}$, and $-1 \leq k \leq 1$ is a coupling coefficient (after Grover [77]). Terms involving I_e are those that will decay with time, the first term is not part of the 2DES energy. Out of the last two terms it is clear that energy stored in the mutual inductance is going to be significant because I_m is large compared to I_e. It is possible to calculate the mutual inductance M knowing the geometry of the two loops, but not necessary here. Another way to view the last term is as the magnetic potential energy arising from bringing the magnetic moment m caused by I_e in an area A, from infinity into a magnetic field of strength B, which is,

$$I_m I_e M = B.m, \tag{4.16}$$

where m is the magnetic moment of the eddy current. This term can be either positive or negative depending upon the orientation of the magnetic moment in the magnetic field, but Lenz's law means that for induced currents it is negative. The energy stored in the mutual inductance for an induced current of 0.29 mA for filling factor $\nu = 4$ is shown in table 4.2.

To estimate the self inductance of the loop of this sample the same method was followed as in Jones et al. [74] for comparison. The most extreme case is that the current flows within a distance ℓ_0 of the sample edge. ℓ_0 is on the order of the spatial extent of the electronic wavefunction in the z direction, therefore assume a simple wire loop of radius R and then the inductance can be calculated from

$$L = \mu_0 R \left[\ln\left(\frac{8R}{\ell_0}\right) - \frac{7}{4} \right]. \tag{4.17}$$

Here μ_0 is the permeability of free space (Grover [77]). For R it is adequate to assume a radius which corresponds to a sample area equal to the rectangular AK47, $R \approx 1.8 \times 10^{-5}\,\mathrm{m}^2$. This is again calculated for $\nu = 4$ in table (4.2).

Capacitive energy

Consider the energy associated with relocating the charge to the edges of the sample from a geometry argument. The eddy current density is important, but for this calculation it is assumed to exist near the edge of the sample and is maintained by a Hall voltage V_{H}. Scott and Wolfe [78] derive the capacitance per unit length of two parallel wires, as used by Jones et al. [74],

$$C_\ell = \frac{\pi\varepsilon_0\varepsilon_r}{ln\left[\frac{D+(D^2-4w^2)^{1/2}}{2w}\right]}, \tag{4.18}$$

of wire radius w and separation D, and ε_r is taken to be 13.1.This is only valid for the limit $D > w$. To put a limit on the radius of the wire, again use the spatial extent of the electronic wavefunction in the direction perpendicular to the applied magnetic field $\sim 10^{-8}\,\mathrm{m}$ which is approximately the magnetic length of the system, so it is an adequate approximation to use ℓ_0. If the current was considered to be an edge state then the separation D would be comparable to the magnetic length and the assumption of $D > w$ breaks down. The current is almost certainly edge weighted, and as experiments have shown probably extends over several μm, a reasonable guess would therefore be $1\,\mu$m using the estimates of MacDonald et al. [72].

A second way to make an upper estimate is to simply consider the capacitance from relocation of the charge to the edge of the sample due to a Hall voltage,

$$C = \frac{Q}{V_{\mathrm{H}}}, \tag{4.19}$$

where the Hall voltage is given by

$$V_{\mathrm{H}} = I.\frac{h}{\nu e^2}. \tag{4.20}$$

An estimate for Q is needed. The current is known, but in the QHE there is the rather odd situation that an electron may navigate the perimeter of the loop many

times before being scattered. The mean free path of the electrons is,

$$l = v_{\mathrm{F}}\tau, \tag{4.21}$$

where τ is the scattering time, and the Fermi velocity

$$v_{\mathrm{F}} = \frac{\hbar k_{\mathrm{F}}}{m*} = \frac{\hbar}{m*}(4\pi n_s/g_s g_v)^{1/2}. \tag{4.22}$$

where n_s is the sheet density, $m*$ is the effective mass, g_s the spin degeneracy and g_v is the valley degeneracy. For the 2DES, this estimates $v_{\mathrm{F}} = 1.93 \times 10^5\,\mathrm{m\,s^{-1}}$. Knowing this, the charge Q can be calculated from the circulating current, where

$$current = charge \times velocity, \tag{4.23}$$

therefore

$$Q = \frac{I_e}{v_{\mathrm{F}}} = 1.50 \times 10^{-9}\,\mathrm{C} \tag{4.24}$$

The Hall voltage sustaining the charge separation is

$$V_{xy} = I_e.R_{xy}, \tag{4.25}$$

which is filling factor dependent. The energy stored in such a capacitance is given by,

$$E = \frac{1}{2}QV \tag{4.26}$$

This gives an upper estimate for the energy stored in the capacitance of the system and is an order of magnitude less than that stored in the inductor.

	Calculated value	Energy
Self inductance of loop	$4.2 \times 10^{-8}\,\mathrm{H}$	$1.76 \times 10^{-15}\,\mathrm{J}$
Mutual inductance of loop with magnet	—	$1.31 \times 10^{-8}\,\mathrm{J}$
Capacitance using geometry	$3.55 \times 10^{-14}\,\mathrm{F}$	$5.12 \times 10^{-13}\,\mathrm{J}$
Capacitance using Q estimate	$8 \times 10^{-10}\,\mathrm{F}$	$1.41 \times 10^{-9}\,\mathrm{J}$

Table 4.2: Comparison of energy storage for eddy current at $\nu = 4$, for a saturating current of 0.29 mA at base temperature.

Previous estimates by Jones et al. for the capacitively stored energy are $\sim 10^{-10}$ J, more than the geometry estimate here, but less than the alternative method by two orders of magnitude. Jones et al. used some slightly different assumptions which can account for the geometry capacitance discrepancy, but both calculations are possibly an underestimate of the stored energy. Ignoring this discrepancy, the values for the inductance are of equal magnitude to the calculated capacitance in this system, so certainly cannot be disregarded easily. Since even the upper limit of the electrostatic energy is below the $I_{\mathrm{e}}.M$ contribution, the eddy current decay is of magnetic origin, not as previously thought electrostatic.

4.8.2 Discharging an eddy current

It has been demonstrated that the energy stored in an eddy current is partly capacitive and partly inductive. In either case, the eddy current is circulating towards the edge of the sample and must relocate back into the 'bulk' 2DES somehow, as the induced current decays. To be consistent with the findings of the previous section, the induced current will be assumed to decay inductively, with an effective inductance corresponding to the total energy stored. In principle it does not matter where the energy is stored for the purpose of predicting a decay curve from an induced current IV, an effective capacitance could be assumed with time constant $C_{\mathrm{E}}R$ (where $R \propto 1/\rho_{xx}$), or an effective inductance L_{E}, with time constant L_{E}/R (where $R_{\mathrm{L}} \propto \rho_{xx}$). When discharging the effective inductance L_{E} through a resistance R, the current I at time t is

$$I = I_0 \exp\left(\frac{-Rt}{L_{\mathrm{E}}}\right), \tag{4.27}$$

where I_0 is the initial current at $t = 0$. In a small time interval dt, an amount of current dI has decayed,

$$dI = -\frac{I_0 R}{L_{\mathrm{E}}} \exp\left(\frac{-Rt}{L_{\mathrm{E}}}\right), \tag{4.28}$$

so

$$dI = \frac{-RI}{L_{\mathrm{E}}} dt. \tag{4.29}$$

Consider the sweep rate IV curve for an eddy current in figure 4.17. The starting point on the sweep rate IV curve is the EMF at which the induced current was established. The instantaneous resistance R_1 can be calculated from the curve, and using equation 4.29 the current dissipated dI, in a time dt is calculated. A new I corresponds to a new resistance R_2, which can be used to calculate the next dissipation dI. This iterative process is used to predict the shape of an induced current decay, where R is proportional to ρ_{xx}. The effective capacitance L_{E} is used as the variable fitting parameter, but again, it is the general shape of the curves that is the aim of the investigation.

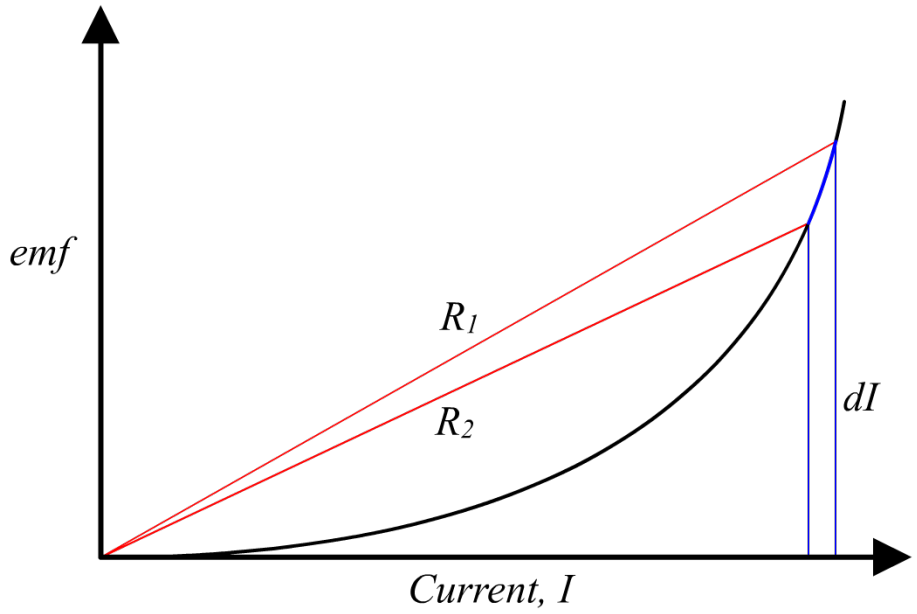

Figure 4.17: Calculating dissipation from a sweep rate IV curve for an induced current. Starting at an arbitrary current, a resistance is calculated, and I is dissipated through the resistance R_1 in a time interval dt. A new current is then used calculate a new resistance R_2, and the process is repeated.

Of the sweep rate IV characteristics measured, figure 4.10, not all have sufficient detail to compute a decay. In order to make a good estimate there needs to be sufficient data near the shoulder, i.e. information about the current outside of the saturated regime. Filling factor $\nu = 6$ has lots of detail, but the decays did not exhibit the long decay due to the finite resistance of ρ_{xx}, so these are of little interest. $\nu = 4$ again has a smooth turn over from the saturated regime, but the decays are not as persistent as for $\nu = 1$ or 2. The saturation regime of $\nu = 2$ was very

robust, and sweep rates slow enough to reduce the amplitude of the induced current significantly were not achieved. For $\nu = 1$, the highest temperature experiment of 800 mK, is the best candidate.

$\nu = 1$ **at** 800 mK

The $\nu = 1$ sweep rate IV curve for 800 mK from figure 4.10 is replotted in figure 4.18 as V vs. I. As discussed earlier, measuring currents for smaller EMFs was experimentally limited. At zero dB/dt (zero EMF), the induced current must be equal to zero. When the lowest measured EMF is interpolated to zero, the decay this produces is not as persistent as measured in experiment, because the resistance this predicts is too large.

The detail around the turning point, and how fast the EMF approaches zero is important. By choosing a function that fits the data a much smoother decay is predicted. The function was chosen because it meets the following criteria:

1. It drops to near-zero fast, with decreasing current.
2. It is a symmetrical function (current reverses direction with a negative EMF), and
3. It fits the data well, however, no claim is being made for a physical reason why the sweep rate curve should follow this trend.

The function which best satisfies these criteria is

$$V = P_1 \times \sinh(P_2 \times I)^3, \tag{4.30}$$

where P_1 and P_2 are fitting parameters.

The fit to the corresponding decay data was computed and is shown in figure 4.19. The resultant modeled decay closely matches the experimental data. It would be

possible to generate a decay that is more persistent, but without more data points on the sweep rate/ induced current curve there is no justification for doing so. This suggests that there is some hidden structure to the IV curve, and a physical justification needs to be found before the model can be improved. If lower sweep rates could be achieved, then there would be no need to fit a function at all for the purpose of generating a theoretical eddy decay.

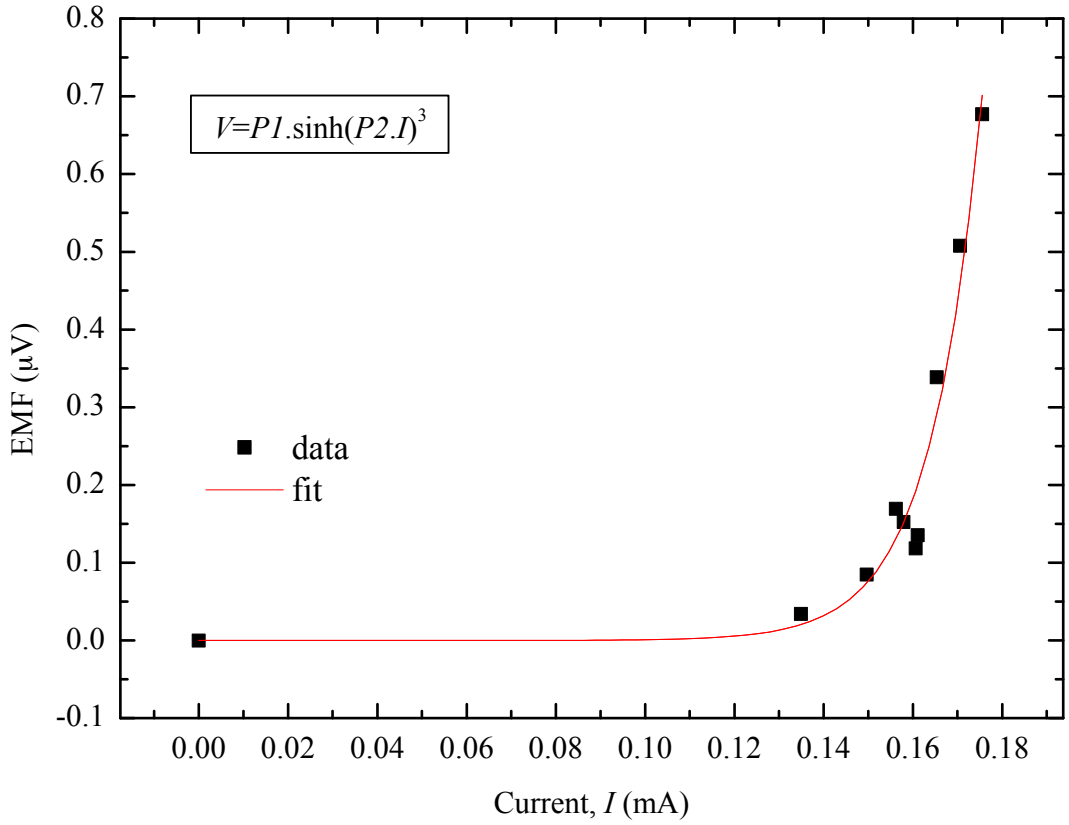

Figure 4.18: Sweep rate curve for induces current $\nu = 1$ at 800mK, with fitted function.

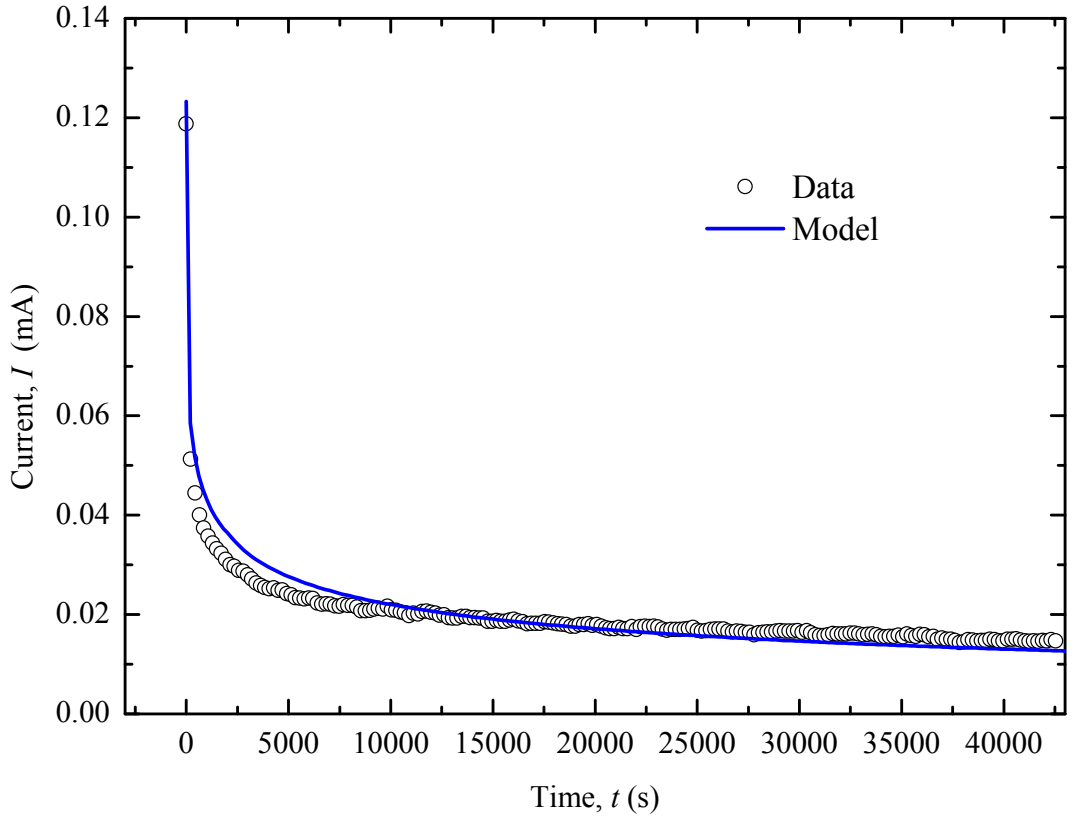

Figure 4.19: Decay of $\nu = 1$ at 800 mK. The blue curve is computed from the sweep rate IV curve, and follows the trend of the data.

4.9 Conclusions

Induced currents in a two dimensional electron system at low temperature and high magnetic fields have been studied. The temperature dependences of the eddy currents were measured over the range 100 mK to 1600 mK. Currents induced at even filling factors were more robust than odd filling factors for the same Landau level index, consistent with the cyclotron splitting being larger than the spin splitting. The peak current at filling factor $\nu = 2$ was shown to saturate at $\gtrsim 800$ mK, more robust than previously observed, but was reduced by elevating the temperature to 1600 mK. The saturated regime is associated with a breakdown of the quantum Hall effect, and in this case, the most likely candidate is an electron heating effect. The shapes of the temperature dependences of the induced eddy currents were compared

to predictions of the charge up model used by Kavokin et al. [70], and qualitatively agreed. It is interesting to note that if electron heating is responsible, then the eddy current must be de-coupled from the transport current, as T limiting is not evident in the transport measurements.

Sweep rate dependence's were characterised for a range of filling factors and temperatures, and even for the lowest sweep rates, never entered a linear regime. Induced currents $\nu = 1, 2$ and 4 all saturated at the same critical value at 100 mK, but $\nu = 4$ was shown to reduce with slower sweep rates, consistent with the prediction that the ρ_{xx} minima is not as small as for lower LL's, so is harder to drive into breakdown.

Induced current decays were measured to be similar to previous work, a fast initial decay attributed to breakdown of the QHE followed by a much longer slow decay. The eddy decay of $\nu = 1$ at low temperature, in the slow decay regime, is among the most persistent reported. Surprisingly, the $\nu = 2$ decay was faster than the $\nu = 1$, somewhat inconsistent with the temperature and sweep rate dependence's measured. The long decay of $\nu = 1$ suggests that, whatever the mechanism for the decay, spin is conserved.

The energy stored in an induced current was discussed, and it was shown that the assumptions of previous work had not evaluated the mutual inductance of the eddy current in the presence of the magnet sufficiently. The sweep rate IV characteristics were considered as a good description of the induced current for a given temperature, that could predict the shape of the eddy decays. By fitting a suitable function to the IV characteristic of $\nu = 1$ at a relatively high temperature to interpolate the behaviour near the turning point of the curve, and using a relatively simple discharge model, the shape of the induced current was modeled. The model showed close agreement to the data, producing a similar shape and a very long time constant for the slow decay.

Chapter 5

Hysteresis in the conductance of a QPC

5.1 Introduction

A quantum point contact (QPC) is a short and narrow constriction in a 2DES with dimensions comparable to the the Fermi wavelength. They were first fabricated and investigated by two independent research groups in 1988: Van Wees et al. [79] and Wharam et al. [80]. The novel result was that the conductance of a quantum point contact is entirely quantised in units of $2e^2/h$, which is reminiscent of the quantum Hall effect, but is measured in the absence of a magnetic field, because the effect is due only to the reduced dimensionality of the system (figure 5.1). On application of a magnetic field there is a smooth transition to the quantum Hall effect which arises because the current is equally partitioned into an integer number of propagating modes in the constriction, each one carrying $2e^2/h$ multiplied by the longitudinal voltage V.

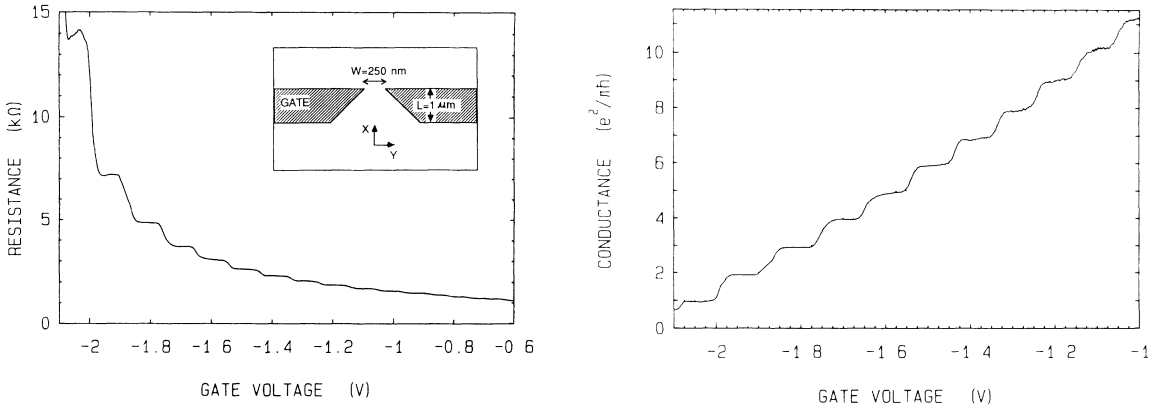

(a) (b)

Figure 5.1: The first experimental realisation of quantised conductance in zero magnetic field. The constriction is tunable; the width decreases, pinching off conducting channels, as the gate voltage is made more negative. (a) Quantum point contact resistance as a function of gate voltage at 0.6 K. The inset shows the split gate electrodes deposited remotely from the 2DES. (b) Quantum point contact conductance as a function of gate voltage obtained from the data in (a), after an adjustment for a series lead resistance. The conductance shows plateaus at multiples of $e^2/\pi\hbar$. Images taken from Van Wees et al. [79].

A typical device would be a made from a (GaAs)/(Al,Ga)As quantum well where the electrons are initially confined to a two-dimensional plane, with a metallic gate grown remotely on the surface by electron beam lithography. The point contact has to be defined electrostatically through the application of a negative (with respect to the conducting reservoir of the 2DES) bias voltage to the split-gate. The width of the gate is therefore tunable, and can typically be tuned from $0 \lesssim W \lesssim 250\,\mathrm{nm}$, which is comparable to the Fermi wavelength in GaAs, $\lambda_\mathrm{F} \backsim 40\,\mathrm{nm}$, yet much smaller than the mean free path $l \sim 10\,\mu\mathrm{m}$. For this reason, the conduction through the QPC can be considered entirely ballistic. The confining potential at the QPC is a saddle-point potential, but for low magnetic fields has a flat bottom. The conductance is quantised into a series of steps with each 1D sub-band in the constriction contributing $2e^2/h$ to the conduction. Since the number N of occupied sub-bands is necessarily an integer, it follows that the conductance G is quantised,

$$G = (2e^2/h)N.$$

In 2006 Pioro-Ladrière et al. [81] reported hysteretic effects in magneto-transport experiments on lateral quantum devices. The devices were fabricated from a 2DES in a standard GaAs/(Al,Ga)As single heterojunction, with an electron density of $1.7 \times 10^{15}\,\mathrm{m}^{-2}$ and an electron mobility of $200\,\mathrm{m}^2\mathrm{V}^{-1}\mathrm{s}^{-1}$. They investigated effects for a fixed gate width, set to a conductance below $2e^2/h$, for a range of sweep rates in magnetic fields up to 10 T. When the hysteretic features were swept into, a decay was observed with two distinct relaxation times, one of minutes and the other of days. It was suggested that the observed behaviour was related to induced eddy currents. Induced currents in the quantum Hall regime are not thought to contribute to, or couple to, the conducting current in standard transport measurements, as they do not flow into the contacts. The authors confirmed that eddy currents did indeed behave in the same way as the hysteretic magnetoconductance, by explicitly measuring them with torsion-balance magnetometry on a sample of the same 2DES material. The observations showed that the induced quantum Hall potential at the edge of the 2DES reservoir influenced the transport through the devices.

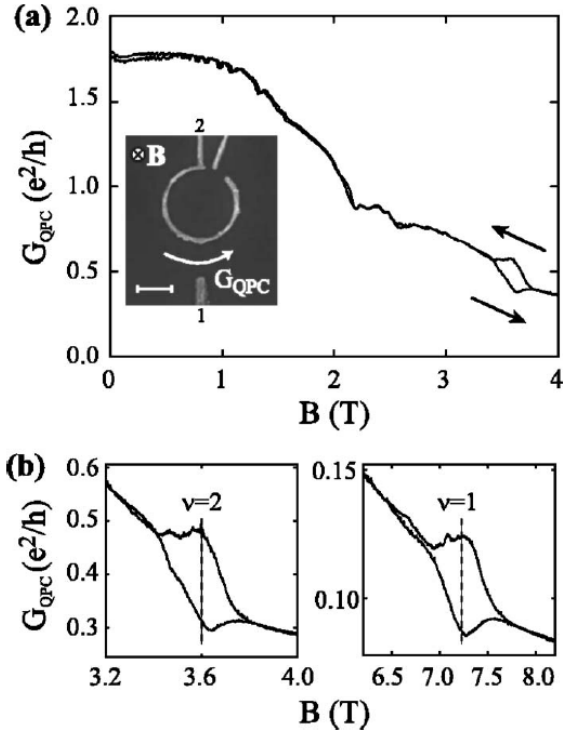

Figure 5.2: Magnetoconductance measurements on a quantum point contact at a sweep rate of $17\,\mu\mathrm{T\,s^{-1}}$ and a temperature of 30 mK, taken from Pioro-Ladrière et al. [81]. (a) The conductance G_{QPC} as a function of magnetic field B, with a hysteretic feature at 3.6 T, corresponding to filling factor $\nu = 2$ (in the 2DES leads). The inset shows an electron micrograph of the device, the scale bar is 300 nm. The quantum dot in the upper gate plays no role in this experiment. (b) (left) An enlargement of the hysteretic feature at $\nu = 2$ and (right) the hysteretic feature at $\nu = 1$.

The inset to figure 5.2(a) shows an electron micrograph of the quantum point contact used in the experiment, and the width of the lithographically defined gate is $\sim$ 300 nm. In addition to the novel hysteretic peaks, non-hysteretic $1/B$ oscillations are seen, associated with oscillations in the electrochemical potential for electrons giving rise to the Shubnikov–de-Haas effect in the 2DES leads.

The explanation offered for the hysteresis is that eddy currents are induced in both 2DES leads, as shown in figure 5.3. There will be a radial Hall field associated with such a current and therefore a transfer of charge from the centre to the edges of the 2DES leads. For an up-sweep, the edges become positively charged, and the region adjacent to, and under, the gate becomes depleted, hence the conduction through the QPC decreases, and vice versa, increases for a down sweep. Additionally, this

experiment confirms that the eddy currents flow near the edge of the sample.

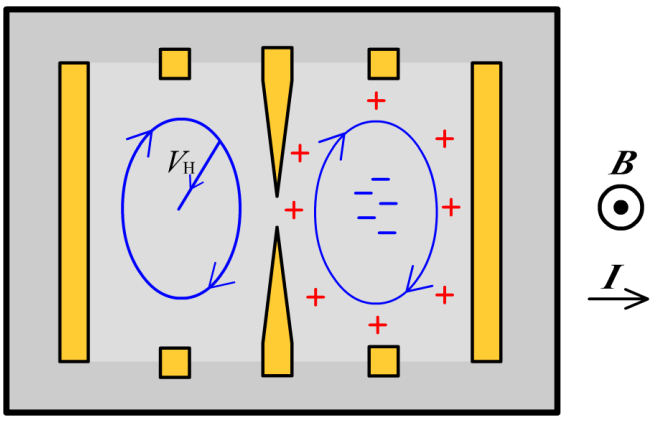

Figure 5.3: A schematic illustration (not to scale) of the induced current in the 2DES, leads have a Hall voltage which perturbs the potential near the QPC. The radial Hall fields results in a positive charge build up near the gates. The barrier appears shorter to the ballistic electrons and therefore the device has a corresponding dip in magnetoconductance.

This chapter describes an experiment that extends on the work of Pioro-Ladrière et al. by measuring the magnetoresistance of a QPC at the same time as measuring the magnetisation of the same sample, to build up a picture of how the hysteretic features change when the size of the eddy current varies. It is shown that there are features in the magnetoresistance at $\nu = 1$, $\nu = 2$ and for the first time, $\nu = 4$. The temperature dependences of the eddy currents and features are characterised and shown to be consistent. The sweep rate dependences are shown to be similar, and a sweep rate dependence for $\nu = 4$ is observed which has not been reported previously. Once a persistent eddy current has been established in the sample it is observed to decay in similar ways for both measurements. It will also be possible to infer how close to the edge the eddy currents flow, because the magnetisation gives the magnitude of the induced current, but the QPC only detects local perturbations to the 2DES charge density.

In the previous chapter, it was shown that for lower temperatures and high sweep rates the breakdown of the quantum Hall effect was evident by the current saturating. Looking in more detail at the induced current peaks for critical currents, the onset of breakdown of the quantum Hall effect is apparent by an increase in noise

as observed by Elliott et al. [76], which has been proposed as an example of self organised criticality. In this chapter, an increase in noise at integer filling factors is measured for faster sweep rates, and by using fast sampling rates (time constants of $\sim 10\,\mu$s) the underlying structure of the noise is measured, and is the same for both measurements, i.e identical individual breakdown events in both the induced current and the magnetoresistance correlate with time. This is evidence that both effects are due to the same underlying mechanism, and that induced currents are that mechanism. Finally, it will be shown that although the eddy currents can affect the electrostatic potential near the point contact, the gate has no effect on the size or decay rate of the induced current.

5.2 Experimental setup

The magnetisation was measured using the torque magnetometry technique discussed in chapter 3.4. The quantum point contact was mounted onto a conventional Stycast rotor, with a GaAs dummy sample containing no 2DES mounted on the opposite side. The samples were glued with GE varnish [43] to thin cigarette paper [82], which was then glued to the rotor, again with GE varnish. Glueing to paper meant that the sample could be removed with ease from the rotor if needed, GaAs is rather brittle and removing samples that have been glued directly to the rotor had previously prooven problematic.

Silver-loaded paint [45] contacts are made to the QPC, as can be seen in figure 5.4, to connect insulated copper wire [83] twisted pairs (approximately 3 twists/mm) to the dilution fridge wiring loom. To perturb the mechanical properties of the experiment as little as possible the twisted wire pairs were glued to the stycast rotor with superglue [84] and run parallel to, but not touching, the torsion fibre. The wires were GE varnished to the torsion fibre mounting posts, then additionally varnished to the body of the magnetometer, so as to minimise their contribution to the torque.

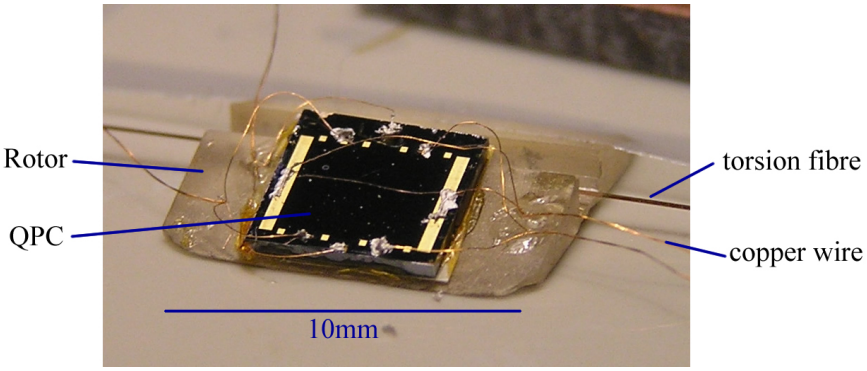

Figure 5.4: Stycast rotor with QPC sample AK47 mounted before being fitted in the magnetometer frame. Insulated copper wires connect to the gold pads on the QPC with silver paint contacts, and are fixed to the edge of the rotor with superglue.

The primary aim of the experiment was to measure simultaneously the induced currents with magnetometry, and the magnetoresistance through a transport measurement. The experimental principles of magnetometry have been described in chapter 3 and requires little modification for this experiment. One lock-in amplifier (EG&G dual channel 7265) was used to measure the small signal output from a differential capacitance bridge, and a second lock-in (EG&G dual channel 5210) used for a standard low frequency AC transport measurement. Initially the QPC resistance was measured with a two-lock-in measurement to establish the current did not vary. Unless otherwise stated, the same bias voltage was applied to both gates with respect to one side of the conducting channel. The sample, AK47, is a single layer GaAs/(Al,Ga)As quantum well structure with a measured mobility of $1.03 \times 10^6\,\mathrm{cm^2\,V^{-1}\,s^{-1}}$, grown at the Institute for Microstructural Sciences, Canada and processed by Dr Alicia Kam.

5.3 Characterising QPC AK-47

For this investigation both the lock-ins were used to measure the resistance of the device. The gate potential was applied by reducing the $\pm 10\,\mathrm{V}$ DAC output from a lock-in amplifier (7265), with a potential divider (not pictured) to give a resolution of $\sim 1\,\mathrm{mV}$, and a $1\,\mathrm{G\Omega}$ protection resistor to limit current. The experiments pre-

sented in this chapter were conducted in the second of two separate cool downs (i.e. raised to room temperature between sets). Noise in the form of 'jumps' in the magnetoresistance from one stable state to another, possibly arising from trapped charge underneath the gates, were problematic in the first cool down. In the second cool-down, a bias voltage of +0.26 V was applied to the split gate after Pioro-Ladriere et al. [85], which improved the stability of the conduction through the QPC.

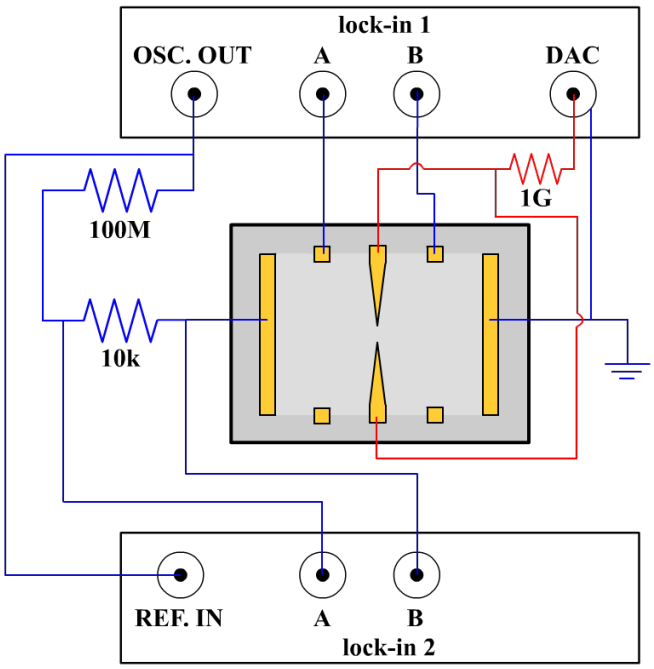

Figure 5.5: Experimental set-up for measurement of voltage drop along QPC using the primary lock-in as a constant current source. The second lock-in is used to measure the small voltage drop across a 10 kΩ resistor, and hence the QPC current, it is removed for the simultaneous experiments.

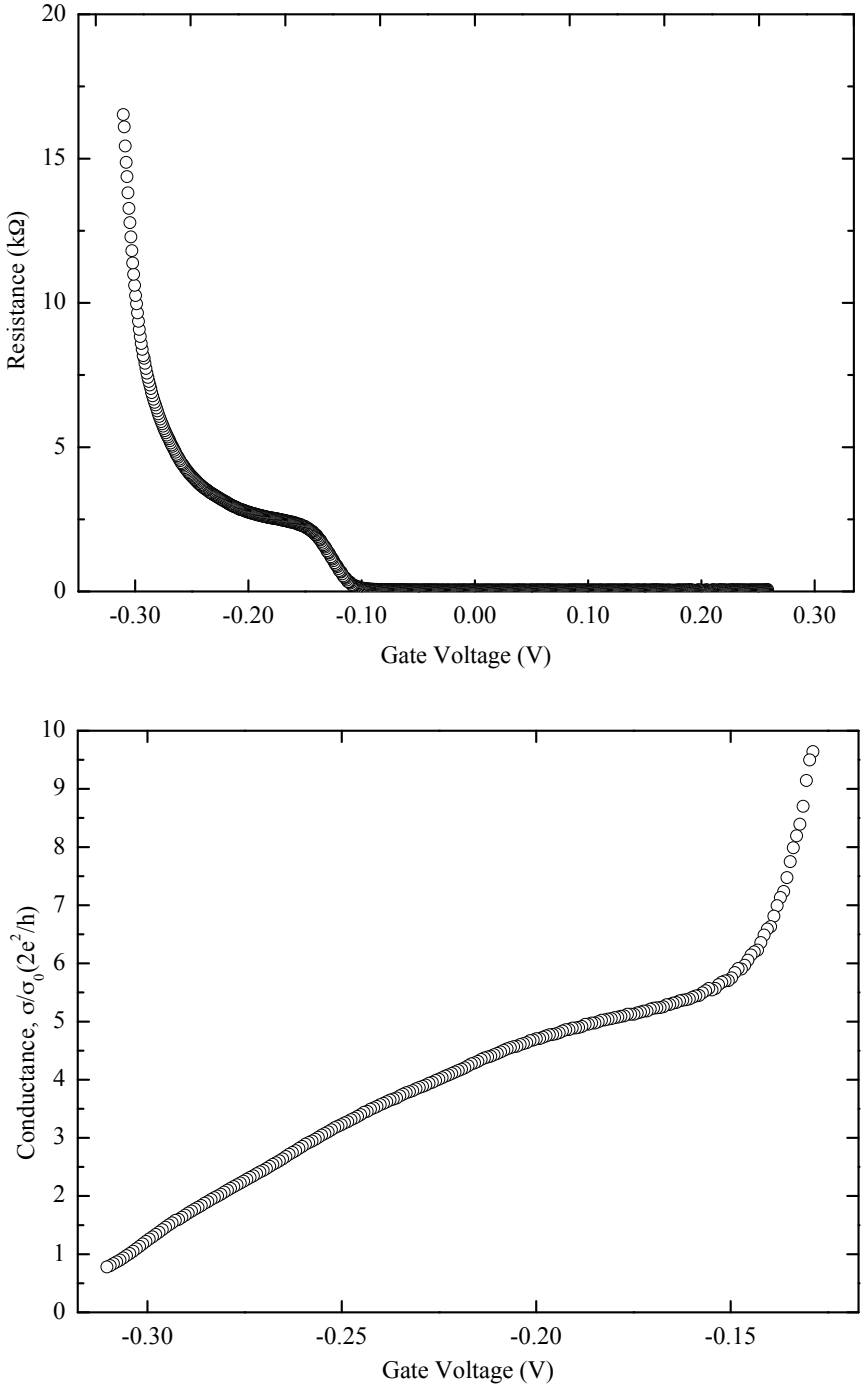

Figure 5.6: (top) QPC resistance measured at 50 mK with a 10 nA excitation current, and (bottom) The corresponding conductance trace. The conductance can be reduced to below $2e^2/h$ where all conduction is due to tunneling. The sensitivity of the lock-in was set to resolve any steps present, and therefore limits the scale. Only one discrete step in the conductance is seen, at ~ -0.12 V, which corresponds to the number density underneath the gate becoming zero, and the constriction becoming the only remaining current path. The expected steps are smeared, but the gate can still be 'pinched-off'.

Figure 5.6 shows the longitudinal resistance R_{xx} as measured through voltage contacts either side of the gate, and current monitored by a second lock-in at zero magnetic field. The expected structure of such a trace is shown in figure 5.1, quantised resistance plateaux over a wider range of gate voltage. Scanning electron microscope imaging in figure 5.7 established that the defined lithographic width of the gate was 509.4 nm which was ~ 160 nm wider than the designed width. A possible explanation for the QPC pinching off over a very short range of gate voltages, and therefore smearing the defined steps, is because the defined gates are far apart compared with the depth of the quantum well from the surface. The parabolic potential at widths of $\sim \lambda_F$, will therefore be a well farther from a square well approximation. The energy levels will be closer together, and therefore will not be separated as far in terms of gate voltage, and appear smeared when the bottom of the electrostatic-defined well is raised.

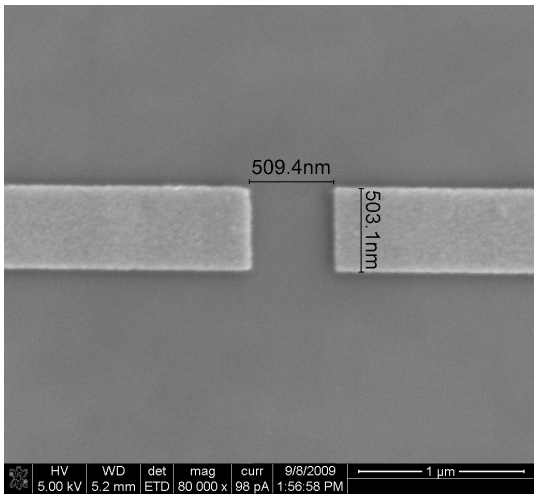

Figure 5.7: SEM image of AK47. The lithographed width is measured to be 509.4 nm.

To understand the trace of QPC resistance versus gate voltage there are several checks that can be made to confirm the gate is working as expected. By going to a filling factor at a specific magnetic field value in the bulk at zero gate voltage, and then sweeping V_g, edge state conducting channels will be scattered as the area underneath the gate becomes depleted.

In the experiment, the gate was set to the effective zero of +0.26 V, and the magnetic field set to a value corresponding to integer filling factor, as established through a Shubinikov—de-Haas measurement. The split gate was then swept, decreasing V_{g} at a constant rate, and the longitudinal resistance measured for filling factors 1 to 8. The expectation was that as n_{2D} was reduced, conducting edge states would be pinched off, and steps seen in the resistance. Similar experiments have been performed, such as by Haug et al. [86], who investigated conduction between two conducting 2DES areas separated by a 10 μm and a 20 μm long gated region. They observed oscillations in the resistance that they attributed to the occurrence of even filling factors in the gated region. The period of the oscillation was consistent with the change in the carrier concentration expected for the known parameters of the sample, via an equation for the capacitance,

$$\Delta n_{\mathrm{2D}} = \frac{\epsilon_{\mathrm{r}}\epsilon_0}{ed}\Delta V_{\mathrm{g}}, \tag{5.1}$$

where d is the distance between the metal gate and the 2DES, ΔV_{g} the change in the gate voltage and Δn_{2D} the resulting change in carrier concentration. Figure 5.8 shows the V_{g} dependence of R for different filling factors. As gate voltage was decreased, n_{2D} under the gate was depleted, and peaks in the resistance were measured. The peaks in resistance occurred at integer fractions of the V_{g} value of the single 0 T step, i.e. for $\nu = 2$, there is a feature halfway between the $\nu = \infty$ step and the effective zero.

With the 2DES leads at filling factor 8 and the gate initially at the effective zero bias, conduction from source to drain is the same as in an ordinary 2DES wide channel system. As number density is reduced under the gate, the uppermost Landau level is excluded from under the gate, and only three conducting edge states are left under the gate. The strongest back-scattering occurred at precise fractions, when the Landau levels are completely full, rather than discrete steps. The QPC plays little role in this experiment, except to act as a parallel resistor.

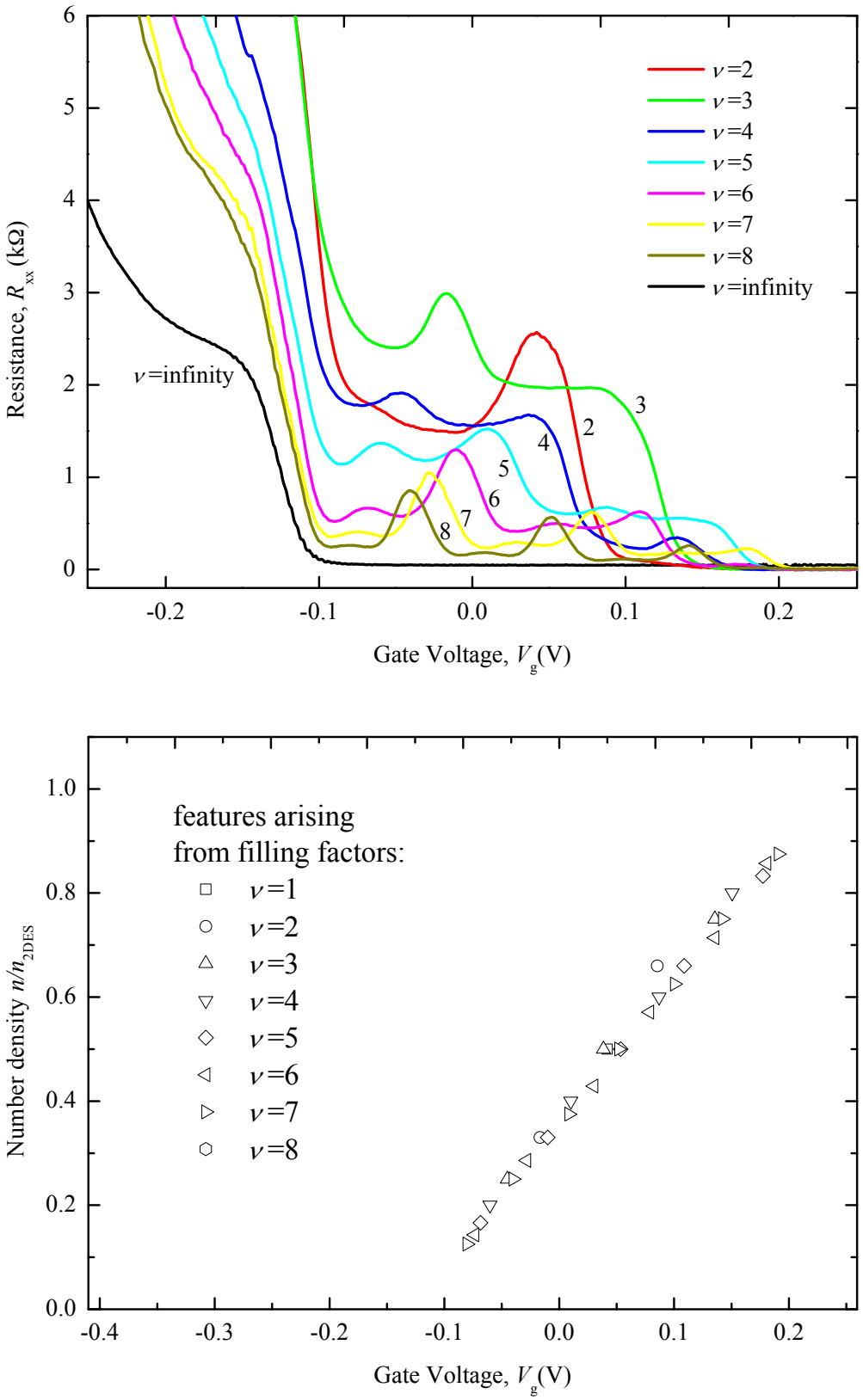

Figure 5.8: Sweeping gate voltage at various fixed magnetic fields corresponding to filling factors. As gate voltage is decreased edge state conducting channels are pinched off and back-scattered at the interface resulting in a resistance plateau. Steps are unexpectedly preceded by an apparent resonance in resistance, strongest for even filling factor transitions.

As depicted in figure 5.9, by going to filling factor $\nu = 8$ in the bulk (constant magnetic field), and reducing the available conducting channels underneath the gate (by adjusting gate voltage), there should be a step like change in the conductance at $\nu = 6$,4 and 2 underneath the gate, corresponding to $^3/_4$, $^1/_2$ and $^1/_4$ of the bulk density. At these values edge state conducting channels in the 2DES leads that have no corresponding state under the gates are strongly back-scattered, and depending on the size of the constriction and the cyclotron radius, are either forced to go through the constriction (as depicted) or are pinched off completely. This can be repeated for other filling factors to build up a picture of number density under the gate vs. applied voltage as in figure 5.8.

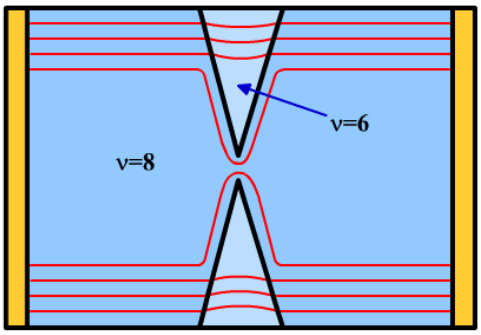

Figure 5.9: Cartoon depicting conducting edge channels (red lines) in the 2DES leads. At a fixed magnetic field, corresponding to $\nu = 8$, the number density under the gate is reduced by application of a negative bias voltage. When the number density at the same field corresponds to $\nu = 6$ there are three edge states left and the remaining state in the leads is strongly back-scattered but can possibly still pass through the gate. As soon as n_s is reduced another conducting channel will be pinched off under the gate.

5.3.1 Magnetoconductance

The experiment utilised two lock-in amplifiers, one to measure the output from the differential capacitance bridge relating to the torque of the magnetometer, and another to measure the longitudinal potential drop between voltage contacts either side of the gate. The current is constant over the measurement range, therefore relates to a resistance measurement. These two measurements are performed simultaneously. Using a quantum Hall effect measurement, and attributing filling factor

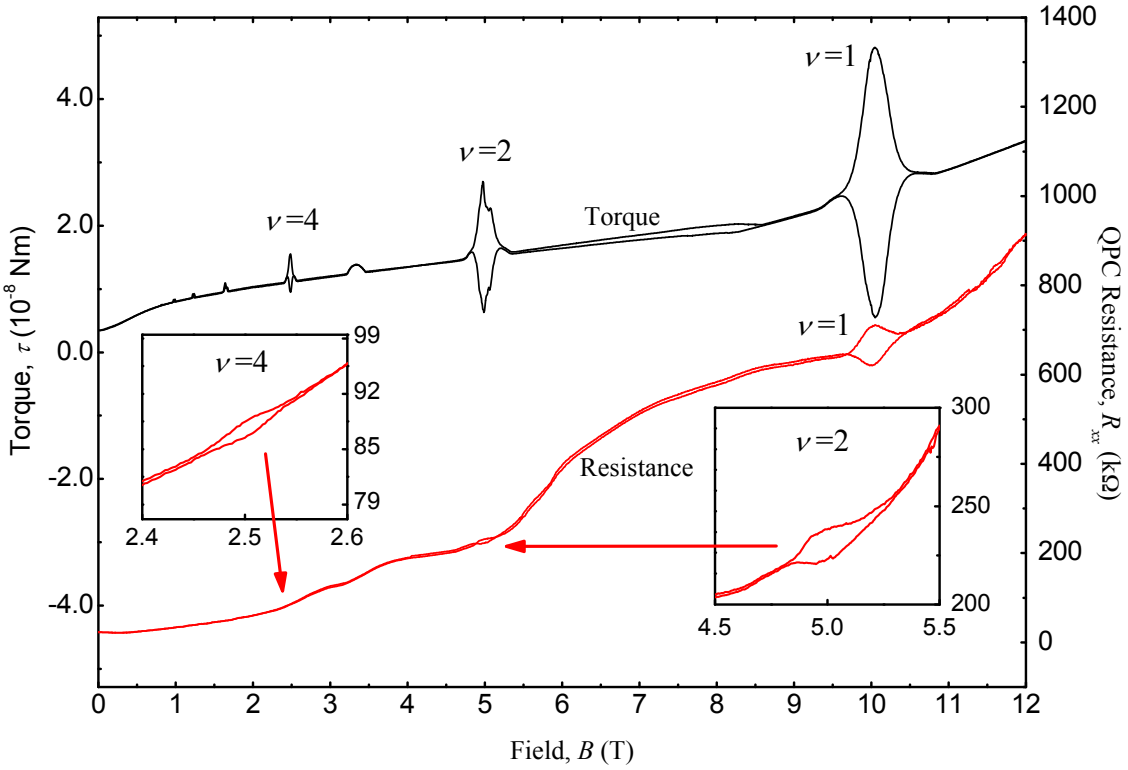

Figure 5.10: Dual measurement of magnetisation and magnetoresistance

field positions at the centres of the resistance minima, the number density of the system was defined to be $2.01 \times 10^{11}\,\mathrm{cm}^{-2}$.

Eddy currents contributing to the magnetisation were resolved for filling factors $\nu = 1, 2, 3, 4, 5, 6$ and 8. Hysteretic features in the magnetoresistance are seen at filling factors $\nu = 1, 2$ and 4, which are the three largest induced currents in the magnetisation. This experiment improved on previous measurements because it was possible to vary the size of the induced current, by inducing a variety of EMFs (sweeping the field at different sweep rates) and hence study the change in the hysteretic magnetoresistance.

A feature at $\nu = 4$ was not seen by Pioro-Ladrière et al., this third hysteretic feature helps to confirm the $1/B$ dependence expected from the QHE.

At higher filling factors the induced currents had a smaller amplitude. Measuring the decay time constants of the induced currents is one way to determine the ρ_{xx} resistivity minima in the QHE, which was considered in chapter 3. The amplitude of

the induced current is linked to the depth of the minima: a deeper minimum is less resistive and so for a fixed EMF has a comparatively larger current. The width of the minima decreases at higher filling factors as the Landau levels are closer together and therefore not only is there less time to induce a current before exiting the low resistance region, but the bottom of the minima may be considered raised if the tails of the Landau levels overlap more.

The ratios of the induced currents from figure 5.10 when converted to a magnetic moment, for $\nu = 1 : 2 : 4$, are approximately $1 : 1 : 1$ and for the magnetoresistance features $46 : 4.3 : 1$. This implies that the total magnetic moments over the area of the sample were the same size, for $\nu = 1, 2$ and 4, but the local charge densities near the edge were decreasing, or the eddy currents were moving into the sample as ν was increased.

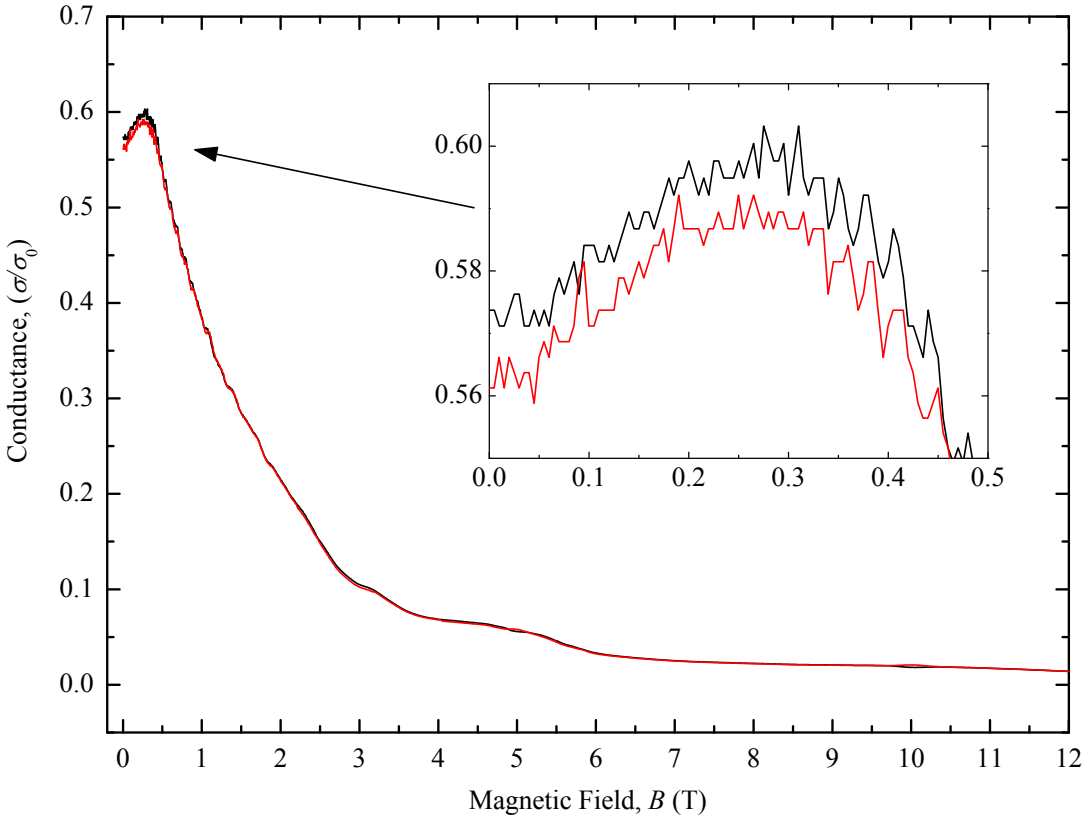

Figure 5.11: Magnetoconductance of the quantum point contact, obtained from figure 5.10, where $\sigma_0 = 2e^2/h$.

The features seen in the magnetoconductance are also interesting. With the gate set to a voltage such that conduction through the QPC is purely by tunnelling ($\sigma < 2e^2/h$), the magnetoconductance behaves as shown in figure 5.11. As the magnetic field increased the conduction through the constriction decreased, i.e. there is a positive magnetoresistance. This can be described qualitatively as the bottom of the saddle shaped potential well being lifted with respect to the reservoir Fermi energy as the number density in the constriction is reduced. A second interesting feature of the magnetoconductance is a negative magnetoresistance below 0.3 T, and is shown magnified as an inset to figure 5.11. This surprising result has been observed previously, and investigated in more detail by van Houten et al. [87] where it was interpreted as a suppression of the geometrical constriction by the magnetic field.

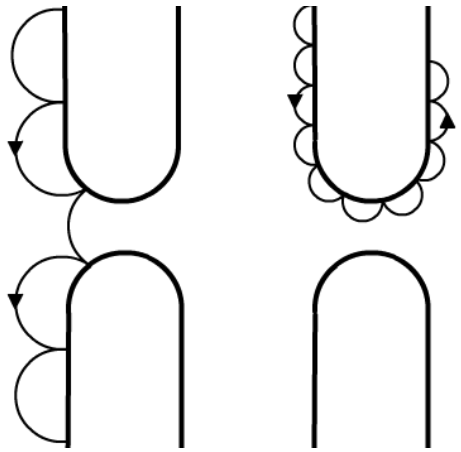

Figure 5.12: Qualitative illustration of the reduction of back-scattering by a magnetic field, responsible for the positive magnetoconductance in the low-field regime in figure 5.11. The electron trajectories approach the constriction without a barrier in a weak magnetic field (left) and a strong magnetic field (right). Image after H. van Houten et al. in ref [40].

Figure 5.12 demonstrates how the conductance of the quantum point contact may increase with B in the low field regime. The skipping orbits of the edge states initially are much larger than the electrostatically defined constriction of the point contact, so although there is a chance that an electron will propagate through, the majority are back-scattered. As the radius of the cyclotron orbits decrease the probability of passing through will increase until the suppression from this effect has disappeared when $2l_{cycl} \leqq W_{constriction}$. The cyclotron radius at the cross over can be estimated

from,

$$l_{cycl} = \frac{\hbar k_{\mathrm{F}}}{eB},$$

and

$$k_{\mathrm{F}} = \left(\frac{4\pi n_s}{g_s g_v}\right)^{1/2},$$

where g_s is the spin degeneracy, g_V the valley degeneracy, the measured number density is $2.01 \times 10^{11}\,\mathrm{cm}^{-2}$, makes $l_{cycl} = 246\,\mathrm{nm}$ at $0.3\,\mathrm{T}$, i.e. half the width of the QPC, however it is expected that the electrostatic width should be smaller than the physical width. In this regime the definition of the gate and the number density of the constriction are essentially unperturbed by the application of a magnetic field. The positive magnetoresistance at higher fields arises from the depopulation of magnetoelectric sub-bands which is a manifestation of the quantum Hall effect. The reduction in back-scattering at high magnetic fields is one of the reasons for the extreme accuracy of the quantum Hall effect, compared with the limited accuracy of quantised conductance in a QPC at zero field.

5.4 Temperature dependence

As temperature is elevated, Landau levels effectively become wider as the Fermi-Dirac distribution is smeared (it is the product of the DOS and the Fermi-Dirac distribution that widens). The QHE resistance plateaux are not as deep and oscillatory phenomena are damped compared to lower temperature experiments. Induced eddy currents are therefore expected to be reduced. In this section we qualitatively observe the change in shape and size of the induced eddy currents as measured previously [68, 67] and discussed in chapter 4, and compare them to the hysteretic magnetoresistance. The T dependence of $\nu = 1$ is shown in figure 5.13, both phenomena appear to evolve in a similar way as temperature is increased; a decrease in amplitude and a hysteresis which occurs over a smaller range of field. Both forms of hysteresis, at all filling factors, have disappeared by $1.6\,\mathrm{K}$, with the exception of the magnetic moment of $\nu = 2$ which is reduced but still measureable.

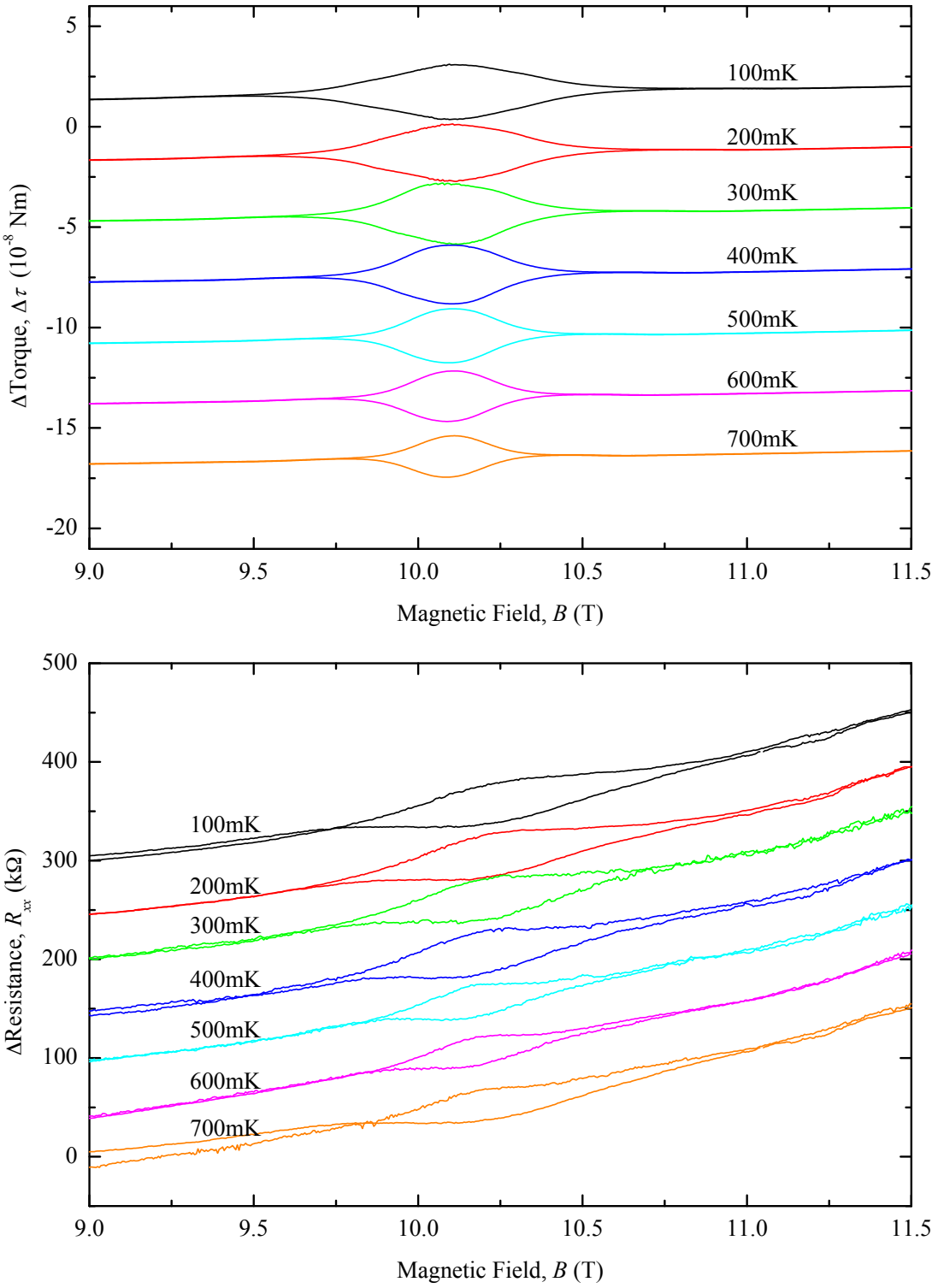

Figure 5.13: Observation of elevating the temperature on the shape and size of the induced current and the hysteretic magnetoresistance with a changing magnetic field at a sweep rate of $62\,\mathrm{mT\,s^{-1}}$. Features at $\nu = 1$ are suppressed as temperature is increased, both experiments follow a similar trend.

The same dependence is difficult to resolve for filling factors $\nu = 2$ and 4, due to the reduced size of the magnetoresistance peaks. The magnetisation and magnetoresistance traces for $\nu = 2$ are not in good agreement, we attribute this to an increased noise on the magnetoresistance traces in this instance. The magnetisation and magnetoresistance traces are measured simultaneously at a sweep rate of $62\,\mathrm{mT\,s^{-1}}$. The peak to peak difference is measured and plotted in figure 5.14, along with that of $\nu = 2$.

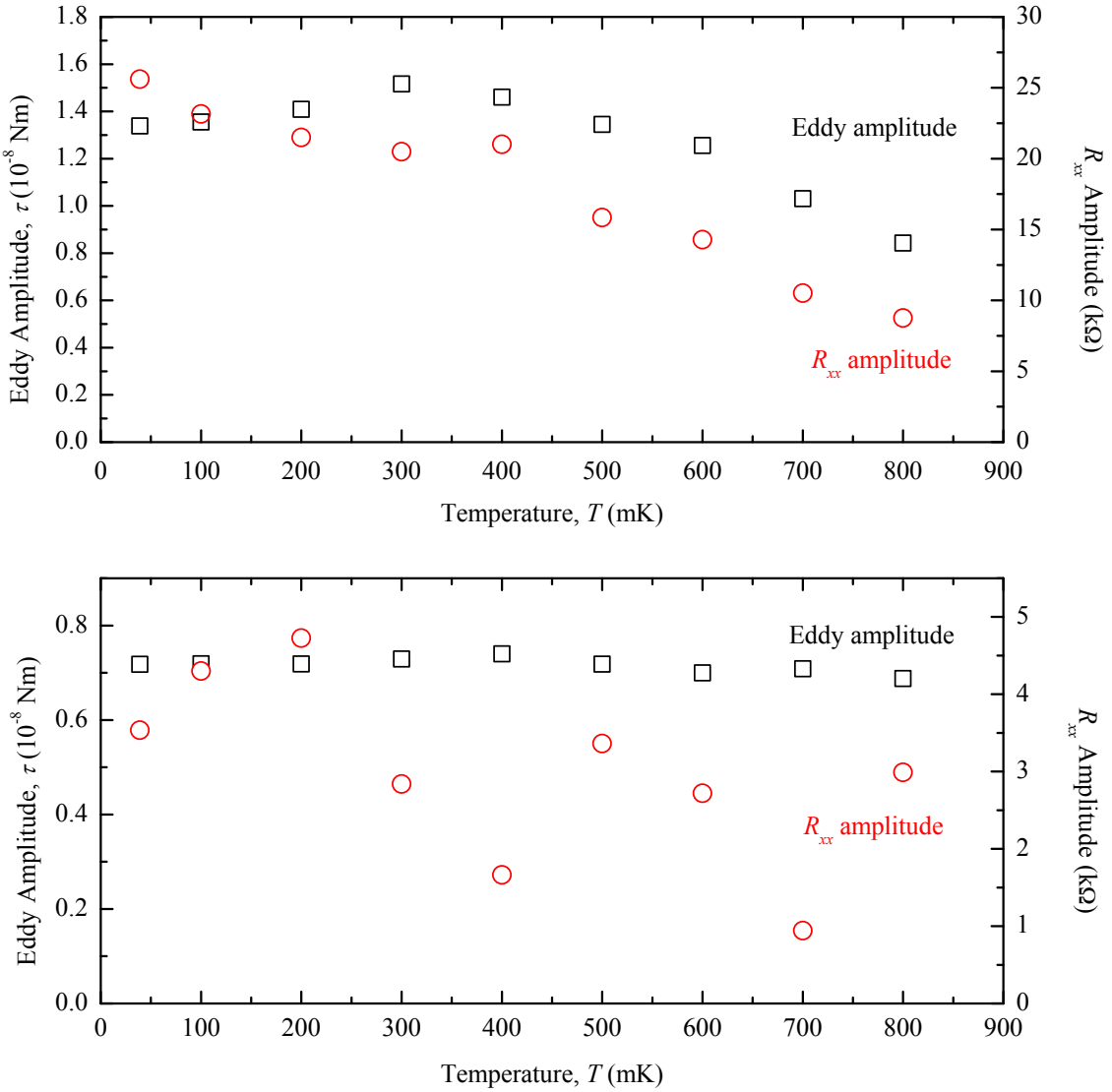

Figure 5.14: Temperature dependences of induced eddy currents at $\nu = 1$ (top) and $\nu = 2$ (bottom), with corresponding hysteretic magnetoresistances. $\nu = 1$ shows a very similar trend for both experiments, but the QPC intercepts the zero at a lower temperature. At $\nu = 2$ the QPC data suffered from noise, possibly due to trapping charges under or near the gates in the QPCs recent history, however it is clear the magnetisation shows no temperature dependence.

There is agreement between the two experiments; on increasing the temperature, the temperature dependences for the induced currents and the QPC resistance both decrease for the $\nu = 1$ filling factor. The $\nu = 2$ dependence is different from the other filling factors at temperatures below 800 mK. The next question is, at a constant temperature can the size of the magnetoresistance hysteresis be reduced when the

size of the induced current is changed?

5.5 Sweep rate dependence

The sample mobility is relatively high for a GaAs/(Al,Ga)As system, and a saturation in the eddy current IV characteristic is measured, i.e above a certain sweep rate the size of the induced current does not increase. The eddy currents are much easier to resolve than the QPC resistance features, and the structure of the IV curves are looked at in more detail in chapter 4. At low temperatures, where the QPC magnetoresistance was strongest the eddy currents never left a saturated regime for filling factors 1 and 2. For filling factor 4, upon reducing the sweep rate below $1\,\mathrm{mT\,s^{-1}}$ the induced current left the saturated regime, and a corresponding reduction in the magnetoresistance hysteresis was seen, as in figure 5.15.

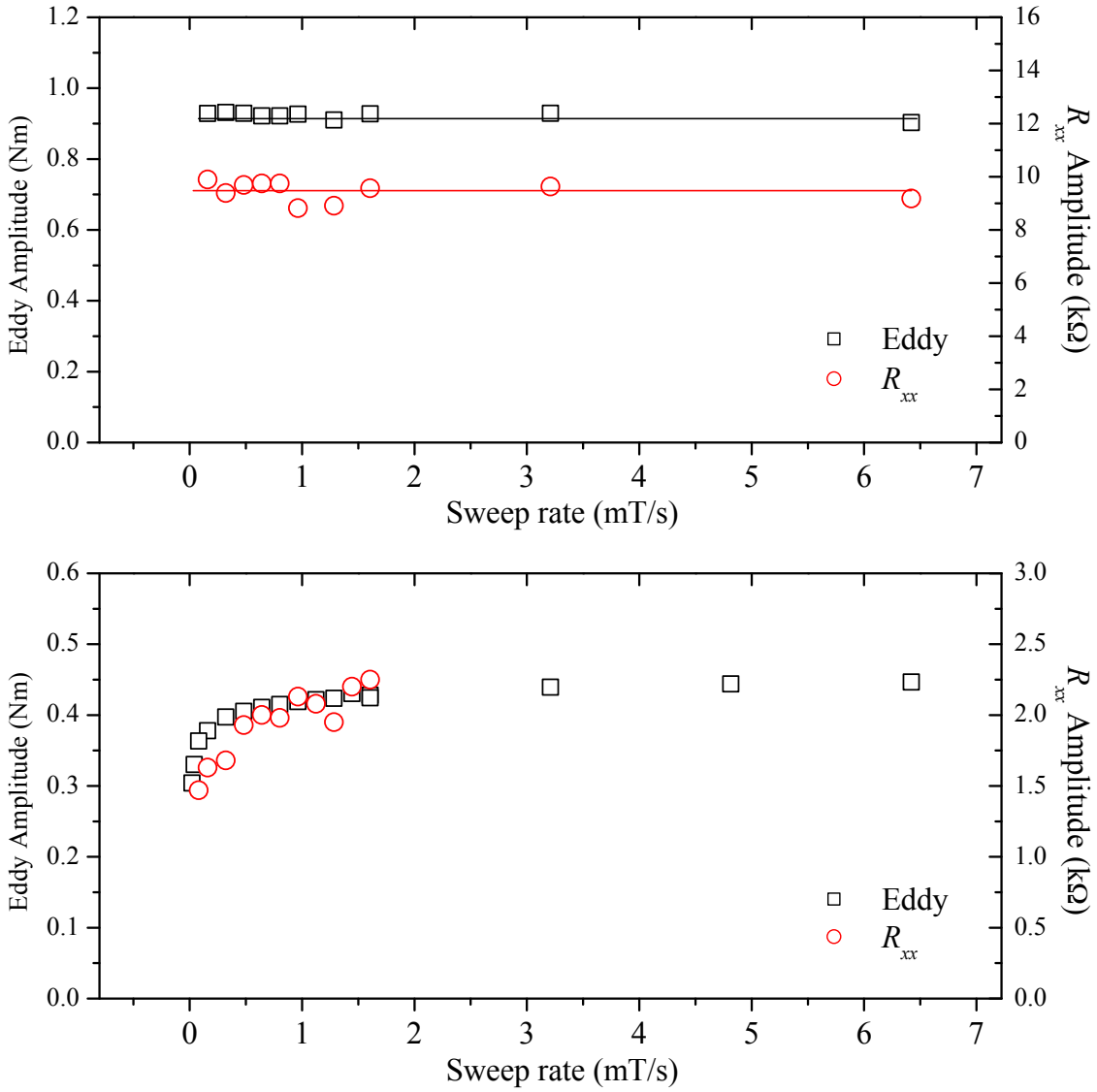

Figure 5.15: Sweep rate dependences of $\nu = 2$ (top), $\nu = 4$ (bottom) at 100 mK measured simultaneously. It was not possible to reduce the sweep rate enough to leave the saturated regime for $\nu = 2$ due to experimental constraints. The eddy current size is varied and the magnetoresistance was found to mirror the size of the induced current.

5.6 Decay measurements

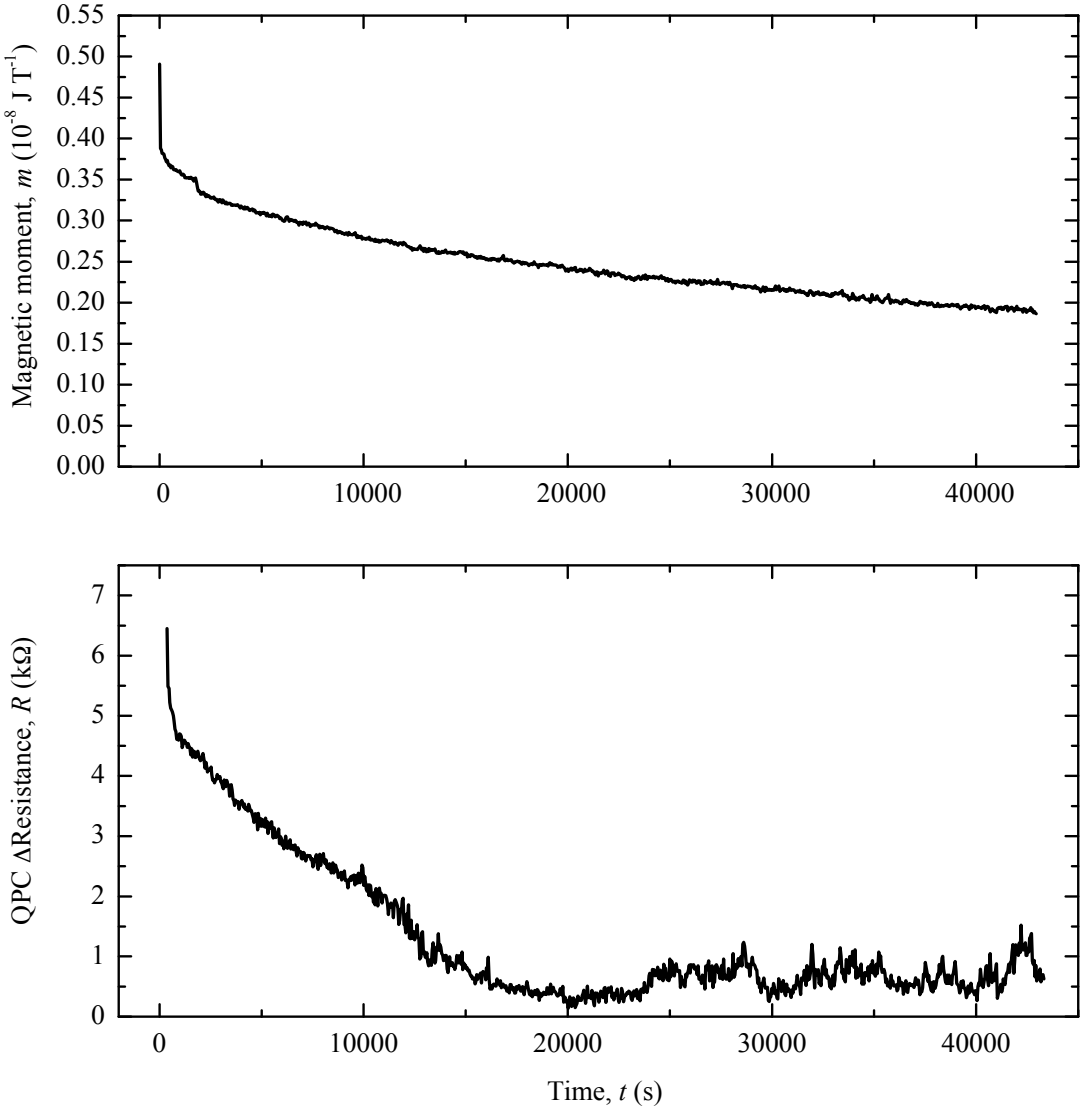

Figure 5.16: Simultaneous measurement of an induced current decay, and the decay of the magnetoresistance for $\nu = 2$ at 300 mK.

The magnetoresistance decay was measured simultaneously with the decay of the eddy current. The decays were measured for $\nu = 1$ at 100 mK, and the magnetoresistance decay (but not magnitude) was smaller than the temperature drift, so the only thing that could be concluded was that the magnetoresistance decay was persistent to within 10% of the initial eddy current. Figure 5.16 shows the simultaneous decays for $\nu = 2$ at 300 mK. The same method to establish the effective 'zero-point' of the

decay as in chapter 4 was applied to the magnetoresistance decay. The effective zero has not been measured previously, but by doing it, a true comparison can be made between the two experiments.

The two decays both have two regimes, a fast decay of seconds and a much longer decay of $> 10,000$ seconds. In both experiments the fast decay is a similar proportion of the total decay $\sim 14 \pm 2\%$. There is a however a disparity between the two decays, the magnetisation decay is much longer than the magnetoresistance. The QPC only detects local perturbations, as discussed earlier on, so this experiment demonstrates that the eddy current must be moving away from the edge as it decays.

There was a drift in temperature which is responsible for the behaviour in the magnetoresistance at times $> 20,000$ seconds. This drift means that there is an error in establishing the zero, of $\sim 10\%$ again, as it will have moved during the course of the experiment.

5.7 Correlation of structure in 'noisy' breakdown of the QHE

As illustrated in the previous section, we can routinely access a regime where the quantum Hall effect breaks down. Elliott et al. [76] looked into the breakdown of the QHE around integer filling factors using torque magnetometry in more detail. They observed a strong 'noisy' behaviour of the induced current around filling factor $\nu = 2$. The noise was observed to have a structure, and was explained by attributing a radial Hall field to the current, which would result in a build up of charge around the sample edge. The breakdown would occur at random "weak" points with a high local Hall field, around impurities and imperfections. In these regions the Hall field reaches a critical value and causes an avalanche of charge distribution which is re-distributed to the bulk. Figure 5.17 shows an increased noise structure around the centre of the peaks compared to non-integer filling

factor field regions. There is clearly three large 'noise' events, as indicated with arrows, which are evident in both measurements.

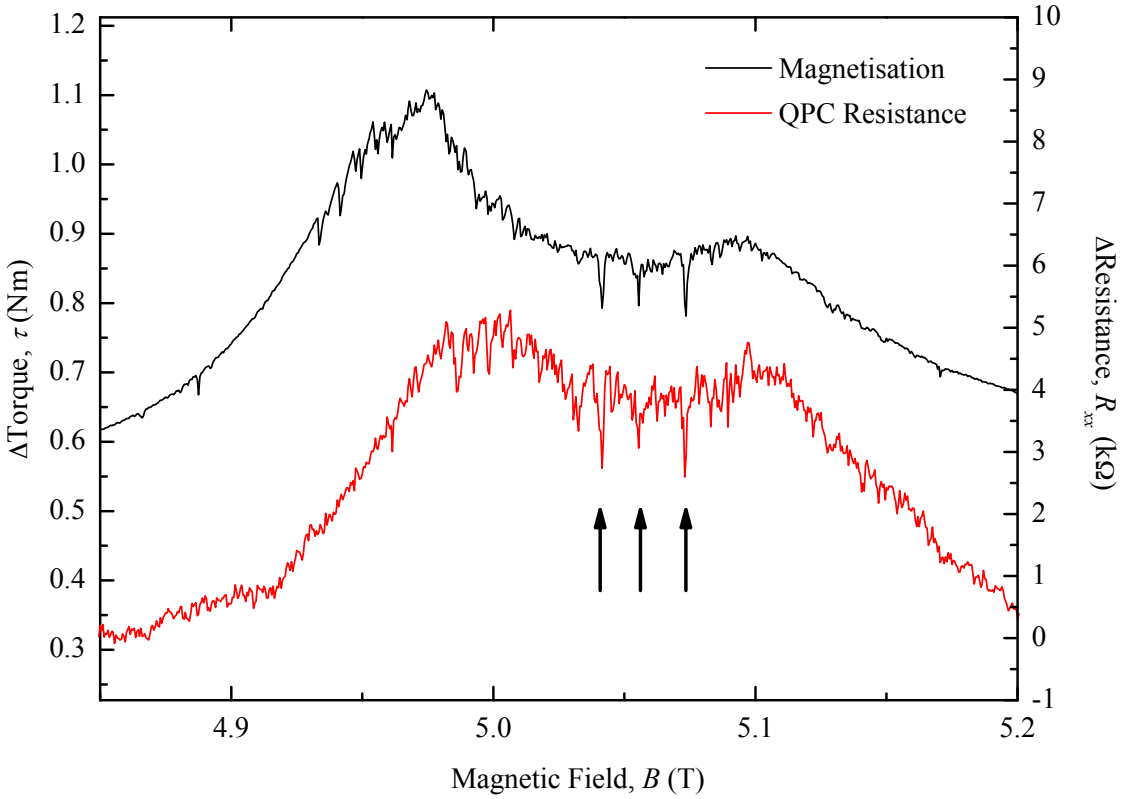

Figure 5.17: $\nu = 2$ at 100 mK is observed to have a noise structure similar to that seen in Elliott et al. [76]. The noise is attributed to the breakdown of the QHE; three individual breakdown events are correlated in the simultaneous measurements, magnetisation (black, top) and magnetoresistance (red, bottom).

As the explanation offered by Elliott et al. [76] implies the eddy current and the breakdown happen at the edges, the measurement of resistance of a quantum point contact is a useful test of this theory. Sample AK47 yielded large hysteretic features which had a similar temperature dependence and an almost identical sweep rate dependence to the same systematic change. By using a short lock-in-amplifier time constant of 10 ms, the individual breakdown events in both

magnetic moment and magnetoresistance were measured, and similarities in the structure of the noise in both were measured. This correlation of individual breakdown events requires a simultaneous measurement, and is another strong piece of evidence that the hysteresis in the QPC resistance must be due to induced eddy currents. As the hysteresis is seen to weaken more strongly for lower field filling factors, it can be concluded that the gate is only sensitive to local perturbations in potential. These individual breakdown events therefore must be occurring at the edge of the sample.

The magnetic moment around filling factor $\nu = 2$ in figure 5.17, has a double peak structure at low temperatures. One possible explanation is that the sample is non-homogeneous and is made up essentially of two electron systems with similar but different number densities, however this does not explain its occurrence only at $\nu = 2$. Regardless of the origins, the double peak structure of the eddy current only seen for $\nu = 2$ is reflected in the structure of the magnetoresistance for the same filling factor, and only that filling factor.

5.8 Affect of the gate on the induced current

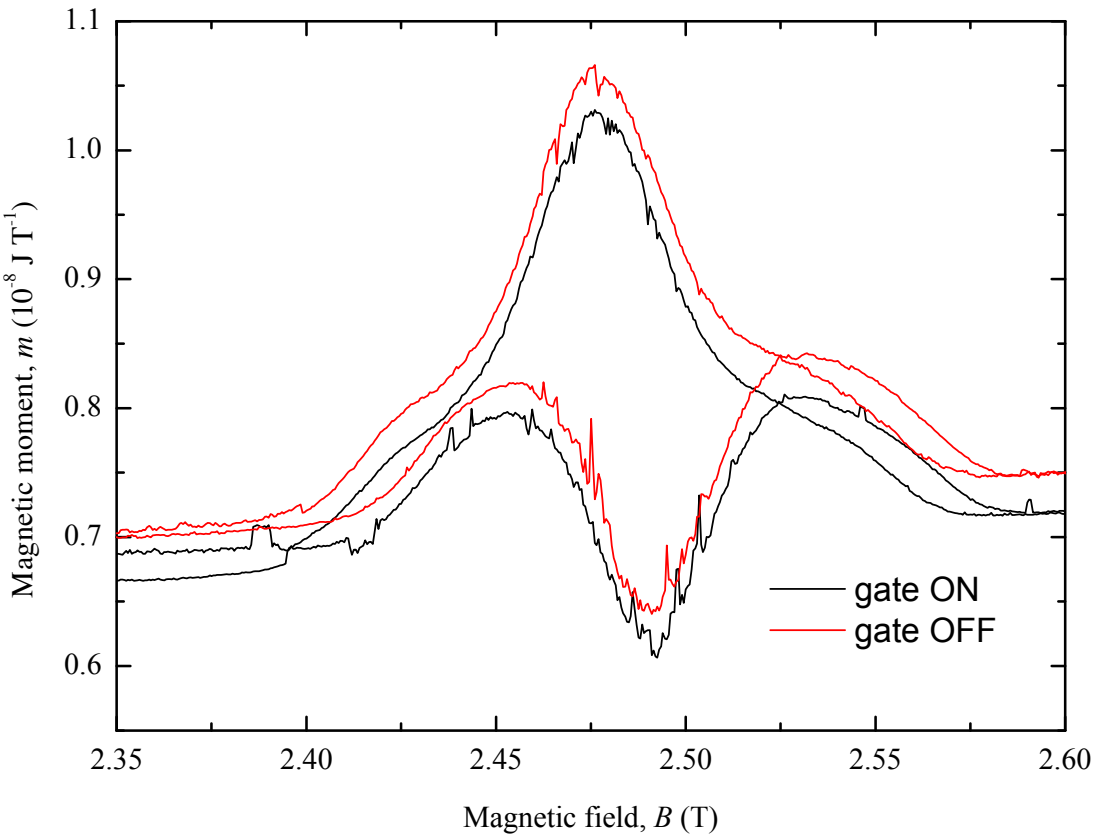

Figure 5.18: Induced eddy current at $\nu = 4$ at 300 mK, and a sweep rate of 21 μT s^{-1}, for two different states: the gate OFF and the gate ON (sample divided into two).

So far this chapter has concentrated on the affect of the induced current on the properties of the QPC. An attempt was made to perturb the induced current by activating/ de-activating the gate. By applying a bias voltage to the gate, the 2DES has two configurations: one large conducting area, or two smaller conducting areas. The EMF is proportional to the area of the sample by the approximation,

$$E = -\sqrt{\frac{A}{4\pi}}.\frac{dB}{dt}, \tag{5.2}$$

so by changing the geometry of the experiment it should have been possible to change the size of the induced current. Several attempts were made, at different temperatures and sweep rates, but the most extreme sweep rate and temperature

were chosen to be in the range far away from a saturation current, 300 mK at a sweep rate of $21\,\mu\mathrm{T\,s^{-1}}$, and the result is shown in figure 5.18. The gate was established to be 'off' when it was set to a bias voltage corresponding to it's zero. The gate was confirmed to be off with a measurement of ρ_{xx}. To within 5% it was not possible to affect the magnitude of the induced current with the gate.

With the induced current established, at a static field, the decay was measured while switching the gate on/off. The idea was the induce dissipation in the induced current by forcing opposite edges together as the gate was closed. Experiments ranged from 1 switching event per hour for 10 hours, to several switching events per second, and it was not possible to affect the induced current to within the noise limit of the magnetisation measurement.

5.9 Conclusions

The hysteresis in the magnetoresistance of a quantum point contact was investigated, through a simultaneous transport and magnetometry measurement. Induced currents corresponding to filling factors up to $\nu = 8$ were measured. Three corresponding features were measured in the magnetoresistance of a QPC.

The temperature dependence was measured simultaneously, and for LL filling factor $\nu = 1$, the general shape of the curves was in agreement. LL filling factor $\nu = 2$ was not in good agreement, although the data suffered from a poor signal to noise ratio, owing to the size of the magnetoresistance, and to jumps in the resistance arising from trapped charges relocating from under the gate. The later problem was solved by waiting at a fixed gate voltage for several days.

The sweep rate IV characteristics of the the two experiments were similar. The $\nu = 2$ sweep rate curves saturated over the entire range for both experiments. At 100 mK, it was possible to resolve the magnetoresistance feature at $\nu = 4$. The low sweep rate regime was investigated, and both the induced currents and the hysteretic magnetoresistance were reduced at low sweep rates.

Sweeping the magnetic field B to a fixed field position and waiting, demonstrated that both phenomena decay with time. Both decays were characterised by a fast decay of seconds and a slow decays of $> 10,000$ seconds. By sweeping up and down over the field range of interest before the decay, an effective zero was found for the magnetoresistance, and a more enlightening comparison could be made. The magnetoresistance decayed to it's effective zero faster than the induced current. As the QPC only detects local electrostatic perturbations, it can be concluded that the eddy current is decaying away from the edge, as well as decreasing in magnitude.

An attempt was made to affect the induced eddy current by switching the gate on/off. A change in the geometry of the sample should have resulted in a reduced magnetic moment, but no change was observed to within 5%. Switching the gate on/off during a decay, even at high frequencies, did not induce any extra dissipation of the induced current. The induced currents would have flowed so as to avoid any impurities, and perhaps the area under the gate, even when switched off, created a barrier.

Experiments in the fast timescale, 10 ms, resolved structure in the induced currents that has previously been attributed to the breakdown of the quantum Hall effect. Both the QPC resistance and the induced current had a larger signal to noise ratio in the fast regime near exact filling factors. By performing a simultaneous measurement, individual breakdown events were seen and correlated, which is one more argument for the induced current causing the perturbation to the QPC gate.

Chapter 6

Dual Calorimetry/Magnetisation Measurements of 2DES

6.1 Introduction

The zero-resistance state of ρ_{xx} in the quantum Hall effect has been investigated previous chapters by torque magnetometry, and electrostatic perturbation of a quantum point contact. The minimum resistivity ρ_{xx} was estimated from the critical magnetic moments at low temperatures, at different integer filling factors. The effects of Landau level broadening were evident in the experiments discussed so far, but the exact shape of the broadened levels is still a topic debate in the literature. The equilibrium measurement of torque magnetometry measures the oscillating magnetic moment as a function of field, the de-Haas–van-Alphen effect (dHvA), which probes the entire DOS, not just the extended states, and therefore depends on the broadening of the LL's. Other equilibrium thermodynamic properties of the system will also depend on the form of the DOS.

This chapter begins by reviewing previous work and summarises the current consensus. A novel device is then proposed, a dual cantilever-calorimeter. The design is investigated and shown to be viable. The cantilever-magnetometer/ calorimeter

is again a GaAs/(Al,Ga)As quantum well structure, but based on lower mobility samples than earlier chapters, and to be operated in a regime where eddy currents are not present, so that the dHvA signal is not masked, which has been achieved previously by illuminating the sample. First the cantilever design is presented, and the processing and measurement of a $10\,\mu m$ device is described. The data exhibited $1/B$ oscillatory behaviour typical of a quantum Hall system, but the non-reversing features have not been completely explained. Next, the experimental components for a calorimetry experiment are considered. Low temperature thermometers, grown as 10 bilayers of Au/Ge, were investigated at different concentrations. They were reliably produced, and functioned at low temperatures in high magnetic fields.

6.2 Cantilever viability

6.2.1 Previous measurements

A GaAs micromechanical cantilever magnetometer with an integrated 2DES was developed by Schwarz et al. [5]. The cantilever had a mesa with a 2DES, of dimensions $2\,\mathrm{mm} \times 2\,\mathrm{mm}$, $n_\mathrm{s} = 2.3 \times 10^{11}\,\mathrm{cm}^{-2}$ and a mobility of $0.6 \times 10^6\,\mathrm{cm\,V^{-1}\,s^{-1}}$, at the end of a beam that was defined by lithography. This was wet-etched up to a molecular-beam epitaxy (MBE) etch stop, to produce a cantilever of only $10\,\mu\mathrm{m}$ thickness. Little additional mounting was required for a cantilever magnetometer, and because the GaAs had been thinned by etching, the background magnetisation was reduced. A layer of gold was deposited on the back, and through capacitive detection, the authors established the sensitivity of the structure to be $10^{-13}\,\mathrm{J\,T^{-1}}$.

Harris et al. [88] fabricated a device with a significantly smaller mesa, $100\,\mu\mathrm{m} \times 40\,\mu\mathrm{m}$, incorporated into a cantilever $50\,\mu\mathrm{m}$ wide, $320\,\mu\mathrm{m}$ long and $0.1\,\mu\mathrm{m}$ thick. The cantilever was driven at resonance by a piezoelectric crystal and its displacement was measured with a fibre optic interferometer. The magnetic moment of the 2DES contributed a restoring torque, which shifted the resonant frequency as the magnetic field varied. The reduced dimensions of the 2DES in this device reduced

the size of the induced currents, which can potentially mask the dHvA signal. The magnetic moment sensitivity was $< 10^{-16}\,\mathrm{J\,T^{-1}}$, similar to a interferometry cantilever experiment by Ruhe et al. [89], and Springborn et al. [90], the latter achieving a sensitivity of $5 \times 10^{-16}\,\mathrm{J\,T^{-1}}$.

6.2.2 Experiment details

The deflection of a cantilever for a given force is inversely proportional to its thickness cubed, therefore by making a thinner substrate the device is made more sensitive. A thinner cantilever will also be beneficial to a calorimetry measurement. As previous workers have successfully produced cantilevers of $10\,\mu$m thickness, but without all the extra processing a calorimeter would require, this was considered a good starting point. The cantilever is $3\,\mathrm{mm} \times 6\,\mathrm{mm}$ and surrounded by a frame, and for an area this large, a thickness of $5\,\mu$m was the aim limited by variations in the initial thickness of the cantilever, as large as $\sim 1\,\mu$m. The processing of such a device is considerably easier than the Exeter cantilever-calorimeter described later.

The cantilever under investigation is a single layer GaAs/(Al,Ga)As quantum well structure grown at Cambridge, and processed by Dr Geoff Hill at Sheffield. As the cantilever was not processed at Exeter, it needed to be robust enough to travel from Sheffield to Exeter (253 miles) safely. The last step, the back etch, which formed the cantilever, required the device to be fixed to a glass microscope slide with photoresist and wax. In this state it was robust enough to be transported, and released from the packaging at Exeter in a clean room.

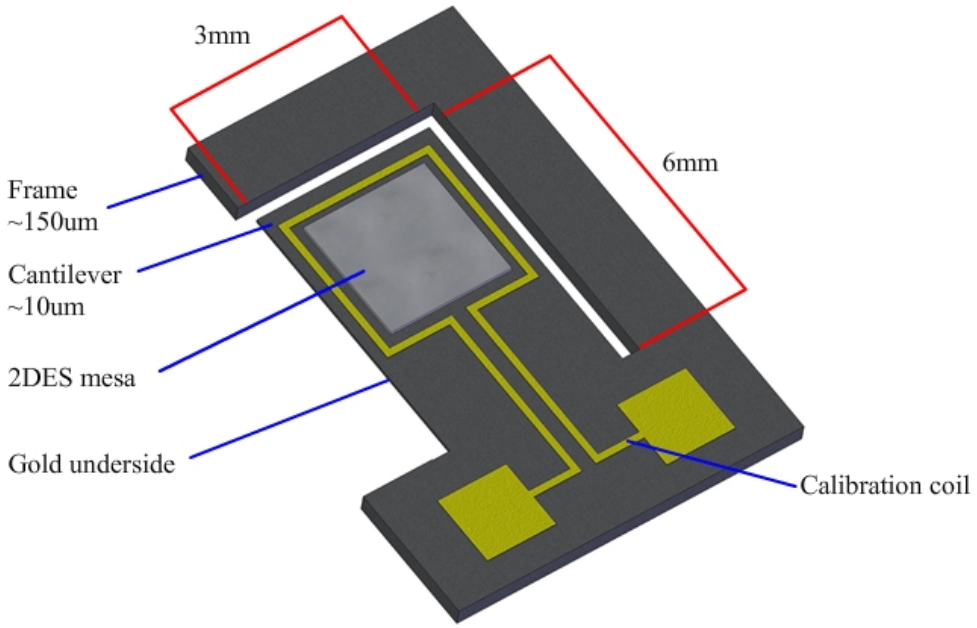

Figure 6.1: Cantilever T621 to scale. The GaAs cantilever is etched to thickness of 10 μm.

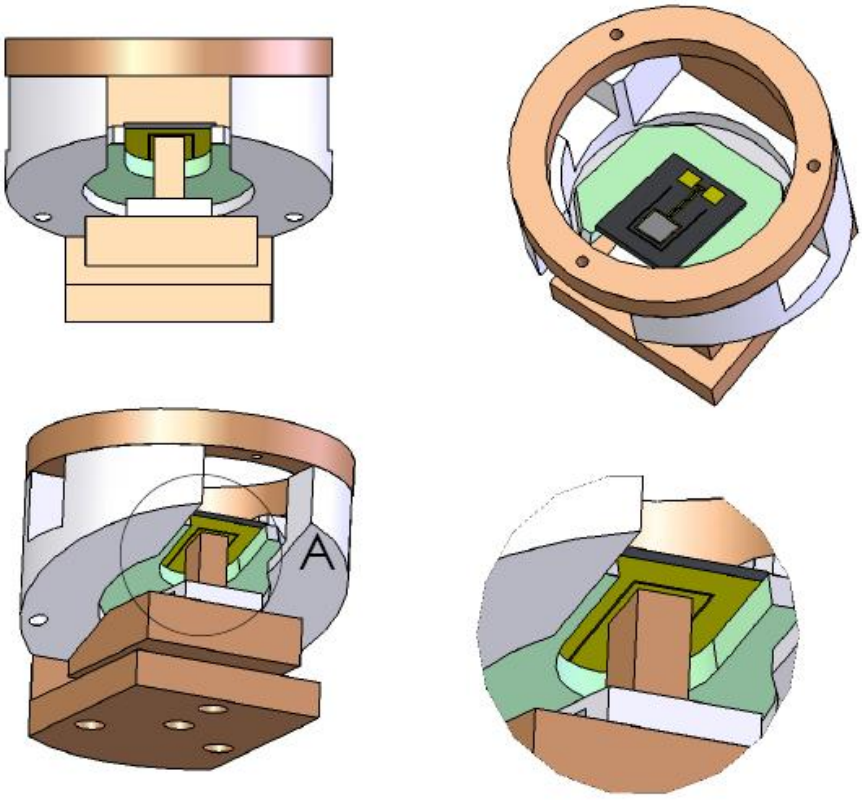

Figure 6.2: Mounting arrangement for cantilever T621 in the mixing chamber of 3He/4He dilution refrigerator. The back of the cantilever is covered with a thin layer of gold; this and the phosphor-bronze pillar form a capacitor.

A new mounting, depicted in figure 6.2, to incorporate the cantilever into a Leiden Cryogenics dilution refrigerator was manufactured in the mechanical workshop at Exeter by Mr Kevyn White. The arrangement was fitted into the mixing chamber of the refrigerator, but later calorimeter-cantilevers were fitted on a cold finger. Details of the refrigerator wiring are given in chapter 3.

The frame of the cantilever measured 12 mm × 8 mm, and was fixed onto a Stycast [42] mounting plate with a small quantity of GE varnish [43] ($\sim 1\,\mathrm{mm}^3$) on two opposite corners. The mounting plate was then varnished into position on the Stycast mounting cap (figure 6.2). The purpose of the stycast was to electrically insulate the underside of the cantilever from the rest of the system, which was coated in gold. To make electrical contact, the cantilever half of the capacitor had previously been fitted with ~ 5 cm of insulated copper wire(insulated, 0.2 mm diameter) with silver-

loaded paint [45], which was then soldered to the refrigerator wiring loom when it was fitted into the plastic mixing chamber.

The cantilever was bolted and wired to the refrigerator, and then the stator capacitor plate was fitted. The drying time of the varnish gave several minutes in which the position of the cantilever could be adjusted. Using a centrally fixed screw which adjusted the height, three other screws set the pitch of the stator capacitance pillar. The capacitor was adjusted by eye, aiming for the two sides of the plates to be parallel, while monitoring with a capacitance bridge [91] at the same time. There is potential for improvement, as over these distances cryogenic piezo-electric positioners could be used for fine adjustment of plate separation [6]. The cantilever was free to bend under the influence of the applied magnetic field which induced a magnetic moment of varying strength. The corresponding capacitance change was measured by either a commercial capacitance bridge [91], or a differential capacitance bridge [6] used with a reference capacitor at room temperature.

6.2.3 Preliminary Cantilever data

The capacitor plates were set parallel at room temperature, with the dilution unit clamped in a vertical position. The capacitance at room temperature was 0.9718 pF, which upon cool-down to 75 mK increased to 1.126 pF. The device responsivity was measured to be $0.52 \times 10^5\,\mathrm{V\,N^{-1}m^{-1}}$, approximately an order of magnitude less than a conventional rotor magnetometer. To increase this value the plates would need to be closer. The limiting factor in getting the plates close was the quality of the cantilever of T621, which had a surface roughness with features $\sim 20\,\mu m$ in height. The plates had to be arranged such that these features would not touch upon cool down. The roughness was probably due to an 'unfortunate' etch, the etchant was improved for later devices.

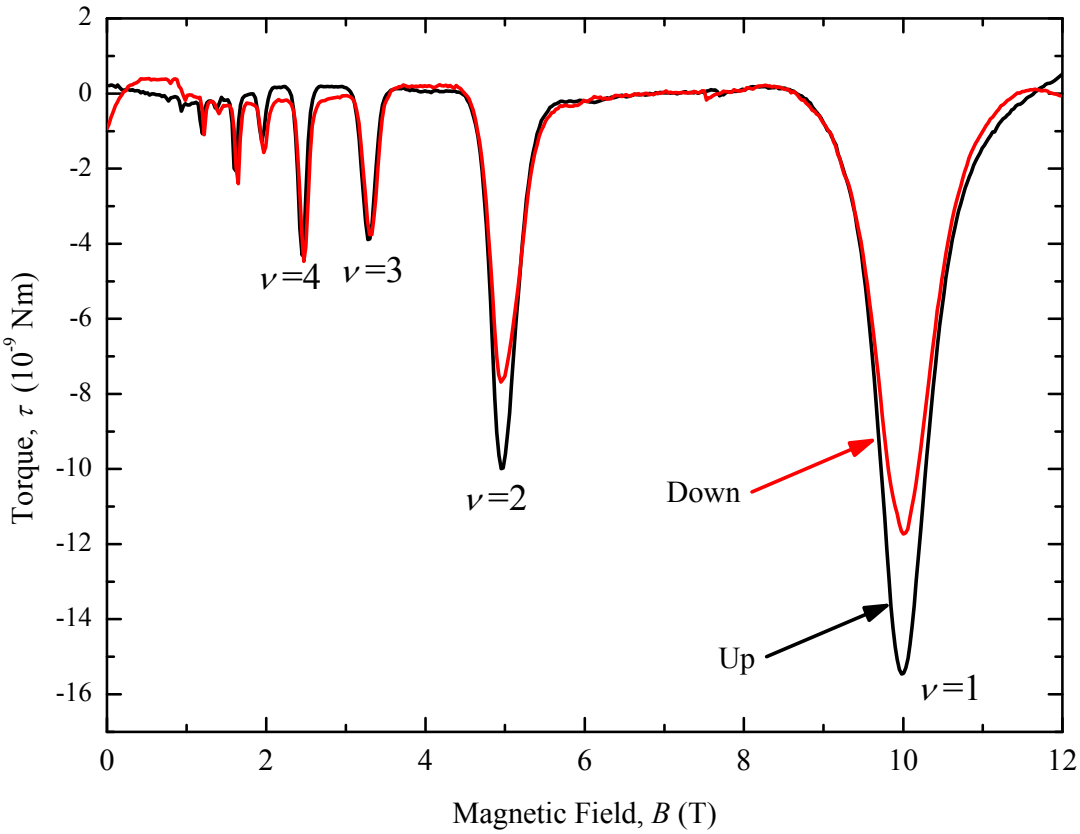

Figure 6.3: Magnetisation data for cantilever T621 at 75 mK, at a magnetic field sweep rate of 3.33 mT s^{-1}. Features correspond to Landau level filling factors, and probably arise from capacitive coupling to the 2DES as they are non-reversing. Hysteresis is seen at $\nu = 1$ and $\nu = 2$, attributed to induced eddy currents.

Figure 6.3 shows an up and a down sweep at a temperature of 75 mK, and a magnetic field sweep rate of 3.33 mT/s for cantilever T621. A small temperature drift has been removed from the plot, $< 10\%$ of the signal, which probably contained a small background magnetisation signal. This background makes up a less smaller proportion of the total signal compared to the background from the magnetisation of AK47 in chapter 3 for example, which was $\sim 50\%$ of the size of the largest induced current. Features were seen which correspond to integer filling factors, but had the appearance of non-reversing induced currents, for which no physical explanation currently exists. dHvA oscillations were expected, but the shape of the trace did not resemble that expected for the oscillatory magnetisation. A more likely explanation

is that the large troughs were due to the stator plate, or the gold on the underside of the cantilever itself, capacitively coupled to the 2DES.

The second notable feature in the traces was a hysteresis between an up and a down magnetic field sweep, measured at $\nu = 1$ and $\nu = 2$, probably due to induced eddy currents. The number density was calculated to be $2.4 \times 10^{11}\,\mathrm{cm}^{-2}$.

For a cantilever of $10\,\mu$m, the calculated heat capacity is $C_V = 1.57 \times 10^{-13}\,\mathrm{J\,K}^{-1}$ at 100 mK. This is comparable to the much thinner gold underside, assuming a thickness of 100 nm, of $C_{el} \sim 4.01 \times 10^{-14}\,\mathrm{J\,K}^{-1}$, assuming the phonon heat capacity of gold to be small in comparison.

6.3 Calorimetry

On cooling from room temperature to liquid helium temperature the specific heat capacity of a typical solid decreases by three or four orders of magnitude, tending to zero as $T \to 0\,\mathrm{K}$. The small heat capacities at liquid helium temperatures and below are difficult to measure. Careful consideration is needed about how a temperature is measured, and adequate thermal isolation, with regard to heat exchange with surroundings and the error in determining the heat capacity of a sample. There are essentially two contributions to the heat capacity signal in a 2DES calorimetry experiment; the electronic contribution of the 2DES, and the contribution from the bulk semiconductor plus the rest of the addenda. Below the Debye temperature θ_D, the addenda phonon heat capacity will obey the Debye T^3 law,

$$C_V = \left(\frac{12\pi^4 N k_\mathrm{B}}{5}\right)\left(\frac{T}{\theta_\mathrm{D}}\right)^3, \tag{6.1}$$

where a crystal has N lattice points. This predicts that the lattice heat capacity is a universal function scaling for all solids through the parameter θ_D, given by

$$\theta_\mathrm{D} = \frac{\hbar}{k_\mathrm{B}}\left(6\pi^2 v_\mathrm{w}^2 \frac{N}{V}\right)^{1/3}, \tag{6.2}$$

where the group velocity and phase velocity are both taken as equal to the velocity of elastic waves in the medium v_{w}. There will also be a 3D electronic contribution to the addenda heat capacity from the gold components, given by,

$$C_{\mathrm{el}} = \pi^2 N k_B \frac{T}{T_{\mathrm{F}}} = \gamma T \tag{6.3}$$

where γ is the Sommerfield constant, where $\gamma = 0.689$ for 3D gold. The contribution from the 2DES in its simplest form, discussed in chapter 2 scales linearly with T,

$$C_{el} = \frac{\pi^2}{3} k_{\mathrm{B}}^2 T D(E), \tag{6.4}$$

where $D(E)$ is the density of states. The addenda having a large mass will have a comparatively large signal compared to the electronic contribution. Because the two contributions scale differently, the electronic of the 2DES contribution becomes significant at low temperatures, and measureable. It is in this regime that the calorimeter needs to be optimised.

6.3.1 The Dual Cantilever-Calorimeter

Heat capacity or magnetisation measurements of the same electron system in different cool downs can vary. For example if the sample is cooled down faster in one instance then it is possible one area of the sample may cool faster than another and the resultant electron system will be inhomogeneous. Comparisons between different experimental techniques applied to different 2DES on different cool downs, combine a lot of subtle differences, so a direct comparison is difficult. By measuring the heat capacity and the magnetisation of the same system during the same cool down, perhaps even simultaneously, a lot of systematic errors can be eliminated. The proposed device in shown in figure 6.4.

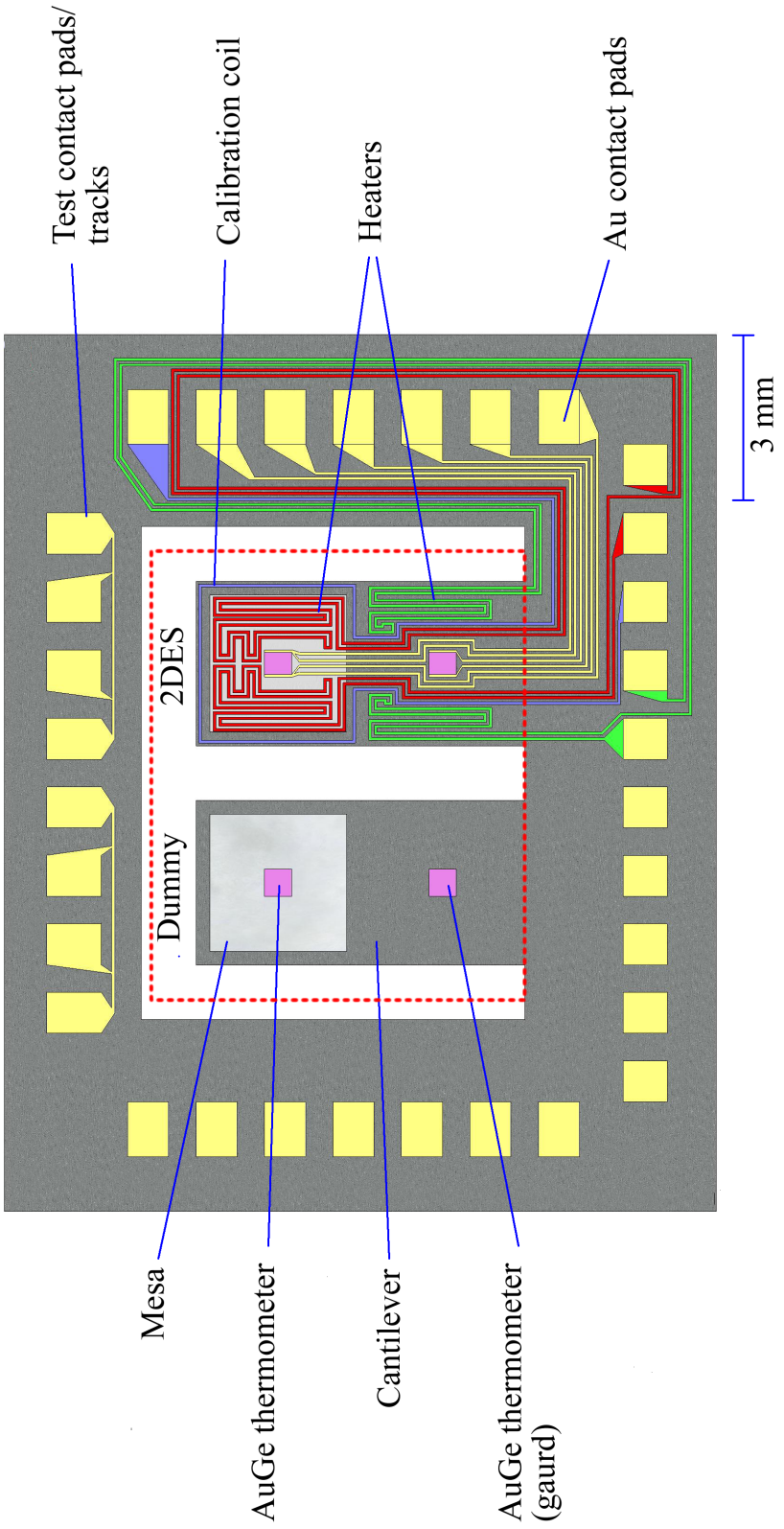

Figure 6.4: The Exeter cantilever-calorimeter. The device has two identical cantilevers (only one is shown to have wires for clarity), except that one has a 2DES mesa, and the other has the 2DES removed. All tracks on the cantilever are 50 μm wide, except heaters on the 2DES (62.5 μm wide), and 5 nm to 50 nm thick. Tracks outside the dotted red region are gold contact leads $\sim$ 200 nm thick.

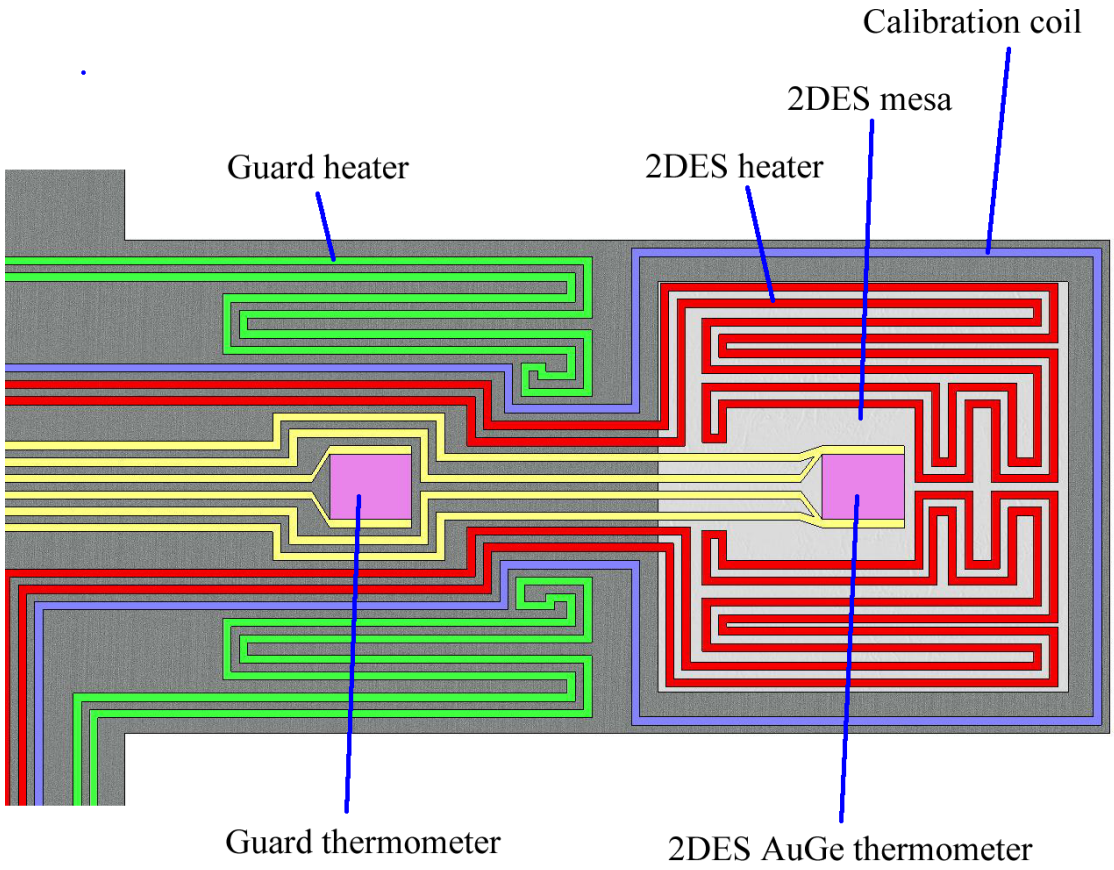

Figure 6.5: The Exeter cantilever-calorimeter. An enlarged version of the 2DES cantilever from figure 6.4. Heater tracks on the mesa are 62.5 μm wide, all other tracks are 50 μm. The guard heater and thermometercreate an artificial thermal isolation for the 2DES in a heat capacity measurement.

The Exeter cantilever-calorimeter incorporated the two measurement techniques, magnetisation and heat capacity, onto one device. The cantilever has the potential to be more sensitive than the conventional torque magnetometry with a rotor. The calorimetry experiment also has potential to be a better probe of heat capacity compared to previous work, because:

1. 5 μm cantilever if realised is thinner than previously used.
2. Thermometer with a smaller heat capacity than previously used.
3. Guard heater/ thermometer technique.
4. Differential calorimetry with a dummy.

The first two issues are discussed experimentally in this chapter. The second two were not tested in this investigation. The idea of the guard heater is to create an artificial thermal isolation for the 2DES. Heating is applied to the guard to maintain its temperature close to that of the 2DES, hence the heat leak can be made close to zero, as the thermal reservoir connected via a heat leak rises to match the temperature of the 2DES. The differential measurement idea is that the experiment is mirrored on an identical system, so a bridge type circuit arrangement can detect the relative change in heat capacity, rather than an absolute measurement in which the small electron contribution needs to be resolved on top of a large addenda.

The dual cantilever-calorimeter measurement has a negative aspect, the gold film on the back of the cantilever required for a magnetometry measurement adds a significant contribution to the addenda. In this chapter the various components are investigated, and then the relative heat capacities are calculated and compared. The preliminary calorimetry experiments presented at the end of this chapter took place on the cold finger of the Leiden Cryogenics dilution refrigerator.

6.3.2 Heaters and tracks

The heaters tracks were made from evaporated gold of $50\,\mu$m to $62.5\,\mu$m width. It was desirable to have a heater with a stable and predictable resistance at low temperatures, and whose resistance was fairly independent of temperature at low T. The gold tracks on the cantilever are $50\,\mu$m in width for the majority of the coverage, which is not difficult in itself to produce, but to cover a large area without a break in the track makes it a challenge. The first calorimeters, A3970 (a $10\,\mu$m drumskin) and C2507 (a $5\,\mu$m drumskin) had track thicknesses of $\sim 5\,$nm, but the continuity was broken at some point in the manufacture in several places. The tracks are composed of ~ 1000 squares, and in the manufacture and transport, even with great care, 'breaks' occur. The problems included:

1. The devices had many stages of production, handling them could be minimised but not avoided, therefore scratches occurred. Before the processing was mod-

ified to consider the fragility of thin tracks, over a ~ 1000 square pattern there were up to ~ 10 scratches causing breaks.

2. Dirt on a 16 mm × 19 mm device may not be noticed, due to contrast and the large scale. If the dirt exists in a track area, and is not cleaned away, gold is evaporated over the dirt which falls away later, causing a break. An example of such a break is in figure 6.6. This can affect a thick track (200 nm) as well as the thin tracks.

3. Moving the device from Sheffield to Exeter in some sort of packaging.

The resistance of a thin film of gold as a function of thickness is hard to estimate in this regime (< 50 nm), as conduction is not 2D, but is poorly predicted by using 3D values for σ. Four calorimeter heater tracks were evaporated on an insulating GaAs wafer, along with thick heater tracks to make connections. The heater tracks were created in exactly the same way as in the final calorimeter device, but without the etching steps. This additionally gave an opportunity to optimise the process by highlighting steps which may damage the surface, which were unavoidable, and to discover what thickness of film could survive the processing.

Figure 6.7 demonstrates how the two-terminal resistance of the heater tracks, at a thickness near 5 nm, becomes rapidly more resistive. The processing highlighted that for few processing steps it is possible to create and transport thin film tracks from Sheffield to Exeter with a high success rate. However, for a full calorimetry device with more processes (more opportunities to contaminate the surface), the chances of damaging the surface are high and a selective repair evaporation will be needed.

The 10 nm tracks had a suitable resistance, and were no less fragile than the slightly thicker tracks so were selected for subsequent devices. The heat capacity of the tracks for this thickness, in the region of the 2DES is calculated to be $\sim 1.7 \times 10^{-13}\,\mathrm{J\,K^{-1}}$ at 100 mK.

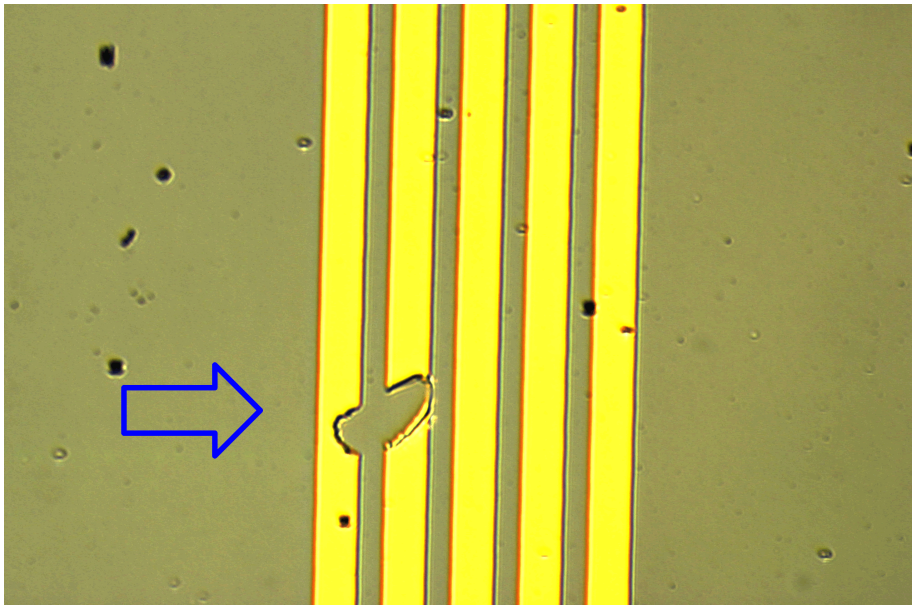

Figure 6.6: Example of dirt on the surface causing a break in a thick gold track.

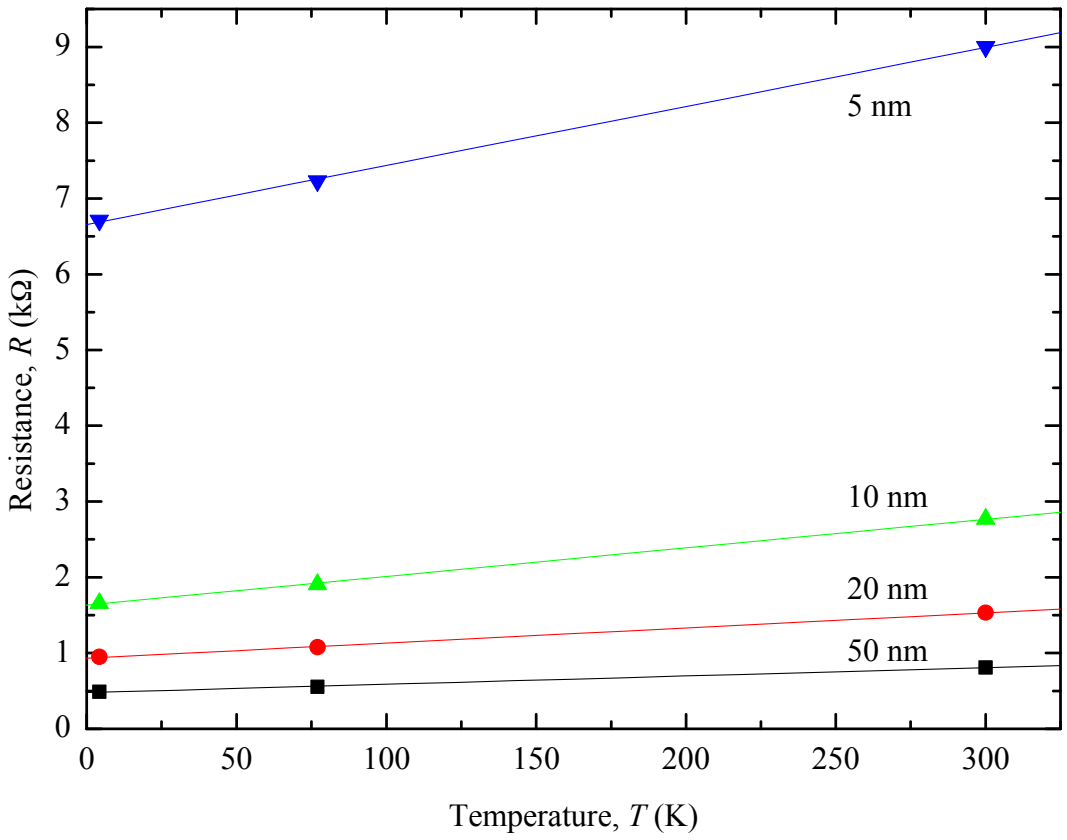

Figure 6.7: Thin films of gold for various thicknesses as a function of temperature.

6.3.3 Thermometry

Careful consideration had to be given to the choice of thermometer for this device. A thermometer that is more robust would probably have a comparatively slower response, and a thermometer useful over a large range of temperatures would be likely to be relatively insensitive in the region of interest. The thermometer needed to be fast responding, which equates to having a small mass. As this is a heat capacity measurement, the small mass was also needed to minimise the background heat capacity of the calorimeter addenda. The thermometer needed to vary from room temperature right down to $\sim 20\,\mathrm{mK}$, but did not need to have a constant sensitivity over the entire range, just a high sensitivity at low temperatures. Bearing in mind that this measurement would take place on a cantilever, the composition of the thermometer needed to have as small a magnetic moment as possible. Additionally, the thermometer needed to have a small, or at least predictable magnetoresistance.

The choice made for such a resistive thermometer was a thin film of $\mathrm{Au}_x\mathrm{Ge}_{1-x}$. These had been reported to have a high sensitivity due to a short thermal relaxation time and a low mass, and recently $< 10^{-18}\,\mathrm{J\,K^{-1}}$ resolution has been achieved by Fon et al. [92]. Also, the system was known to have a strong conductivity dependence on gold concentration, and therefore could be tailored to specific requirements. These thin films, at certain compositions near the metal-insulator transition, have already been seen to have conductivities that, when extrapolated to 0 K, have no minimum [93].

The first batch of resistors was manufactured by flash evaporation, in a similar process to Dodson et al. [93]. Flash evaporation consisted of heating 45 mg of Ge and 4.5 mg of Au in a tungsten 'basket', to be mixed before evaporation, the heat in the coil was then increased and the shutter opened when there were signs of evaporation. Evaporation lasted ~ 30 seconds, or until all the material was gone, which corresponded to a film of 100 nm. This is an easy process consisting of one pump down to vacuum, and one evaporation process. However, the resistors of this first batch were not satisfactory, by 4.2 K the resistors were in the range $0.5\,\mathrm{M\Omega} - 1\,\mathrm{M\Omega}$. This was attributed to the film recipe being deficient in gold, which could be rectified,

but the variation between 'identical' devices, i.e. same evaporation, was a problem. Because gold and germanium have different evaporation rates, gold concentration may have varied during evaporation, this indicates a difficulty in reproducing identical resistors each time, consistent with the observation Dodson et al. made: the end products were strongly dependent on growth conditions.

More recently, Fortune et al. [94] reported a method for fabricating such resistors reliably, which largely removed uncertainties given by annealing conditions. The fabrication technique allows the tuning of two parameters: the room temperature resistivity ρ_{RT} and the temperature sensitivity $\eta(T)$. The method deposits gold and germanium sequentially grown in bilayers. Their thermometers were grown with 50 bilayers on a single crystal sapphire substrate, in which each bilayer consisted of 8.4Å of Au on top of 43Å of Ge which corresponds to 18% (atomic) Au. To transform the polycrystalline film into a distribution of Au clusters confined to polycrystalline Ge grain boundaries, the film was annealed at 265°C.

For precision calorimetry, it is important that the thermometer has a short thermal relaxation time in the low temperature region, and therefore a low mass. The aim was to produce thinner thermometers that worked just as well, of similar composition, but consisting of only 5 or 10 bilayers.

Fortune et al. measured the room temperature resistivity of their samples after increments in annealing temperature of 30 minute durations. As can be seen in figure 6.8 they observed that the room temperature resistivity ρ_{RT} increased by approximately an order of magnitude, only to drop again at a critical temperature of 135 °C. This was attributed to the onset of gold-assisted germanium crystallization.

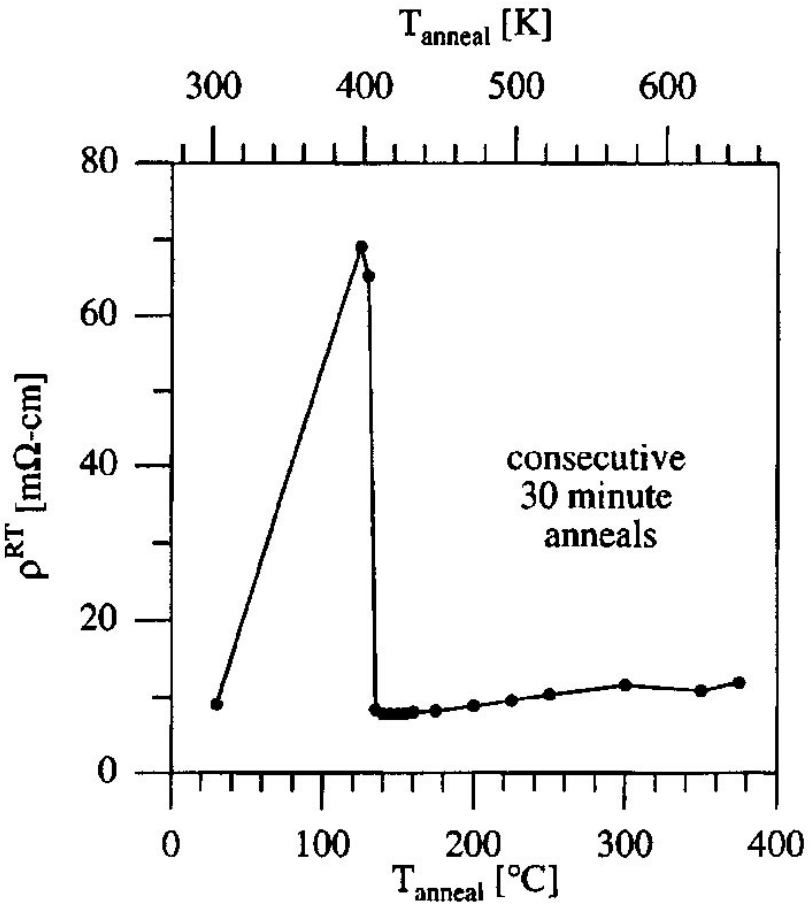

Figure 6.8: Dependence of room temperature resistivity on annealing temperature, taken from Fortune et al. [94]

The increase in resistivity after the deposition at 40 °C can be attributed to the gold atoms that have already diffused into the amorphous germanium layer beginning to cluster into small gold grains, as the metal is not soluble in crystalline germanium. During anneals at and above 135 °C the relatively weak gold-germanium bonding in the amorphous film mediates the exchange of germanium for gold, allowing the rearrangement and crystallization of germanium in a process known as *metal-assisted crystallization,* investigated by Tan et al. [95]. This critical temperature depends on the gold concentration, as pure germanium films do not crystallize until $350-600\,^{\circ}\mathrm{C}$ depending on the deposition conditions [96].

The mechanism for the formation of gold and germanium islands, which appear to

be fractal, in this metal/semiconductor thin film is not well understood. However, an in situ TEM (Transmission Electron Microscopy) study of fractal formation in amorphous AuGe bilayer films by Zhang et al. [97] gave a qualitative understanding of what is happening to the structure of the films with an increased annealing temperature.

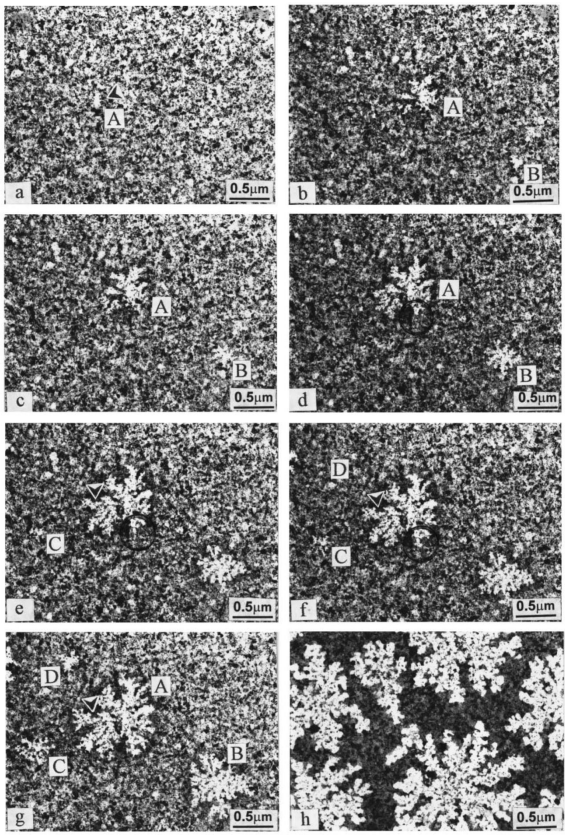

Figure 6.9: Fractal crystallization process as a AuGe film is annealed at 120 °C at ∼10 min intervals in (a)-(g), then (h) an additional 10 min at 135 °C. Light contrast is Ge, dark contrast Au. Taken from Zhang et al. [97].

Figure 6.9 illustrates the fractal crystallization process in a single Au/Ge bilayer (layer thickness ratio of 30nm/30nm). Because the electron scattering of the gold is much stronger than that of germanium, the dark contrast is from gold grains, the dark grey is a mixed region and the white features are from germanium clusters. The 8 images show how the crystallization process progresses with time for a relatively constant temperature of 120 °C. [97] reported that when the annealing temperature was increased to 135 °C the polycrystalline germanium morphologies dramatically covered the whole area of the film (h). The effect of heating is to cause larger gold

grains to grow at the expense of smaller grains, the size of the germanium fractal patterns increase in addition to new patterns forming.

Test thermometers for the Exeter cantilever-calorimeter were approximately square films of 3 mm × 3 mm, defined by photolithography. Two batches of AuGe resistors were manufactured, of these results for 5C (5 bilayers) and 10C (10 bilayers) are presented. Both were grown as bilayer structures with a Au/Ge ratio of 11.1 Å/43 Å. The films were annealed for 30 minute durations and their room temperature resistances were measured when they had cooled. Figure 6.10 shows the calculated resistivities for the two resistors as a function of anneal temperature. Up to a critical temperature of 210°C the room temperature resistivity increases, consistent with the picture that the gold is forming islands in the structure, but the average separation of islands is increasing. After the highest anneal temperature of 270°C, the resistivity has dropped, essentially becoming a conducting film. The explanation of this is that at higher anneal temperatures either the gold has been expelled from the Ge, or similarly, a proportion of the germanium has diffused into the bulk GaAs, leaving a high concentration of gold. Diffusion into the substrate is not desired and this could potentially perturb the electron system under investigation. AuGe structures of 5 bilayers worked, but as there was some disparity between thermometers of the same batch, 10 layers were adopted so that errors in deposition were more likely to be smoothed out. In this batch of resistors, some films demonstrated non-ohmic behaviour which was attributed to the gold contacts forming Schottky barriers, either through the deposition order, or a mechanical shadowing effect.

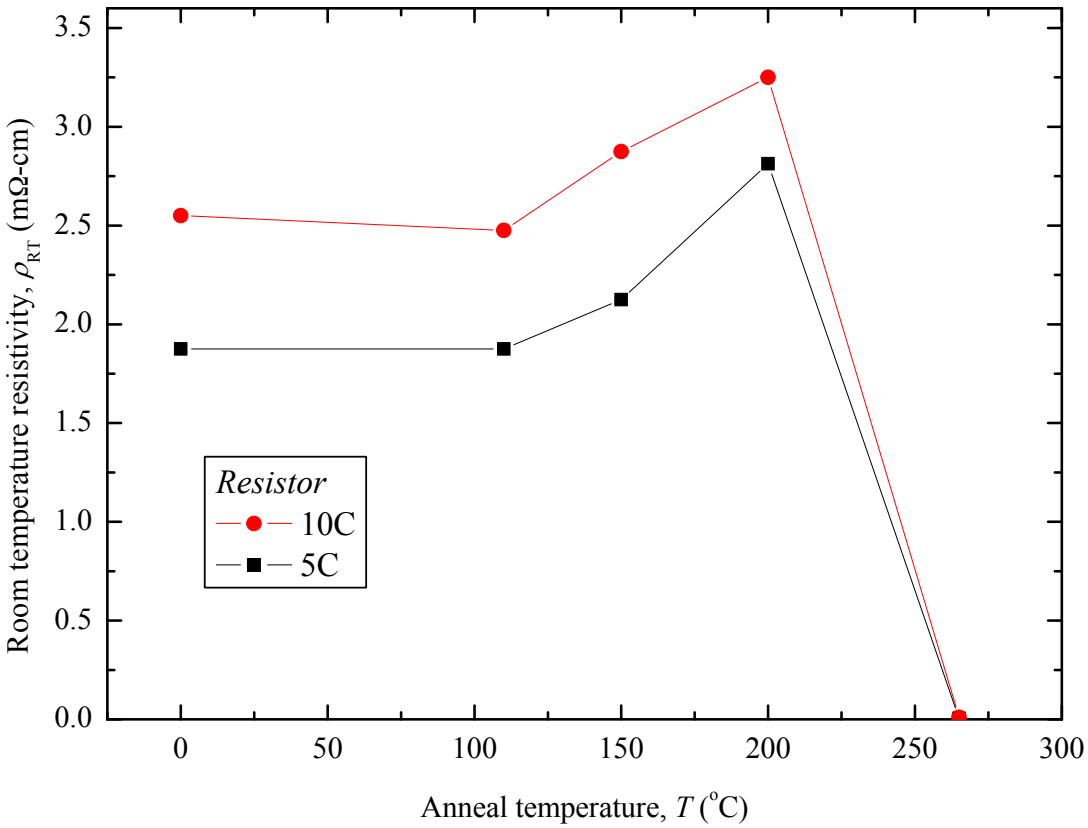

Figure 6.10: Room temperature resistivity dependence for various anneal temperatures, for resistors of 5 layers and 10 layers.

Different concentrations were investigated, 18%,20% and 24%. The 24% gold concentration gave the best temperature dependence, and required the lowest anneal temperatures to produce a thermometer that was sensitive down to 4.2 K. For this batch the films were deposited on top of pre-defined gold contacts which overlapped on two edges, as opposed to depositing the contacts down after the film anneal. The success of contacts increased by using this method.

After the thermometers had been grown, before an anneal (other than the temperature of the growing conditions), the temperature dependences were not very useful, they were fairly conductive down to liquid helium temperatures. By annealing the thermometers at a particular temperature, the room temperature resistivity could be varied as well as the thermometers' sensitivity. Temperature dependences for anneal temperatures up to 175 °C are shown in figure 6.11.

After subsequent 30 min anneals at the same temperature for a thermometer of this composition, little change was seen, indicating that a 30 min anneal was sufficient. The resistance increased by $\sim 90\%$ after the first anneal, but $< 5\%$ in later anneals at the same temperature.

For a 10 layer Au/Ge thin film resistor, the estimated heat capacity is $1.26 \times 10^{-16}\,\mathrm{J\,K^{-1}}$ at 100 mK.

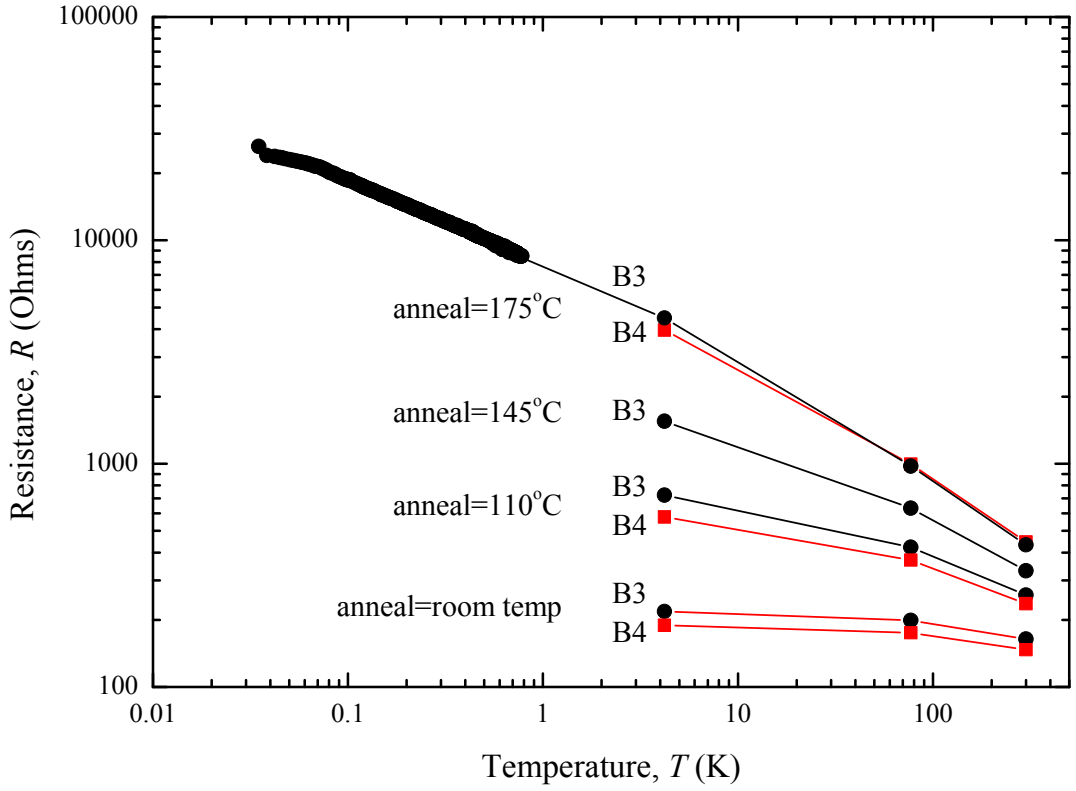

Figure 6.11: A log-log plot of the temperature dependence of thermometers B3 and B4, Au:Ge 11.1 Å : 43 Å bilayers after different 30 minute anneals.

6.3.3.1 Temperature Dependence and Sensitivity

Resistor D5 was part of a batch of test thermometers for calorimeter A3970B, evaporated at the same time. The temperature dependence can be seen in figure 6.12. D5 was annealed and calibrated at room temperature, 77 K, and 4.2 K approximately 10 months before the temperature sweep below 1 K. In that time the room temperature

resistance had changed by less than 8%, and the thermometer was still sensitive at dilution fridge base temperature.

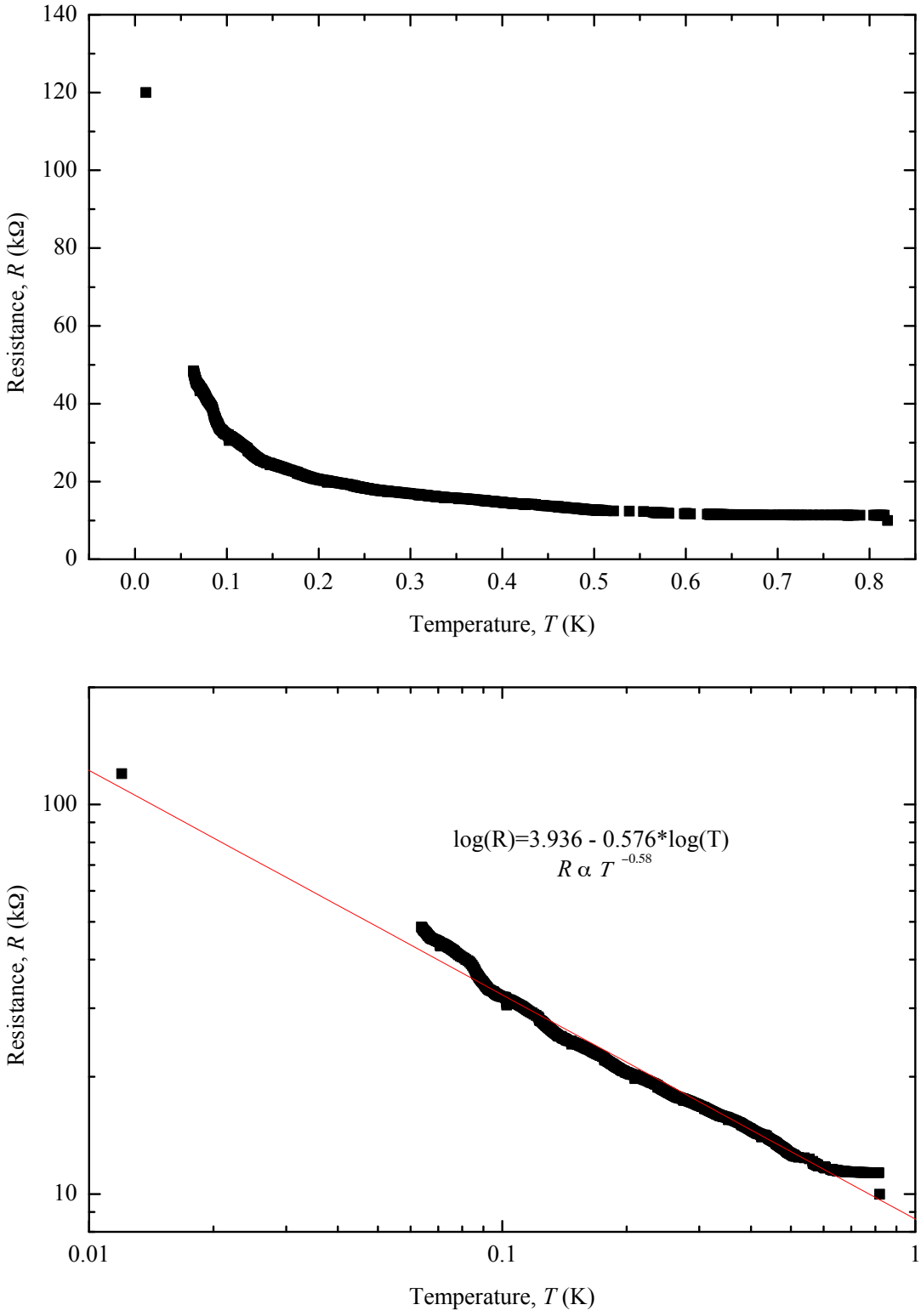

Figure 6.12: Temperature dependence of thermometer D5.

The resistor temperature dependence in figure 6.12 can be presented as the change in resistance per change in temperature, i.e [Ω/K]. This quantity is geometry dependent. i.e. dR/dT scales with R. For this reason it is often conventional for sensitivities to be normalised by dividing by the measured resistance to give a sensitivity, S_T, in change per kelvin.

$$S_T = \left(\frac{1}{R}\right)\left(\frac{dR}{dT}\right), \tag{6.5}$$

where T is the temperature in kelvin and R the resistance in ohms. However, as the Au/Ge bilayer thermometers seemingly obey a power law dependence, it is convenient to quote the sensitivity as

$$S = \left|\frac{\log R}{\log T}\right|, \tag{6.6}$$

which is approximately constant over the temperature range 100 mK to 800 mK, $S = 0.58$. The thermometer measuring the temperature of the mixing chamber was not ideally situated, which explains the deviation below 100 mK; the point at 29 mK was taken at base temperature after the fridge had been stable for a few hours. The AuGe thermometers on the final calorimeter will be slightly different from each other, and each will require its own calibration. Although the error in calibrating the thermometers may be several mK, providing the fractional change is approximately constant it does not matter.

6.3.3.2 Magnetic field dependence

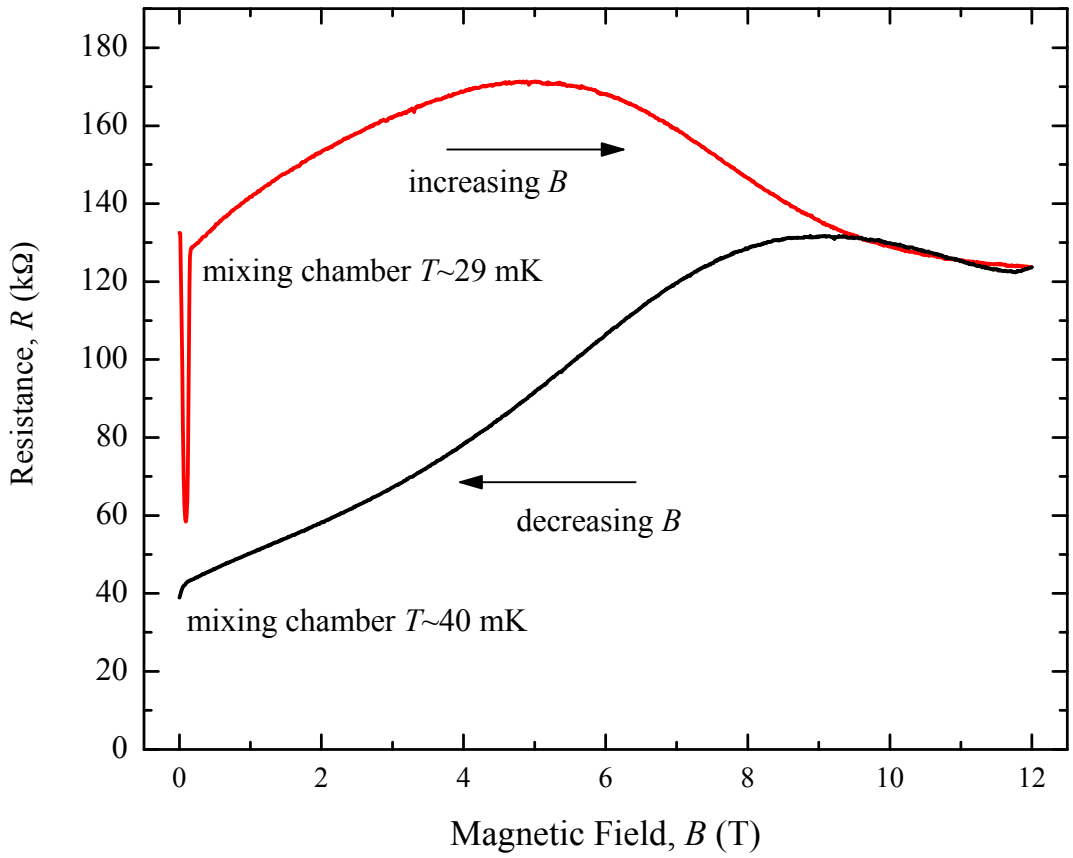

Figure 6.13: Magnetic field dependence of resistance of thin film thermometer D5.

With the refrigerator in single shot mode, the magnetic field dependence of the resistance of the thermometer was investigated, figure 6.13. The difference between the up and the down sweep is due to a temperature drift. The drift is emphasised because the fridge is at base temperature where the temperature dependence of the thermometer is most sensitive.

The run started at 29 mK, and due to sweeping finished at a mixing chamber temperature of 40 mK. There is a small discrepancy in comparing the value to the temperature calibration in figure 6.12, but the field dependence value (at zero field) is probably the correct value, as in this case the system is warming, but in the temperature dependence experiment it was cooling and there was probably a thermal

lag to the calibration thermometer. The thermometers had a sufficiently small and reproducible magnetoresistance that it could be accounted for in a calibration.

6.3.3.3 Noise

The best case scenario for the thermometer is that it is limited by the broadband thermal noise,

$$S_n = 4k_{\mathrm{B}}TR. \tag{6.7}$$

At a base temperature of 30 mK is, the resistance is $\sim$ 120 kΩ, so the noise is calculated to be,

$$S_n \sim 2.0 \times 10^{-19}\,\mathrm{V^2\,Hz^{-1}}.$$

Using the 5210 lock-in amplifier, with a time constant 10 ms and 3 time-constants per point, the voltage across the thermometer terminals was measured against time. The noise was measured as a function of frequency, (with no filters) at a temperature of 30 ± 2 mK. From figure 6.14 the measured thermal noise was $\sim 2 \times 10^{-15}\,\mathrm{V^2\,Hz^{-1}}$ at > 1 kHz, with a non-Gaussian noise that obeyed $\sim 1/f$ at low frequencies.

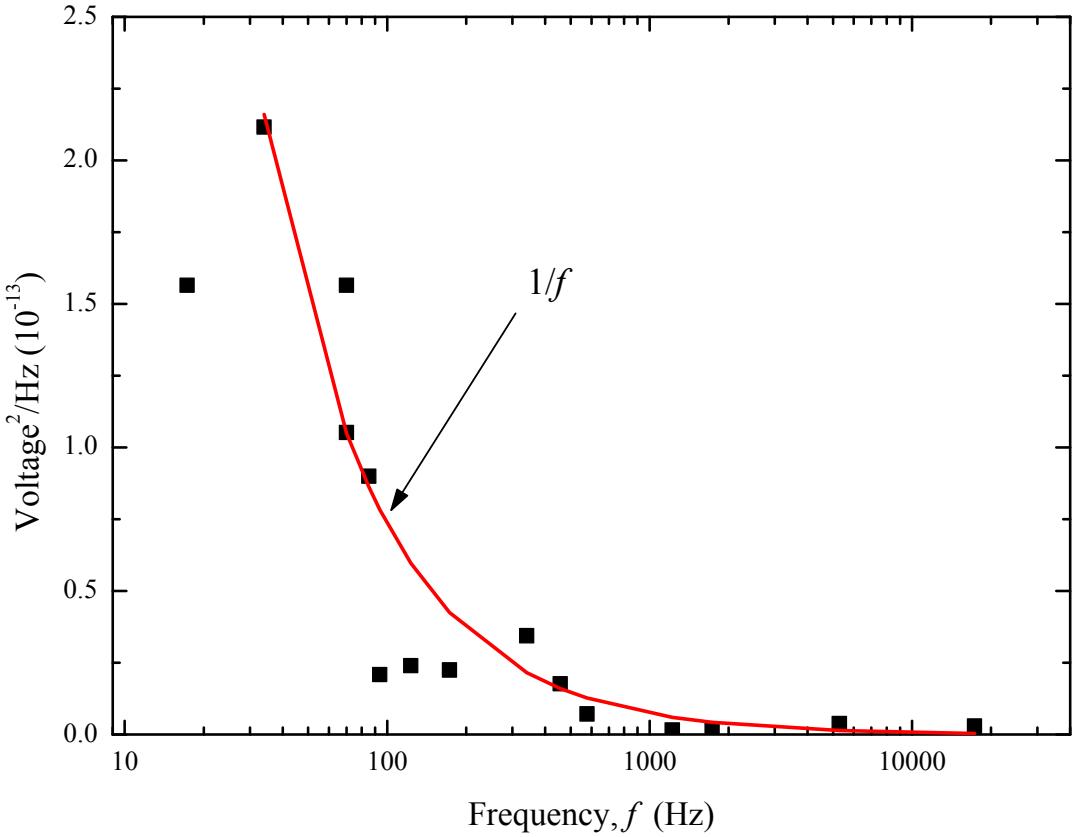

Figure 6.14: Zero magnetic field AuGe thin film thermometer D5 noise characteristic, with no driving current.

The thermal noise is therefore $\approx 0.45\,\mathrm{nV}/\sqrt{\mathrm{Hz}}$, which is comparable with a good lock-in amplifier ($\sim 1\,\mathrm{nV}/\sqrt{\mathrm{Hz}}$).

6.3.4 Processing of Device

The calorimeter-cantilever devices were processed at the EPSRC National Centre for III-V Technologies at the University of Sheffield by Dr Geoff Hill and myself. Typical device requirements are on the scale of $<$ mm, so many devices can be made on the same wafer for little extra expense or effort. It does not matter if a few devices do not work, and it is normal to have a yield much less than 100%. The Exeter cantilever-calorimeter is comparatively large, $\sim 16\,\mathrm{mm} \times 19\,\mathrm{mm}$, and the success rate of all tracks, evaporated thermometers and contact pads needs to be

very close to 100% to have a useful device. By working with Sheffield, the process was refined to give a better success rate.

An outline of the fabrication process is given below. The design in figure 6.4 is broken up into several chrome masks rather than one. The chrome masks are created in the conventional way.

1. Preparation of wafer

   (a) Scribe the GaAs/(Al,Ga)As to 16 mm × 19 mm.

   (b) Clean the samples with n-butyl acetate with cotton buds [98] cleaning towards the edges. Blow dry with a nitrogen gun.

   (c) Mount sample 2DES face up onto a glass cover-slip, using wax on a hotplate at a temperature of 100 °C, and cool with a flow of dry nitrogen. The cover-slip is essential for handling of the device, to keep contact with the surface to a minimum.

   (d) Place sample onto a spinner, held in place by a vacuum. Cover with PMMA [99] photoresist and spin at 4,000 rpm for 30 seconds (resulting in a film thickness of $\sim$ 350 nm). Bake on a hotplate at 100 °C for 60 seconds. Baking for too long may result in the photoresist becoming too hard/dry.

   (e) Inspect under the microscope as it is possible the photoresist bottle is contaminated with dirt. If there is any dirt then clean with acetone, IPA, dry and repeat (d).

2. Etch mesa

   (a) Using a mask aligner (Karl Suss MJB3), align the first mask and expose under UV light for 2 seconds (precise number varies with each instrument).

   (b) Place into a PLSI [100] developer for 60 seconds, then straight into a beaker of de-ionised water (release tweezers to clean PLSI from them), then remove from beaker and rinse in a flow of de-ionised water.

(c) Etch the surface in 1:8:80, sulphuric acid: hydrogen peroxide: water, this will etch the GaAs at $\sim$ 400 nm/minute. Before etching, monitor the height of the photoresist with a Dektak stylus profilometer (Dektak 3030ST). The 2DES was $\sim$ 90 nm beneath the surface, so aim to remove $\sim$ 150 nm

3. Thin track exposure with contact lithography

(a) Inspect the remaining photoresist mask on the sample. As there are a lot of thin tracks it is possible some may not have been defined properly, some may be shorted, or there may be some dirt in a 'trench'. If dirt cannot be removed with a flow of de-ionised water then the surface needs to be cleaned with Acetone and IPA, and the process started again.

(b) Place in a thermal evaporator (Edwards E306A thermal evaporator) close to the quartz crystal oscillator (for measuring film thickness) and pump down to a evaporation pressure. Evaporate a layer of gold by passing a current of 20 A and monitor the crystal oscillator. A wetting layer of titanium needs to be evaporated first so the gold adheres to the surface. From a typical evaporation: 1.5 nm Ti ($\sim$ 5 sec deposition) and then 9.8 nm Au ($\sim$ 20 sec deposition).

(c) Leave to cool.

(d) Lift off: Clean off the photoresist and excess gold in acetone, IPA and blow dry. During lift off, the photoresist underneath the evaporated thin metal film is dissolved in acetone, leaving behind a thin metal film where the pattern was photolithographically defined. Squirting acetone across the surface helps to remove loose gold. The gold tracks are close together, if the photoresist had a lip then lift-off tracks may get trapped.

4. Thick track exposure

(a) Lithography and evaporation. Slightly thicker wetting layer of $\sim$ 10 nm Ti, followed by 150 nm to 200 nm of gold.

(b) Inspect.

5. Thermometer exposure

(a) Lithography.

(b) Evaporation: 10 layers of Ge and 10 of Au, 43 Å to 11.1 Å. So that the crystal oscillator does not need to be adjusted, keep setting as for Ge, 11.1 Å of gold corresponds to a thickness setting of 40 Å when set for Ge. The typical current required to start evaporation for Ge is 26 A. It is 20 A for gold.

(c) Figure 6.15 shows a typical orientation for an evaporation process. The deposition gradient may be subtle but the effect on the thermometers is significant. The source is ~ 20 cm away from the sample.

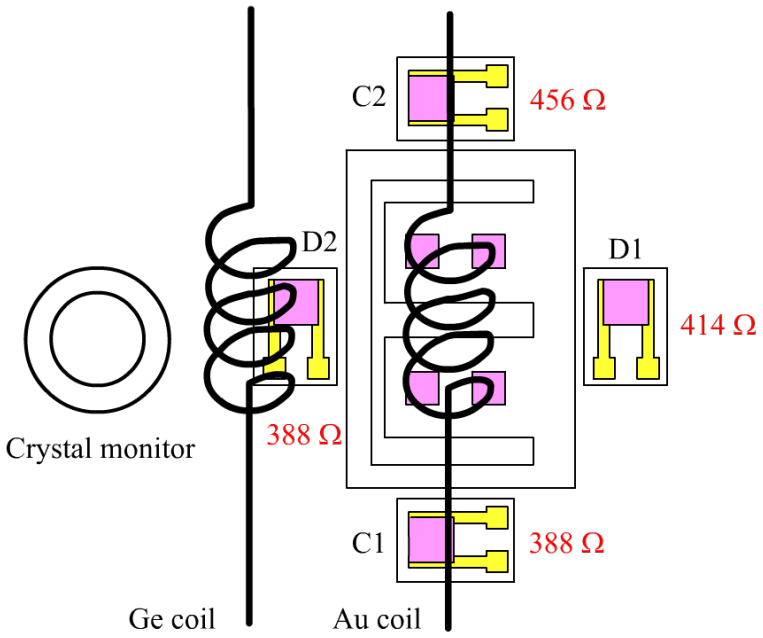

Figure 6.15: Orientation of calorimeter and test thermometers in the evaporator. Room temperature resistances are shown to illustrate the deposition gradient of the thermometers.

6. Lithograph cantilever edges and etch.

7. Last chance to repair tracks. Repair consists of re-defining the thin tracks, using PMMA to select out 'good' areas, and then re-do a thin track evaporation.

8. Polish to $\sim 150\,\mu$m. (Buehler Minimet 1000 grinder/polisher with Buehler Metadi II 3μm diamond polishing compound). Getting an even surface is the most important aspect of the back etch procedure.

9. Perform the back etch, up to the Al etch stop.

Problems that can occur

Apart from scratches, or holes in tracks due to surface contamination during an evaporation, other problems can occur. Figure 6.16 demonstrates the thin gold tracks on the cantilever are damaged due to hot gold during an evaporation damaging the photoresist. A hot gold lump damaged the photoresist between the outer leg of the thermometer and an adjacent track, thus creating a short between the tracks. The calorimeter was repaired by use of a focused ion-beam etching machine to remove material and create a small trench in the gold short, insulating the two tracks from one another (indicated by a red arrow).

If the polishing stage does not produce a flat sample, the etching will not be even. Figure 6.17 shows a photo of the corner of a cantilever. The etch has gone through the Al etch stop in some areas, but not others. Typically it is the corners that are susceptible.

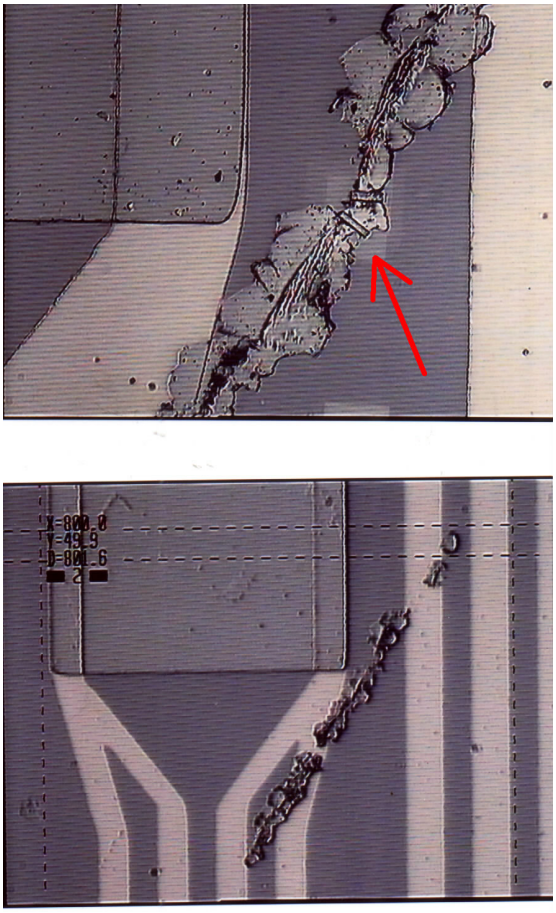

Figure 6.16: Repair of thin gold tracks. The top image is a magnified version of the bottom. Hot gold damaged the photoresist during evaporation and shorted some tracks. The top image shows a FIB repair, a small trench of material is removed to insulate the tracks (red arrow). Repair carried out by Geoff Hill.

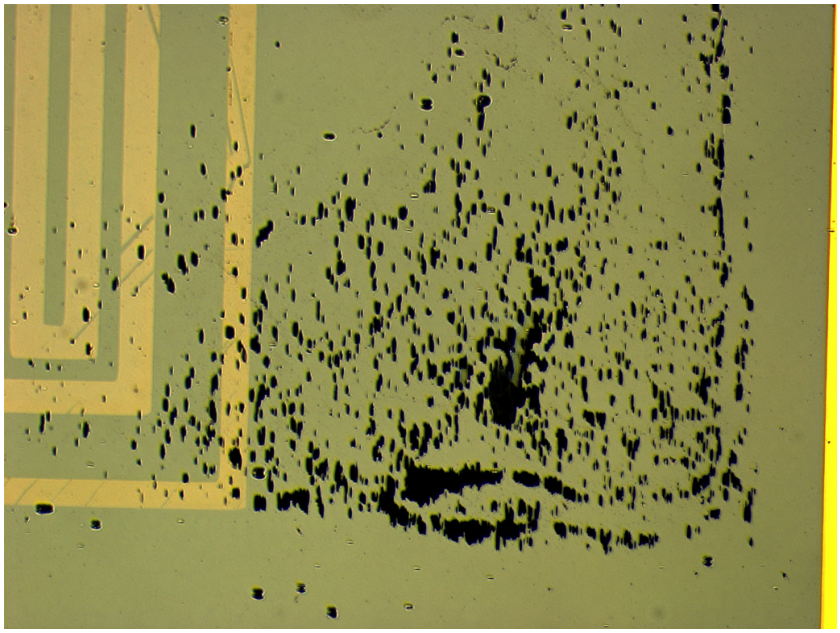

Figure 6.17: Corner of heater tracks on a cantilever. The etch has gone through the stop and damaged the cantilever.

6.3.5 Contacting the Calorimeter and external connection

The calorimeter was mounted on the cold finger of the Lieden Cryogenics fridge. It was not possible to make make electrical contact to the calorimeter with a conventional wire bonding machine. A drumskin calorimeter proved to be too delicate, and fractured due to the ultrasonic bonding technique. Silver paint contacts were used, as depicted in figure 6.18.

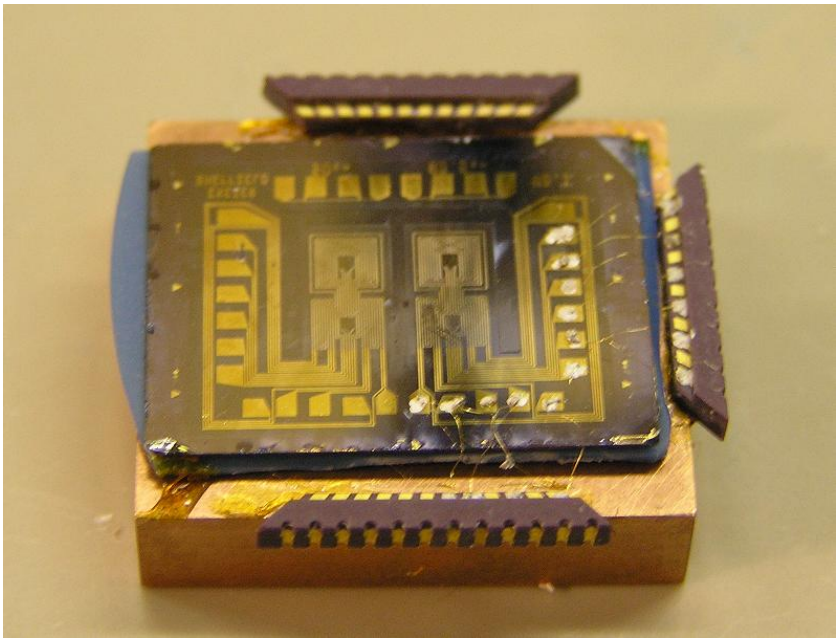

Figure 6.18: Calorimeter A4182, contacted with silver paint contacts.

6.3.6 Preliminary Calorimetry Measurements

After problems with a full model cantilever-calorimeter device, the aim was to establish that a thermometer on a more robust device could be made to work, and measure a temperature change due to a heat pulse. Calorimeter A4182 is shown in the mounting arrangement in figure 6.19. The lowest temperature achievable due to problems with the refrigerator was $\sim 270\,\mathrm{mK}$. At this relatively high temperature for a heat capacity measurement, the smallest heat pulse resolvable was 25.7 nJ (200 ms duration, 30 mV height).

In a fixed rate magnetic field sweep, with a constant excitation current of 100 nA in the thermometer which itself acted as a heater, oscillations were measured arising from the 2DES underneath, as in figure 6.20. The experiment took place after illumination with a red LED at refrigerator temperatures. There are prominent oscillations which are periodic in inverse magnetic field, up to $\nu = 12$, but with some features beyond this. Assuming the filling factors to be present at the displayed positions in figure 6.20, a corresponding number density was calculated to be $n_s = 3.26 \times 10^{11}\,\mathrm{cm}^{-2}$. This is comparable with the result from a Hall bar measurement at

Cambridge of $n_s = 3.47 \times 10^{11}\,\mathrm{cm}^{-2}$, which took place on a different piece of the same wafer. It is promising that a thermal measurement was able to resolve oscillations, but further work is required to quantify the magnitude of the oscillations so that a heat capacity for the 2DES can be calculated.

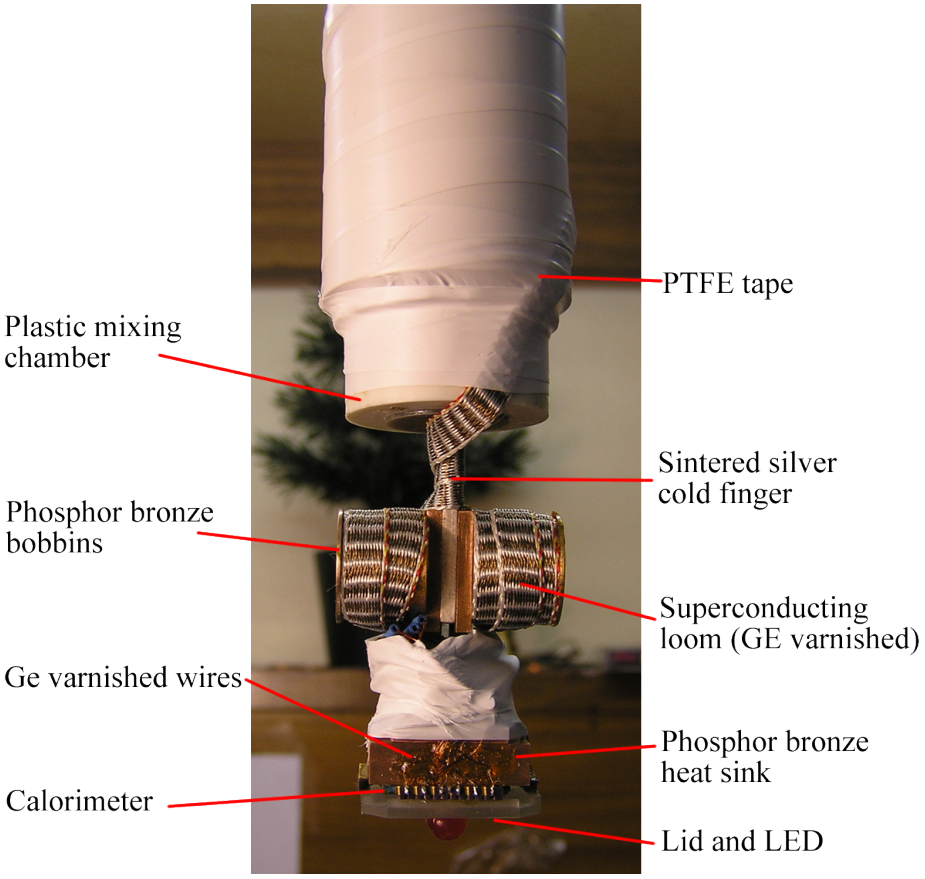

Figure 6.19: The experimental setup for the preliminary calorimeter experiment.

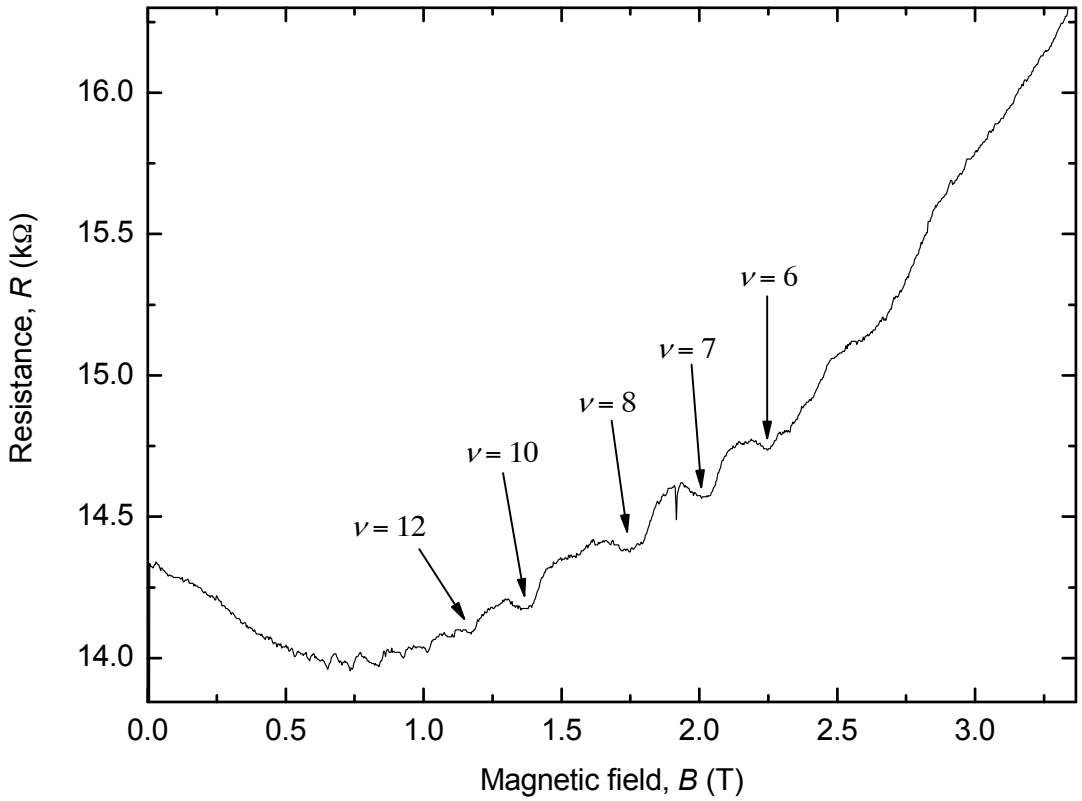

Figure 6.20: Response of thermometer on thinned calorimeter A4182 to constant thermometer heating at 270 mK.

6.4 Conclusions

A method has been presented for the fabrication of a novel device, to measure the magnetisation and the heat capacity of a 2DES at the same time.

AuGe thin film resistors were grown in only 10 bilayers, reducing the heat capacity per unit area by an order of magnitude on Fortune et al. [94]. The AuGe thermometers were shown to be 'tunable', i.e. the temperature dependence was dictated by the annealing conditions after growth, so thermometers with different gold concentrations due to growth conditions, could be tuned to have similar temperature dependences. The magnetoresistance of the thin films was investigated and shown to be predictable and much smaller than the drift associated with a temperature change in the mixing chamber. It would be possible to calibrate a thermometer to

operate at magnetic fields, but this is not done here as a final calorimeter was not realised. Low temperature thermometers with small heat capacities were repeatably produced, and thermometer D5 was presented in this thesis with a sensitivity of $S = 0.58$ over the temperature range 100 mK to 800 mK.

It is possible from monitoring the orientation of the AuGe test thermometers in the deposition process, and by annealing and testing at only three temperature points, to establish the ideal annealing conditions for a more delicate cantilever-calorimeter so that it only needs to undergo one thermal cycle, minimising the risk of damage.

At an elevated refrigerator temperature of nearly 300 mK, heat pulses of $\sim$ nJ were resolved on a device which had a 100% front processing success rate, but was not etched from the back. The preliminary results are encouraging, and the device has been shown to be viable, and with the processing details described in this chapter, the device should be reproducible.

Performing a back etch to isolate the calorimeter from the rest of the device, creating a differential calorimeter successfully, is the next step. The project was not completed, but it has been shown that a device to measure the broadening of the low temperature, high magnetic field 2DES density of states is possible.

Chapter 7

Conclusions and Further work

7.1 Conclusions

This thesis has described an investigation into aspects of the integer quantum Hall effect, specifically the near-dissipationless state of the longitudinal resistivity ρ_{xx} between Landau levels, and the associated broadening of the levels.

Eddy currents induced by a time varying magnetic field B were considered in chapter 4. The temperature dependences of the eddy currents were measured over the range 100 mK to 1600 mK. Currents induced at even filling factors were more robust than odd filling factors for the same Landau level index, consistent with the cyclotron splitting being larger than the spin splitting. The peak current at filling factor $\nu = 2$ was shown to saturate at $\gtrsim 800$ mK, more robust than previously observed, but was reduced by elevating the temperature to 1600 mK. The saturated regime is associated with a breakdown of the quantum Hall effect, and in this case, the most likely candidate for the saturation is an electron heating effect. The shapes of the temperature dependences of the induced eddy currents were compared to predictions of the charge up model used by Kavokin et al. [70], and qualitatively agreed. It is interesting to note that if electron heating is responsible, then the eddy current must be de-coupled from the transport current, as temperature limiting is not evident in the transport measurements.

Sweep-rate dependences were characterised for a range of filling factors and temperatures, and even for the lowest sweep rates, never entered a linear regime. Induced currents $\nu = 1, 2$ and 4 all saturated at the same critical value at 100 mK, but $\nu = 4$ was shown to reduce with slower sweep rates, consistent with the prediction that the ρ_{xx} minima is not as small as for lower Landau levels.

Induced current decays were measured to be similar to previous work, a fast initial decay attributed to breakdown of the QHE followed by a much longer slow decay. The eddy decay of $\nu = 1$ at low temperature, in the slow decay regime, is among the most persistent reported. Surprisingly, the $\nu = 2$ decay was faster than the $\nu = 1$, inconsistent with the temperature and sweep rate dependences measured. The long decay of $\nu = 1$ suggests that, whatever the mechanism for the decay, spin is conserved.

The energy stored in an induced current was discussed, and it was shown that the assumptions of previous work had not evaluated the mutual inductance of the eddy current in the presence of the magnet sufficiently. The sweep rate IV characteristics were found to be a good description of the induced current for a given temperature, that could predict the shape of the eddy decays. By fitting a suitable function to the IV characteristic of $\nu = 1$ at a relatively high temperature to interpolate the behaviour near the turning point of the curve, and using a relatively simple discharge model, the shape of the induced current was modeled. The model agreed with the data, producing a similar shape and a very long time constant for the slow decay.

In chapter 5 the hysteresis in the magnetoresistance of a quantum point contact was investigated, through a simultaneous transport and magnetometry measurement. Induced currents corresponding to filling factors up to $\nu = 8$ were measured. Three corresponding features were measured in the magnetoresistance of a QPC, one more than previously seen.

The temperature dependence was measured simultaneously, and for Landau level filling factor $\nu = 1$, the general shape of the curves was the same. However, in the case of Landau level filling factor $\nu = 2$, the curves differed significantly, although

the data suffered from a poor signal to noise ratio, owing to the size of the magnetoresistance, and to jumps in the resistance arising from trapped charges relocating from under the gate. The later problem was solved by waiting at a fixed gate voltage for several days.

The sweep rate IV characteristics of the the two experiments were similar. The $\nu = 2$ sweep rate curves saturated over the entire range for both experiments. At 100 mK, it was possible to resolve the magnetoresistance feature at $\nu = 4$. The low sweep rate regime was investigated, and both the induced currents and the hysteretic magnetoresistance were reduced at low sweep rates.

Sweeping the magnetic field B to a fixed field position and waiting, demonstrated that both phenomena decay with time. Both decays were characterised by a fast decay of seconds and a slow decay taking more than $10,000$ seconds. By sweeping up and down over the field range of interest before the decay, an effective zero was found for the magnetoresistance, and a more enlightening comparison could be made. The magnetoresistance decayed to its effective zero faster than the induced current. As the QPC only detects local electrostatic perturbations, it can be concluded that the eddy current is decaying away from the edge, as well as decreasing in magnitude.

An attempt was made to affect the induced eddy current by switching the QPC gate on/off. A change in the geometry of the sample should have resulted in a reduced magnetic moment, but no change was observed to within 5%. Switching the gate on/off during a decay, even at high frequencies, did not induce any extra dissipation of the induced current. The induced currents would have flowed so as to avoid any impurities, and perhaps the area under the gate, even when switched off, created a barrier.

Experiments on a fast timescale, 10 ms, resolved structure in the induced currents that has previously been attributed to the noisy breakdown of the quantum Hall effect. Both the QPC resistance and the induced current had a larger signal to noise ratio in the fast regime near exact filling factors. By performing a simultaneous measurement, individual breakdown events were seen and correlated, which is one

more argument for the induced current causing the perturbation to the QPC gate.

After investigating the zero-resistance state in chapter 4 and chapter 5 with induced currents, exactly how the zero-resistance state varied between Landau levels was the topic of chapter 6. A method was presented for the fabrication of a novel device, to measure the magnetisation and the heat capacity of a 2DES at the same time, to not only improve on the measurements of previous work in both fields, but to make a direct comparison.

AuGe thin film resistors were grown in only 10 bilayers, reducing the heat capacity per unit area by approximately an order of magnitude on Fortune et al. [94]. The AuGe thermometers were shown to be 'tunable', i.e. the temperature dependence was dictated by the annealing conditions after growth, so thermometers with different gold concentrations due to growth conditions, could be tuned to have similar temperature dependences. The magnetoresistance of the thin films was investigated and shown to be predictable and much smaller than the drift associated with a temperature change in the mixing chamber. It would be possible to calibrate a thermometer to operate at high magnetic fields, but this is not done here as a final calorimeter was not realised. Low temperature thermometers with small heat capacities were repeatably produced, and thermometer D5 was presented in this thesis with a sensitivity of $S = 0.58$.

It is possible that, by monitoring the orientation of the AuGe test thermometers in the deposition process, and by annealing and testing at only three temperature points, established the ideal annealing conditions for a more delicate cantilever-calorimeter so that it only needs to undergo one thermal cycle, minimising the risk of damage.

At an elevated refrigerator temperature of nearly 300 mK, heat pulses of $\sim$ nJ were resolved on a device which had a 100% front processing success rate, but was not etched from the back. The preliminary results are encouraging, and the device has been shown to be viable, and with the processing details described in this chapter, reproducible.

It has been shown that a device to measure the broadening of the low temperature, high magnetic field 2DES density of states is possible. Performing a back etch to isolate the calorimeter from the rest of the device, creating a differential calorimeter successfully, is the next step.

7.2 Further work

The most obvious suggestion is the completion of the cantilever-calorimetry project. The device has been shown to be viable, but many of the design features were not realised, such as the differential measurement of calorimetry, the guard heater or obviously, the dual measurement of heat capacity and magnetisation.

In the QPC project, it was interesting to note that separating the 2DES into two areas had no effect on the induced current. Rather than splitting the 2DES into smaller fractions, if a large gate was deposited, then the area could be changed. Eddy currents in different geometry samples has been studied previously [64], but each geometry was a different sample, as opposed to changing the geometry of a single system.

The QPC was unable to affect the decay of the induced current. Perhaps the geometry of the gate was not ideal, i.e. the eddy current is wider than the widest QPC constriction. A 2DES with a split gate structure, which could be activated by a bias voltage with respect to a channel contact, would force the eddy current to change path. By forcing the eddy current edges from opposite sides, together, an additional loss mechanism may be introduced to the system, where by an electron can tunnel from one edge to the other, and this should be observable in a decay measurement.

In the induced current chapter, sweep rates for $\nu = 4$, the slowest sweep rate still did not produce a linear IV curve. At small enough sweep rates the curve is expected to become linear. In order to achieve slower sweep rates, for low field features, a magnetometer angled at 45^o to the applied field will experience a slower sweep rate that the 20^o rotor, and also experience a larger torque, because $\tau = mBsin\theta$.

If the eddy currents are causing a breakdown due to heating, then by using the thin film thermometers developed in this work, the temperature change due to current of $\sim 300\,\mu$A should be resolvable. The thin film thermometers can be made small enough that several could be positioned across the surface containing a 2DES.

Bibliography

[1] K. von Klitzing, G. Dorda, and M. Pepper. New method for high-accuracy determination of the fine-structure constant based on quantized hall resistance. *Phys. Rev. Lett.*, 45(6):494–497, 1980.

[2] T. Ando, Y. Matsumoto, and Y. Uemura. Theory of Hall effect in a two-dimensional electron system. *Journal of the Physical Society of Japan*, 39: 279–288, 1975.

[3] D. C. Tsui, H. L. Stormer, and A. C. Gossard. Two-dimensional magnetotransport in the extreme quantum limit. *Phys. Rev. Lett.*, 48:1559–1562, 1982.

[4] H. L. Stormer. Nobel Lecture: The fractional quantum Hall effect. *Rev. Mod. Phys.*, 71(4):875–889, 1999.

[5] M. P. Schwarz, D. Grundler, I. Meinel, Ch. Heyn, and D. Heitmann. Micromechanical cantilever magnetometer with an integrated two-dimensional electron system. *Applied Physics Letters*, 76(24):3564–3566, 2000.

[6] A.J. Matthews, A. Usher, and C.D.H. Williams. A low-temperature high-sensitivity torsion balance magnetometer with in situ stator adjustment. *Review of Scientific Instruments*, 75:2672, 2004.

[7] J. P. Eisenstein, H. L. Störmer, V. Narayanamurti, and A. C. Gossard. High precision de Haas-van Alphen measurements on a two-dimensional electron gas. *Superlattices and Microstructures*, 1(1):11 – 14, 1985.

[8] M. R. Schaapman, P. C. M. Christianen, J. C. Maan, D. Reuter, and A. D. Wieck. A multipurpose torsional magnetometer with optical detection. *Applied Physics Letters*, 81(6):1041–1043, 2002.

[9] R. Bachmann, F.J. DiSalvo Jr, T.H. Geballe, R.L. Greene, R.E. Howard, C.N. King, H.C. Kirsch, K.N. Lee, R.E. Schwall, H.U. Thomas, et al. Heat capacity measurements on small samples at low temperatures. *Review of Scientific Instruments*, 43:205, 1972.

[10] E. Grivei, S. Melinte, V. Bayot, H. C. Manoharan, and M. Shayegan. Multiple interacting bilayer electron system: Magnetotransport and heat capacity measurements. *Phys. Rev. B*, 68(19):193404, Nov 2003.

[11] J. K. Wang, D. C. Tsui, M. Santos, and M. Shayegan. Heat-capacity study of two-dimensional electrons in GaAs/AlGaAs multiple-quantum-well structures in high magnetic fields: spin-split Landau levels. *Phys. Rev. B*, 45(8):4384–4389, 1992.

[12] E. Gornik, R. Lassnig, G. Strasser, H. L. Störmer, A. C. Gossard, and W. Wiegmann. Specific heat of two-dimensional electrons in GaAs-GaAlAs multilayers. *Phys. Rev. Lett.*, 54(16):1820–1823, 1985.

[13] J.P. Eisenstein, H.L. Stormer, V. Narayanamurti, A.Y. Cho, A.C. Gossard, and C.W. Tu. Density of states and de Haas-van Alphen effect in two-dimensional electron systems. *Physical review letters*, 55(8):875–878, 1985.

[14] I. M. Templeton. A simple contactless method for evaluating the low-temperature parameters of a two-dimensional electron gas. *Journal of Applied Physics*, 62(9):4005–4007, 1987.

[15] R.C. Ashoori and R.H. Silsbee. The Landau level density of states as a function of Fermi energy in the two dimensional electron gas. *Solid State Communications*, 81(10):821 – 825, 1992.

[16] T. P. Smith, B. B. Goldberg, P. J. Stiles, and M. Heiblum. Direct measurement

of the density of states of a two-dimensional electron gas. *Phys. Rev. B*, 32 (4):2696–2699, 1985.

[17] Hou-zhi Zheng, Aimin Song, Fu-hua Yang, and Yue-xia Li. Density of states of the two-dimensional electron gas studied by magnetocapacitances of biased double-barrier structures. *Phys. Rev. B*, 49(3):1802–1808, 1994.

[18] F. F. Fang and W. E. Howard. Negative field-effect mobility on (100) Si surfaces. *Phys. Rev. Lett.*, 16(18):797–799, 1966.

[19] H. Etz, W. Gombert, W. Idstein, and P. Leiderer. Stability of charged 4He films. *Physical Review Letters*, 53(27):2567–2570, 1984.

[20] G. Mistura, T. Gunzler, S. Neser, and P. Leiderer. Microwave study of screened two-dimensional electron crystals on helium films. *Physical Review B*, 56(13): 8360–8366, 1997.

[21] S. M. McMurry and A. Van Someren. *Quantum Mechanics*. Addison-Wesley Longman Publishing Co., Inc., Boston, MA, USA, 1993. ISBN 0201544393.

[22] A. H. MacDonald, H. C. A. Oji, and K. L. Liu. Thermodynamic properties of an interacting two-dimensional electron gas in a strong magnetic field. *Phys. Rev. B*, 34(4):2681–2689, 1986.

[23] Qiang Li, X. C. Xie, and S. Das Sarma. Calculated heat capacity and magnetization of two-dimensional electron systems. *Phys. Rev. B*, 40(2):1381–1384, 1989.

[24] W. Zawadzki and R. Lassnig. Specific heat and magneto-thermal oscillations of two-dimensional electron gas in a magnetic field. *Solid State Communications*, 50(6):537 – 539, 1984.

[25] A. Potts, R. Shepherd, WG Herrenden-Harker, M. Elliott, CL Jones, A. Usher, GAC Jones, DA Ritchie, EH Linfield, and M. Grimshaw. Magnetization studies of Landau level broadening in two-dimensional electron systems. 8:5189–5208, 1996.

[26] C. Kittel and P. McEuen. *Introduction to solid state physics*. Wiley New York, 1996.

[27] D. Shoenberg. Magnetization of a two-dimensional electron gas. *Journal of Low Temperature Physics*, 56(5):417–440, 1984.

[28] M. Zhu, A. Usher, AJ Matthews, A. Potts, M. Elliott, WG Herrenden-Harker, DA Ritchie, and MY Simmons. Magnetization measurements of high-mobility two-dimensional electron gases. *Physical Review B*, 67(15):155329, 2003.

[29] S. A. J. Wiegers, M. Specht, L. P. Lévy, M. Y. Simmons, D. A. Ritchie, A. Cavanna, B. Etienne, G. Martinez, and P. Wyder. Magnetization and energy gaps of a high-mobility 2D electron gas in the quantum limit. *Phys. Rev. Lett.*, 79(17):3238–3241, 1997.

[30] V. Bayot, E. Grivei, S. Melinte, M. B. Santos, and M. Shayegan. Giant low temperature heat capacity of GaAs quantum wells near Landau level filling $\nu = 1$. *Phys. Rev. Lett.*, 76(24):4584–4587, 1996.

[31] Edwin. Hall. On a new action of the magnet on electric currents. *American journal of mathematics*, 2:287–292, 1879.

[32] V.T. Dolgopolov, N.B. Zhitenev, and A. Shashkin. New method for determining Hall conductivity in QHE regime. *EPL*, 14:255–259, 1991.

[33] M. E. Cage. *IEEE Trans Instrum. Meas.*, IM-34:301, 1985.

[34] K.S. Novoselov, Z. Jiang, Y. Zhang, S.V. Morozov, H.L. Stormer, U. Zeitler, J.C. Maan, G.S. Boebinger, P. Kim, and A.K. Geim. Room-temperature quantum Hall effect in graphene. *Science*, 315(5817):1379, 2007.

[35] S. Luryi and R.F. Kazarinov. Theory of quantized Hall effect at low temperatures. *Physical Review B*, 27(2):1386–1389, 1983.

[36] B.I. Halperin. Quantized Hall conductance, current-carrying edge states, and the existence of extended states in a two-dimensional disordered potential. *Physical Review B*, 25(4):2185–2190, 1982.

[37] R. B. Laughlin. Quantized Hall conductivity in two dimensions. *Phys. Rev. B*, 23(10):5632–5633, 1981.

[38] C. W. J. Beenakker. Edge channels for the fractional quantum Hall effect. *Phys. Rev. Lett.*, 64(2):216–219, 1990.

[39] D. B. Chklovskii, B. I. Shklovskii, and L. I. Glazman. Electrostatics of edge channels. *Phys. Rev. B*, 46(7):4026–4034, 1992.

[40] C. W. J. Beenakker and H. van Houten. Quantum transport in semiconductor nanostructures. *Solid State Physics*, 44:1, 1991.

[41] Ruthenium oxide thermometer: model no. RO600A1, serial no. 1988, calibrated for the range 0.05K to 4.2K by Scientific Instruments.

[42] Stycast(1266): manufactured by GRACE speciality polymers, WR GRACE and Co, Belgium. Purchased from distributors HITEK Electronics Materials Ltd. 15, Wentworth Road, South Park Industrial Estate, Scunthorpe, North Lincolnshire, DN17 2AX.

[43] GE Varnish: ICEles03, distributed by ICEoxford Limited, Oxford, OX2 0ES, UK.

[44] Gold (Au) wire (LS255439 J V AU00512/13) bought from Goodfellow Cambridge Ltd, PE29 6WR, UK. Diameter 0.025mm, Temper: Hard, purity 99.99+.

[45] Silver paint: (Silver in Methyl Isobutyl Ketone) Manufacturer brand: Acheson Electrodag 1415M. Distributed by Agar Scientific (product number G3648), batch no. 0334. Agar Scientific, Essex, CM24 8DA, UK.

[46] M Smith. Torque magnetometry studies of two-dimensional electron systems. Master's thesis, School of Physics, University of Exeter, 2005.

[47] E. M. Forgan and S. Nedjat. Heat capacity cryostat and novel methods of analysis for small specimens in the 1.5–10 K range. *Review of Scientific Instruments*, 51(4):411–417, 1980.

[48] P. F. Sullivan and G. Seidel. Steady-state, AC-temperature calorimetry. *Phys. Rev.*, 173(3):679–685, 1968.

[49] T.H.K. Barron and G.K. White. *Heat capacity and thermal expansion at low temperatures*. Plenum Pub Corp, 1999.

[50] G. R. Stewart. Measurement of low-temperature specific heat. *Review of Scientific Instruments*, 54(1):1–11, 1983.

[51] T.J. Kershaw, A. Usher, A.S. Sachrajda, J. Gupta, Z.R. Wasilewski, M. Elliott, D.A. Ritchie, and M.Y. Simmons. Decay of long-lived quantum Hall induced currents in 2D electron systems. *New Journal of Physics*, 9(3):71, 2007.

[52] D. C. Tsui and A. C. Gossard. Resistance standard using quantization of the Hall resistance of GaAs-AlGaAs heterostructures. *Applied Physics Letters*, 38 (7):550–552, 1981.

[53] D. C. Tsui, H. L. Störmer, and A. C. Gossard. Zero-resistance state of two-dimensional electrons in a quantizing magnetic field. *Phys. Rev. B*, 25(2): 1405–1407, 1982.

[54] G. Ebert, K. von Klitzing, K. Ploog, and G. Weinmann. Two-dimensional magneto-quantum transport on GaAs-AlGaAs heterostructures under non-ohmic conditions. *Journal of Physics C: Solid State Physics*, 16(28):5441–5448, 1983.

[55] M. E. Cage, R. F. Dziuba, B. F. Field, E. R. Williams, S. M. Girvin, A. C. Gossard, D. C. Tsui, and R. J. Wagner. Dissipation and dynamic nonlinear behavior in the quantum Hall regime. *Phys. Rev. Lett.*, 51(15):1374–1377, 1983.

[56] S. Komiyama, T. Takamasu, S. Hiyamizu, and S. Sasa. Breakdown of the quantum Hall effect due to electron heating. *Solid State Commun*, 54:479–84, 1985.

[57] P. Streda and K. von Klitzing. Critical non-dissipative current of quantum Hall regime. *Journal of Physics C: Solid State Physics*, 17(19):L483–L486, 1984.

[58] O. Heinonen, P. L. Taylor, and S. M. Girvin. Electron-phonon interactions and the breakdown of the dissipationless quantum Hall effect. *Phys. Rev. B*, 30(6):3016–3019, 1984.

[59] L. Eaves and F.W. Sheard. Size-dependent quantised breakdown of the dissipationless quantum Hall effect in narrow channels. *Semiconductor science and technology*, 1:346–349, 1986.

[60] L. Bliek, E. Braun, G. Hein, V. Kose, J. Niemeyer, G. Weimann, and W. Schlapp. Critical current density for the dissipationless quantum Hall effect. *Semiconductor Science and Technology*, 1:110–112, 1986.

[61] J. Gething. *Eddy Current Induced Breakdown of the Quantum Hall Effects*. PhD thesis, University of Exeter, 2005.

[62] S. Takaoka, K. Oto, H. Kurimoto, K. Murase, K. Gamo, and S. Nishi. Magnetocapacitance and the edge state of a two-dimensional electron system in the quantum Hall regime. *Phys. Rev. Lett.*, 72(19):3080–3083, 1994.

[63] C.L. Petersen and Hansen. O.P. The diagonal and off-diagonal AC conductivity of two-dimensional electron gases with contactless Corbino geometry in the quantum Hall regime. *Journal of Applied Physics*, 80(8):4479–4483, 1996.

[64] P. M. Morris. *Torque magnetometry Studies of the Integer Quantum Hall Effect*. PhD thesis, Department of Physics and Astronomy, University of Wales, Cardiff, 1998.

[65] K. Oto, S. Takaoka, H. Kurimoto, and K. Murase. Magnetocapacitance and the edge state of a two-dimensional electron system in the quantum Hall regime. *Proceedings of Semi Mag 94*, (1994).

[66] L. B. Rigal, D. K. Maude, M. Potemski, J. C. Portal, L. Eaves, Z. R. Wasilewski, G. Hill, and M. A. Pate. Phase diagram for the breakdown of the quantum Hall effect. *Phys. Rev. Lett.*, 82(6):1249–1252, 1999.

[67] A. J. Matthews, K. V. Kavokin, A. Usher, M. E. Portnoi, M. Zhu, J. D. Gething, M. Elliott, W. G. Herrenden-Harker, K. Phillips, D. A. Ritchie, M. Y. Simmons, C. B. Sorensen, O. P. Hansen, O. A. Mironov, M. Myronov, D. R. Leadley, and M. Henini. Temperature dependence of the breakdown of the quantum Hall effect studied by induced currents. *Phys. Rev. B*, 70(7):075317, 2004.

[68] C.L. Jones, A. Usher, M. Elliott, W.G. Herrenden-Harker, A. Potts, R. Shepherd, T.S. Cheng, and C.T. Foxon. Contactless detection of current breakdown of the quantum Hall effect. *Solid State Communications*, 97(9):763–768, 1996.

[69] A. Usher and M. Elliott. Magnetometry of low-dimensional electron and hole systems. *Journal of Physics, Condensed Matter*, 21(10), 2009.

[70] K.V. Kavokin, M.E. Portnoi, A.J. Matthews, A. Usher, J. Gething, D.A. Ritchie, and M.Y. Simmons. Induced currents, frozen charges and the quantum Hall effect breakdown. *Solid State Communications*, 134(4):257–259, 2005.

[71] M. I. Dyakonov. Possible mechanism for the breakdown of the quantum Hall effect. *Solid State Communications*, 78(9):817 – 821, 1991.

[72] A. H. MacDonald, T. M. Rice, and W. F. Brinkman. Hall voltage and current distributions in an ideal two-dimensional system. *Phys. Rev. B*, 28(6):3648–3650, 1983.

[73] N.Q. Balaban, U. Meirav, H. Shtrikman, and Y. Levinson. Scaling of the critical current in the quantum Hall effect: A probe of current distribution. *Physical review letters*, 71(9):1443–1446, 1993.

[74] C. L. Jones, A. Usher, M. Elliott, W. G. Herrenden-Harker, A. Potts, R. Shepherd, T. S. Cheng, and C. T. Foxon. The decay of induced eddy currents in

a two-dimensional electron system. *Solid State Communications*, 95(7):409 – 413, 1995.

[75] T. Haavasoja, H.L. Störmer, D.J. Bishop, V. Narayanamurti, A.C. Gossard, and W. Wiegmann. Magnetization measurements on a two-dimensional electron system. *Surface Science*, 142(1-3):294 – 297, 1984.

[76] M. Elliott, Y. Lu, K. L. Phillips, W. G. Herrenden-Harker, A. Usher, A. J. Matthews, J. D. Gething, M. Zhu, M. Henini, and D. A. Ritchie. Novel breakdown of the quantum Hall effect: An example of self-organised criticality? *EPL*, 75(2):287–293, 2006.

[77] F.W. Grover. *Inductance calculations, working formulas and tables*. Van Nostrand Reinhold, 1946.

[78] W.T. Scott and H.C. Wolfe. *The physics of electricity and magnetism*, volume 28. 1960.

[79] BJ Van Wees, LP Kouwenhoven, H. van Houten, CWJ Beenakker, JE Mooij, CT Foxon, and JJ Harris. Quantized conductance of magnetoelectric subbands in ballistic point contacts. *Physical Review B*, 38(5):3625–3627, 1988.

[80] DA Wharam, TJ Thornton, R. Newbury, M. Pepper, H. Ahmed, JEF Frost, DG Hasko, DC Peacock, DA Ritchie, and GAC Jones. One-dimensional transport and the quantisation of the ballistic resistance. *J. Phys. C*, 21(L209-214): 26, 1988.

[81] M. Pioro-Ladrière, A. Usher, AS Sachrajda, J. Lapointe, J. Gupta, Z. Wasilewski, S. Studenikin, and M. Elliott. Influence of the long-lived quantum Hall potential on the characteristics of quantum devices. *Physical Review B*, 73(7):75309, 2006.

[82] brand name Rizla, type RIZLA+ (green packaging).

[83] Copper (Cu) Insulated wire (LS213617 B G CU005825/2) bought from Goodfellow Cambridge Ltd, PE29 6WR, UK. Diameter 0.025mm, insulation (Polyurethane) thickness 0.005mm, purity 99.99.

[84] Super Glue: branded 'Loctite' liquid.Manufactured by Henkel Loctite (Irl) Limited, distributed by Henkel Consumer Adhesives, Cheshire, UK, CW7 3QY.

[85] M. Pioro-Ladriere, J.H. Davies, AR Long, AS Sachrajda, L. Gaudreau, P. Zawadzki, J. Lapointe, J. Gupta, Z. Wasilewski, and S. Studenikin. Origin of switching noise in GaAs/AlGaAs lateral gated devices. *Physical Review B*, 72 (11):115331, 2005.

[86] R. J. Haug, J. Kucera, P. Streda, and K. von Klitzing. Scattering experiments in two-dimensional systems in the presence of quantizing magnetic fields. *Phys. Rev. B*, 39(15):10892–10900, 1989.

[87] H. van Houten, C. W. J. Beenakker, P. H. M. van Loosdrecht, T. J. Thornton, H. Ahmed, M. Pepper, C. T. Foxon, and J. J. Harris. Four-terminal magnetoresistance of a two-dimensional electron-gas constriction in the ballistic regime. *Phys. Rev. B*, 37(14):8534–8536, 1988.

[88] J. G. E. Harris, D. D. Awschalom, K. D. Maranowski, and A. C. Gossard. Magnetization and dissipation measurements in the quantum Hall regime using an integrated micromechanical magnetometer. 87(9):5102–5104, 2000.

[89] N. Ruhe, J. I. Springborn, Ch. Heyn, M. A. Wilde, and D. Grundler. Simultaneous measurement of the de Haas-van Alphen and the Shubnikov-de Haas effect in a two-dimensional electron system. *Physical Review B*, 74(23):235326, 2006.

[90] JI Springborn, N. Ruhe, C. Heyn, MA Wilde, D. Heitmann, and D. Grundler. Gate-controlled de Haas van-Alphen effect in an interacting two-dimensional electron system. *Physica E*, 34(1-2), 2006.

[91] AH bridge: AH 2500A 1 kHz Ultra-Precision Capacitance Bridge. Andeen-Hagererling, Inc.Cleveland, Ohio, USA.

[92] W.C. Fon, K.C. Schwab, J.M. Worlock, and M.L. Roukes. Nanoscale, phonon-coupled calorimetry with sub-attojoule/Kelvin resolution. *Nano Letters*, 5(10): 1968–1971, 2005.

[93] B. W. Dodson, W. L. McMillan, J. M. Mochel, and R. C. Dynes. Metal-insulator transition in disordered germanium-gold alloys. *Phys. Rev. Lett.*, 46 (1):46–49, 1981.

[94] N.A. Fortune, M. J. Graf, and K. Murata. Physical dependence of the sensitivity and room-temperature stability of AuGe thin film resistive thermometers on annealing conditions. *Review of Scientific Instruments*, 69(1):133–138, 1998.

[95] Z. Tan, SM Heald, M. Rapposch, CE Bouldin, and JC Woicik. Gold-induced germanium crystallization. *Physical Review B*, 46(15):9505–9510, 1992.

[96] A. Barna, PB Barna, and JF Pocza. Crystallization processes in AuGe thin films. *J Non-Cryst. Solids*, 8:36, 1972.

[97] S. Zhang, X. Wang, Z. Chen, Z. Wu, NY Jin-Phillipp, M. Kelsch, and F. Phillipp. In situ TEM study of fractal formation in amorphous Ge/Au bilayer films. *Physical Review B*, 60(8):5904–5908, 1999.

[98] Cotton buds: Johnson's Cotton buds, manufactured by Johnson & Johnson.

[99] PMMA photoresist: Microchem 950K A7 PMMA. The average weight of the PMMA is 950,000, and the solvent is anisole. The mixture is a 7% solution of PMMA in anisole. The PMMA was further diluted with anisole in the ratio of PMMA:anisole 2:1. This gives a film thickness of around 350nm when span at 4,000rpm for 30 seconds.

[100] PLSI: PLSI is mixed as 1:1 mixture with de-ionised water.